THE UNIVERSITY OF QUEENSLAND

AUSTRALIA

Development of new layer-structured materials as photocatalysts for water splitting

Zheng Xing

Bachelor's degree in Materials Engineering and Science

A thesis submitted for the degree of Doctor of Philosophy at

The University of Queensland in 2014

School of Chemical Engineering

Abstract

To solve many environment and energy related issues, photosynthesis has been widely investigated for the past several decades as it promises to be a potential reliable method to convert the nearly unlimited solar energy to chemical energy. In particular, photocatalytic water splitting has drawn great interest, which can decompose water molecules to hydrogen and oxygen in the presence of semiconductor photocatalysts under light irradiation. Among many semiconductors investigated for photocatalysis, layered semiconductors form a unique group of photocatalysts due to their special properties such as improved charge separation and easily tuned composition. Moreover, some layered semiconductors can be exfoliated to ultrathin nanosheets (NSs), which not only exhibit distinct properties compared to the bulk materials, but also can be used to fabricate novel nanostructures. This dissertation is devoted to develop nanocomposites based on layered semiconductors for efficient photocatalytic water splitting. A series of heterogeneous photocatalysts were constructed from layered semiconductors such as graphitic carbon nitride (g-C_3N_4) and exfoliated semiconductors including titanium oxide ($Ti_{0.91}O_2$) NSs and g-C_3N_4 NSs.

By coupling $Ti_{0.91}O_2$ NSs and octahedral gold nanoparticles (NPs), a nanohybrid was formed, in which Au NPs were embedded into the matrix of titanium oxide. The surface plasmon resonance (SPR) effect of Au NPs introduced a broad absorption peak in the visible region to the nanohybrid. The nanohybrid showed considerably improved photocatalytic hydrogen production performance compared to naked titanium oxide and conventional titanium oxide with photo-deposited Au due to the local light intensity enhancement and photon scattering effect.

A nanocomposite photocatalyst composed of $Ti_{0.91}O_2$ NSs and CdTe@CdS nanocrystals (NCs) was successfully synthesized via a facile restacking approach. In the nanocomposite, the $Ti_{0.91}O_2$ NSs randomly stacked upon each other while the CdTe@CdS NCs were sandwiched between $Ti_{0.91}O_2$ NSs. The introduction of CdTe@CdS NCs not only extended the visible light absorption, but also formed p-n nanojunctions in the nanocomposite. The photocatalytic hydrogen evolution under visible light irradiation was significantly enhanced compared to pure CdTe@CdS NCs due to the effective charge separation, which was achieved by the synergetic effect of proper energy band alignment and p-n nanojunctions.

A new type of polymeric composite photocatalyst was prepared by co-loading g-C_3N_4 with poly(3,4-ethylenedioxythiophene) (PEDOT) as hole transport pathway and Pt as electron trap. As a result of the spatial separation of reduction and oxidation reaction sites on g-C_3N_4 surface, the photocatalytic water splitting activity of the composite was dramatically increased compared to those of C_3N_4-PEDOT and C_3N_4-Pt.

Phosphorus-doped g-C_3N_4 NSs were synthesized by doping bulk g-C_3N_4 and subsequent exfoliation in water. The obtained 1 nm-thick P-doped g-C_3N_4 NSs were highly stable in water suspension and carried negative surface charge, while pure g-C_3N_4 did not undergo effective exfoliation. The NSs suspension was able to produce hydrogen under visible light irradiation, in contrast to the visible-light-inactive undoped counterpart. More importantly, the P-doped g-C_3N_4 NSs were demonstrated to be used to construct layer-by-layer (LBL) assembly onto different substrates. The photoelectrode with LBL assembly on FTO glass substrate showed visible light response.

Declaration by author

This thesis is composed of my original work, and contains no material previously published or written by another person except where due reference has been made in the text. I have clearly stated the contribution by others to jointly-authored works that I have included in my thesis.

I have clearly stated the contribution of others to my thesis as a whole, including statistical assistance, survey design, data analysis, significant technical procedures, professional editorial advice, and any other original research work used or reported in my thesis. The content of my thesis is the result of work I have carried out since the commencement of my research higher degree candidature and does not include a substantial part of work that has been submitted to qualify for the award of any other degree or diploma in any university or other tertiary institution. I have clearly stated which parts of my thesis, if any, have been submitted to qualify for another award.

I acknowledge that an electronic copy of my thesis must be lodged with the University Library and, subject to the General Award Rules of The University of Queensland, immediately made available for research and study in accordance with the *Copyright Act 1968*.

I acknowledge that copyright of all material contained in my thesis resides with the copyright holder(s) of that material. Where appropriate I have obtained copyright permission from the copyright holder to reproduce material in this thesis.

Publications during candidature

Peer-reviewed papers

1. **Xing, Z**.; Zong, X.; Pan, J.; Wang, L., On the engineering part of solar hydrogen production from water splitting: Photoreactor design. ***Chem. Eng. Sci.*** 2013**,** *104*, 125-146, review article.
2. **Xing. Z**,; Chen, Z.; Zong, X.; Wang L., A new type of carbon nitride-based polymer composite for enhanced photocatalytic hydrogen production. ***Chem. Commun.***, 2014, 50, 6762-6764.
3. Bai, Y.; **Xing, Z**.; Yu, H.; Li, Z.; Amal, R.; Wang, L., Porous titania nanosheet/nanoparticle hybrids as photoanodes for dye-sensitized solar cells. ***ACS Appl. Mater. Interfaces*** 2013, 5 (22), 12058-12065.
4. Seger, B.; McCray, J.; Mukherji, A.; Zong, X.; **Xing, Z**.; Wang, L., An n-Type to p-Type Switchable Photoelectrode Assembled from Alternating Exfoliated Titania Nanosheets and Polyaniline Layers. ***Angew. Chem., Int. Ed.*** 2013, 52 (25), 6400-6403.
5. Zong, X.; **Xing, Z**.; Yu, H.; Bai, Y.; Lu, G. Q.; Wang, L. Z., Photocatalytic hydrogen production in a noble-metal-free system catalyzed by in situ grown molybdenum sulfide catalyst. ***J. Catal.*** 2014, 310, 51-56.
6. Zong, X.; Thaweesak, S.; Xu, H.; **Xing, Z**.; Zou, J.; Lu, G. M.; Wang, L., A scalable colloidal approach to prepare hematite films for efficient solar water splitting. ***Phys. Chem. Chem. Phys.*** 2013, 15 (29), 12314-12321.
7. Zong, X.; Sun, C.; Yu, H.; Chen, Z. G.; **Xing, Z**.; Ye, D.; Lu, G. Q.; Li, X.; Wang, L., Activation of photocatalytic water oxidation on N-doped ZnO bundle-like nanoparticles under visible light. ***J. Phys. Chem. C*** 2013, 117 (10), 4937-4942.
8. **Xing, Z**.; Zong, X.; Butburee, T.; Pan, J.; Bai, Y.; Wang, L., Nanohybrid materials of titania nanosheets and plasmonic gold nanoparticles for effective hydrogen evolution (Submitted)
9. **Xing, Z**.; Bai, Y.; Zong, X.; Zhu, Y.; Chen, Z. G.; Wang, L., A nanohybrid of CdTe@CdS nanocrystals and titania nanosheets with p-n nanojunctions for visible light hydrogen production. (Submitted)
10. **Xing, Z**.; Zong, X.; Chua, Y. T.; Wang, L., A nanocomposite of two different semiconductor nanosheets for enhanced photocatalytic hydrogen evolution. (In preparation)
11. **Xing, Z**.; Zong, X.; Wang, B.; Wang, L., Metal-free semiconducting nanosheets as building blocks for nanodevices. (Submitted)

Publications included in this thesis

Nanohybrid materials of titania nanosheets and plasmonic gold nanoparticles for effective hydrogen evolution

Zheng Xing, *Xu Zong, Teera Butburee, Jian Pan, Yang Bai, and Lianzhou Wang*

Submitted to **Chemcatchem**

Incorporate as **Chapter 3**

Contributor	Statement of contribution
Zheng Xing	Designed experiments (100%) Wrote the paper (100%)
Xu Zong	Edited paper (50%)
Teera Butburee	Synthesize gold nanoparticles
Jian Pan	Guidance for some experiments
Yang Bai	TEM characterisations
Lianzhou Wang	Edited paper (50%)

A nanohybrid of CdTe@CdS nanocrystals and titania nanosheets with p-n nanojunctions for visible light hydrogen production

Zheng Xing, *Yang Bai, Xu Zong, Yian Zhu, Zhigang Chen, and Lianzhou Wang*

Submitted to **Nanoscale**

Incorporate as **Chapter 4**

Contributor	Statement of contribution
Zheng Xing	Designed experiments (100%) Wrote the paper (100%)

Yang Bai	Help with synthesis of CdTe@CdS NCs
Xu Zong	Edited paper (50%)
Yian Zhu	Help with synthesis of CdTe@CdS NCs
Zhigang Chen	HRTEM characterisations
Lianzhou Wang	Edited paper (50%)

A new type of carbon nitride-based polymer composite for enhanced photocatalytic hydrogen production

Zheng Xing, *Zhigang Chen, Xu Zong, and Lianzhou Wang*

Chemical Communications, 2014, 50, 6762-6764

Incorporate as **Chapter 5**

Contributor	Statement of contribution
Zheng Xing	Designed experiments (100%) Wrote the paper (100%)
Zhigang Chen	TEM characterisations
Xu Zong	Edited paper (50%)
Lianzhou Wang	Edited paper (50%)

Metal-free semiconducting nanosheets as building blocks for nanodevices

Zheng Xing, *Xu Zong, Bei Wang, and Lianzhou Wang*

Submitted to **Adv. Mater.**

Incorporate as **Chapter 6**

Contributor	Statement of contribution
Zheng Xing	Designed experiments (100%) Wrote the paper (100%)
Xu Zong	Edited paper (50%)
Bei Wang	AFM characterisations
Lianzhou Wang	Edited paper (50%)

Contributions by others to the thesis

Ms. Yen Thien Chua helped with TEM characterisations in the work described in chapter 4 and chapter 6.

Statement of parts of the thesis submitted to qualify for the award of another degree

None.

Acknowledgements

First of all, I would like to take this opportunity to express my most sincere gratitude to my research supervisors, Prof. Lianzhou Wang and A/Prof. Xu Zong for their guidance, encouragement and support throughout the course of my PhD research. Prof. Lianzhou Wang, you have taught me not only enormous knowledge, but also how to become a proper researcher with broader vision in the long run. I have benefited so much from the many discussions with you. A/Prof. Xu Zong, I really appreciated it that you spent so much time teaching me even the very little things in the lab, patiently revising my manuscripts time after time and kindly sharing your exciting ideas with me. You have also acted as role model of mine and showed me the importance of hard work.

I am extremely thankful to Mr. Yang Bai, Mr. Teera Butburee, Mr. Delai Ye, Mr. Jian Pan, Dr. Hongjun Chen, Dr. Zhigang Chen and Dr. Bei Wang for their help with materials characterisations including TEM, HRTEM, AFM, etc. and valuable suggestions from them. I would like to thank Ms. Yen Thien Chua for helping me with many materials characterisations techniques including TEM, HRTEM, XRD, etc. I also would like to thank Mrs Cheryl Berquist and Mrs Celestien Warnaar for their lab and administration management.

I acknowledge the scholarships I received from the UQ graduate school for awarding me the University of Queensland Research Scholarship (UQRS). I am also thankful to the Nanomaterials Centre, the Australian Institute of Bioengineering and Nanotechnology (AIBN) and School of Chemical Engineering.

Words can’t express my deepest gratitude to my parents Mr. Yunshan Xing and Mrs. Chuanying Liu, from whom I received endless support, encouragement, love and guidance. Without them, I will never be the man I am today. I would like to thank my girlfriend Ms. Yue Zhao who was, is and will always be the love of my life. I would express my thanks to my dearest friends, Mr. Huan Qian and Mr. Shulong Ye, who have always got my back.

Keywords

photocatalysis, water splitting, layered semiconductors, nanosheets, nanocomposites

Australian and New Zealand Standard Research Classifications (ANZSRC)

ANZSRC code: 090499, Chemical Engineering not elsewhere classified, 60%

ANZSRC code: 091202, Composite and Hybrid Materials, 40%

Fields of Research (FoR) Classification

FoR code: 0904, Chemical Engineering, 100%

Table of contents

List of Figures

List of Tables

List of Abbreviations

AFM	Atomic force micrograph
$BmimPF_6$	1-butyl-3-methylimidazolium hexafluorophosphate
CB	Conduction band
CBM	Conduction band minimum
CO_2	Carbon dioxide
CTAB	Cetyltrimethylammonium bromide
EG	Ethylene glycol
FDTD	Finite-difference time-domain
FTO	Fluorine doped tin oxide
GC	Gas Chromatography
$g\text{-}C_3N_4$	Graphitic carbon nitride
H_2A	Ascorbic acid
HOMO-LUMO molecular orbital	Highest occupied molecular orbital-lowest unoccupied
IPA	Isopropanol
LB	Langmuir-Blodgett
LBL	Layer-by-layer
LDH	Layered double hydroxide
MB	Methylene blue
Me_4NOH	Tetramethlammonium hydroxide
MO	Methyl orange
MSA	Mercaptosuccinic acid
NC	Nanocrystal
NHE	Normal hydrogen electrode
NMP	N-methyl-pyrrolidone
NP	Nanoparticle
NS	Nanosheet

PAA	Polyallylamine
PANI	Polyaniline
PDDA	Poly(diallyldimethylammonium chloride)
PEC	Photoelectrochemical
PEDOT	Poly (3, 4-ethylenedioxythiophene)
PEI	Polyethyleneimine
PL	Photoluminescence
PMMA	Poly-methylmethacrylate
PPy	Polypyrrole
P3HT	Poly(3-hexylthiophene)
QDSSCs	Quantum dot sensitized solar cells
rGO	Reduced graphene oxide
SP	Surface plasmon
SPR	Surface plasmon resonance
TBAOH	Tetrabutylammonium hydroxide
TEM	Transmission electron microscopy
$Ti(OR)_4$	Titanium alkoxide
TMD	Metal dichalcogenide
VB	Valence band
VBM	Valence band maximum
XRD	X-ray diffraction
XPS	X-ray photoelectron spectroscopy

1. Introduction

1.1 Background

Energy crisis in the mid-1970s triggered the worldwide research enthusiasm of developing renewable energy sources to replace conventional fossil fuels.[1, 2] Moreover, greenhouse gases like carbon dioxide generated from combustion of fossil fuels bring us up against the serious environmental issues, such as global warming and climate change.

In recently years, alternative energy sources including solar energy, wind energy, geothermal energy, tidal energy etc. are recognised to be the “green energy” and “future energy”. Solar energy is one of the most promising alternative energy sources that can replace fossil fuels and fulfil the rising global energy consumption demand. The Sun can provide enough energy for all human’s annual use in just one hour, supplying power of 1.2×10^{17} watts continuously.[3] Due to the nearly infinite solar energy, the decade 1996-2005 witnessed an average annual 31% increase of solar cell market, as shown in Figure 1.1.[3]

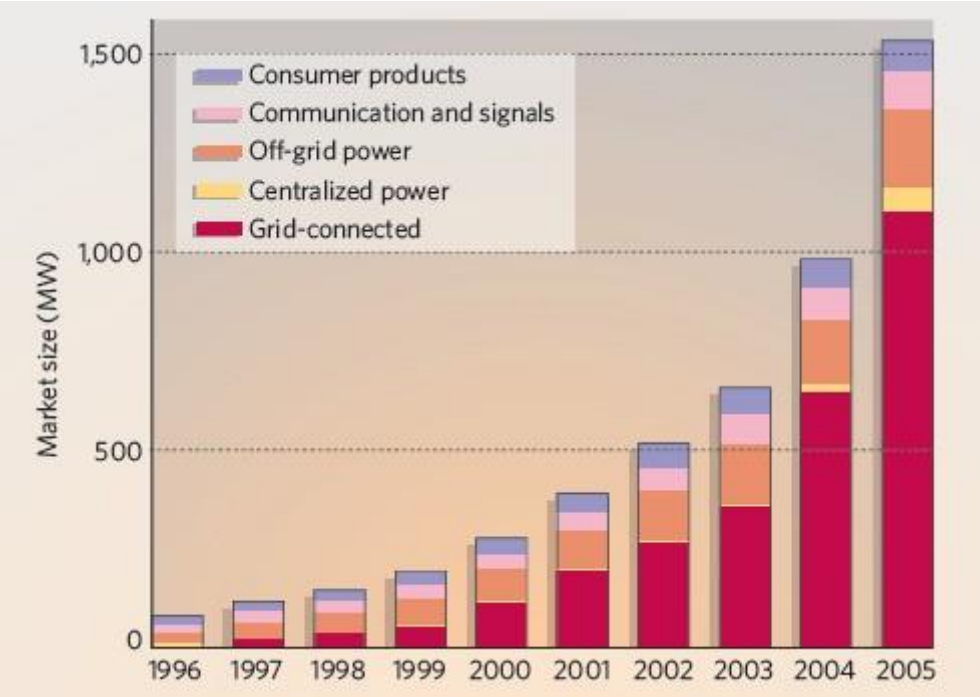

Figure 1.1 Solar cell market between 1996 and 2005.[3]

One of the most effective approaches to harvest the solar energy is the photoinduced production of H_2 and O_2 molecules using semiconductor photocatalysts.[4] Unlike solar cells which transform solar energy to electrical energy, photocatalysis utilizes sunlight to generate hydrogen and oxygen directly. When a photocatalyst is irradiated with light, it captures photons and is excited to generate electrons and holes, which are subsequently used to decompose water molecules to H_2 and O_2.

Hydrogen fuel is a good replacement of gasoline because hydrogen has the highest energy capacity per unit mass among different fuels and generates just water after combustion.[5] Hydrogen can be produced in various ways[6]:

1) Water electrolysis: the most important hydrogen production way because of the high energy conversion efficiency.

2) Thermochemical water splitting and biomass decomposition: solar energy is collected by tower concentrators and other devices and then concentrated to produce very high energy; this high energy is subsequently used to split water or thermochemical biomass decomposition.

3) Photoelectrochemical (PEC) and photocatalytic water splitting: PEC devices utilize photoelectrode made of photocatalyst to split water with the assistance of external

voltage, while photocatalysis process only involves semiconductor materials and light irradiation.

4) Biological hydrogen production: still in early laboratory-scale research stage, using hydrogen-production enzymes.

Among all the hydrogen production methods, photocatalytic water splitting is the most straightforward and promising one, considering the absence of external potential, safety factor, environmental friendliness and nearly unlimited solar energy supply.

1.2 Research aim and scope of the project

This project aims to develop a series of heterogeneous photocatalysts based on layer-structured semiconductors for efficient water splitting. Two semiconductors with layered structure were chosen to be the starting materials, that is, caesium titanate with perovskite structure, and graphitic carbon nitride (g-C_3N_4) with graphite-type structure. There are two aspects from which the materials are manipulated:

(1) Exfoliation of the layered semiconductors to form 2-D ultrathin nanosheets (NSs)

(2) Constructing composites through combination of the layered materials or the exfoliated NSs with guest species

Through the manipulation of photocatalysts from these two aspects, photocatalysts can be delicately controlled and investigated in terms of:

(1) Achieving unique features after exfoliation of layered semiconductors, as the 2-D NSs generally exhibit not only very different optical and chemical properties compared to the bulk counterpart, but also altered surface and energy related natures

(2) Introducing special functionalities by incorporation of guest species with desired chemical or optical properties, such as excellent visible light absorbance, surface plasmon resonance (SPR), etc.

Via the abovementioned methods, a group of heterogeneous layered nanomaterials can be obtained, with potentially interesting structures and properties. Comprehensive characterisations will be carried out in order to understand the structures and physicochemical properties of the heterogeneous nanomaterials, and more importantly, investigate the relationship between their properties and the photocatalytic water splitting performance.

The key objectives of this project are to:

- Investigate the exfoliation process of both caesium titanate and g-C_3N_4 via wet chemistry method
- Constructing composites with layered semiconductors or the exfoliated nanosheets
- Study the structures and physicochemical properties of the composites

- Evaluate the photocatalytic water splitting capabilities of the composites
- Understand the relationship between the structure, physicochemical properties and the water splitting performance

1.3 Thesis structure

The thesis is prepared with a publication-based style, in which a collection of relevant publications is presented as the main body of the thesis. The overall structure of the thesis will be presented as follows:

Chapter 1: Introduction- background, research aim and scope

Chapter 2: Literature review of the advances in heterogeneous photocatalysts based on layered-structure semiconductors

Chapter 3: Research methodology- materials synthesis, characterisations and photocatalytic water splitting evaluation

Chapter 4: Investigation of a nanohybrid of titania nanosheets and plasmonic gold nanoparticles for photocatalytic water splitting

Chapter 5: Investigation of a nanocomposite material of titania nanosheets and CdTe@CdS nanocrystals with p-n nanojunctions, and its capability of water splitting under visible light irradiation

Chapter 6: Investigation of a polymer composite based on carbon nitride for visible light hydrogen production and the spatial separation of charge carriers in the composite material

Chapter 7: Investigation of a new type phosphorus-doped carbon nitride nanosheets, their self-assembly and performance for photocatalytic and photoelectrochemical water splitting

Chapter 8: Overall conclusions and recommendations for future works

1.4 References

1. J. A. Turner, *Science*, 1999, **285**, 687-689.

2. J. Alic, D. Sarewitz, C. Weiss and W. Bonvillian, *Nature*, 2010, **466**, 316-317.

3. O. Morton, *Nature*, 2006, **443**, 19-22.

4. X. Chen, S. Shen, L. Guo and S. S. Mao, *Chem. Rev.*, 2010, **110**, 6503-6570.

5. J. Nowotny, C. C. Sorrell, T. Bak and L. R. Sheppard, *Sol. Energy*, 2005, **78**, 593-602.

6. L. J. Guo, L. Zhao, D. W. Jing, Y. J. Lu, H. H. Yang, B. F. Bai, X. M. Zhang, L. J. Ma and X. M. Wu, *Energy*, 2010, **35**, 4421-4438.

2. Literature review

The purpose of this chapter was to provide a background context for this thesis. It presents the mechanism and evaluation methods of photocatalytic water splitting, construction of heterogeneous photocatalysts, and the advances of layered semiconductors and their exfoliated form- 2D nanosheets. This chapter forms the foundation for the research and development of heterogeneous photocatalysts based on layered semiconductors.

2.1 Introduction-photocatalysis

Figure 2.1 depicts the band structure characteristics of conductors, semiconductors and insulators. The conduction band (CB) and the valence band (VB) are linked together in conductors so electrons can move freely from the VB to the CB, making it possible to conduct electricity; insulators generally have a very large energy gap between the VB and the CB, inhibiting electron transition. Unlike conductors and insulators, semiconductors have a relatively small band gap, so the VB electrons can be excited and “jump” to the CB in the presence of external energy source (solar, thermal etc.).

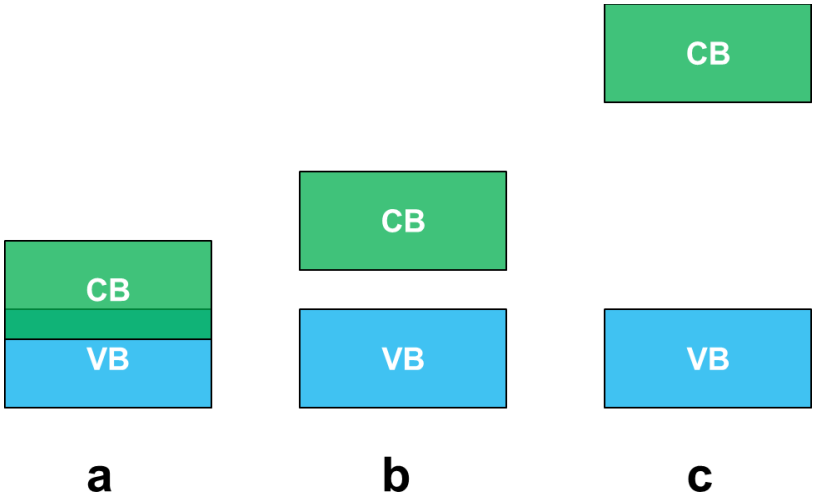

Figure 2.1 Schematic of band structure of (a) conductor, (b) semiconductor and (c) insulator.

This unique energy band structure of semiconductors can be used for photocatalytic applications. In a typical photocatalytic reaction, a semiconductor is photoexcited to generate electrons and holes, and the photoinduced electrons and holes can be captured by surrounding species and participate in reduction and oxidation reactions, respectively. Semiconductor-based photocatalysis has been investigated for a few decades. As shown in Figure 2.2, depending on what charge carriers are consumed, photocatalysis can be generally categorized into two types: photo-oxidative reactions including oxygen evolution, pollutant degradation, etc. and photo-reductive reactions such as hydrogen production, carbon dioxide (CO_2) reduction etc. For example, the CB electrons can be used to reduce protons to hydrogen gases or to reduce CO_2 and H_2O molecules to CO, CH_4, CH_3OH, etc. In the meantime, the VB holes can be used to oxidize H_2O molecules to O_2 gases or to oxidize organic pollutants into oxidized forms and further into CO_2 and other small molecules.

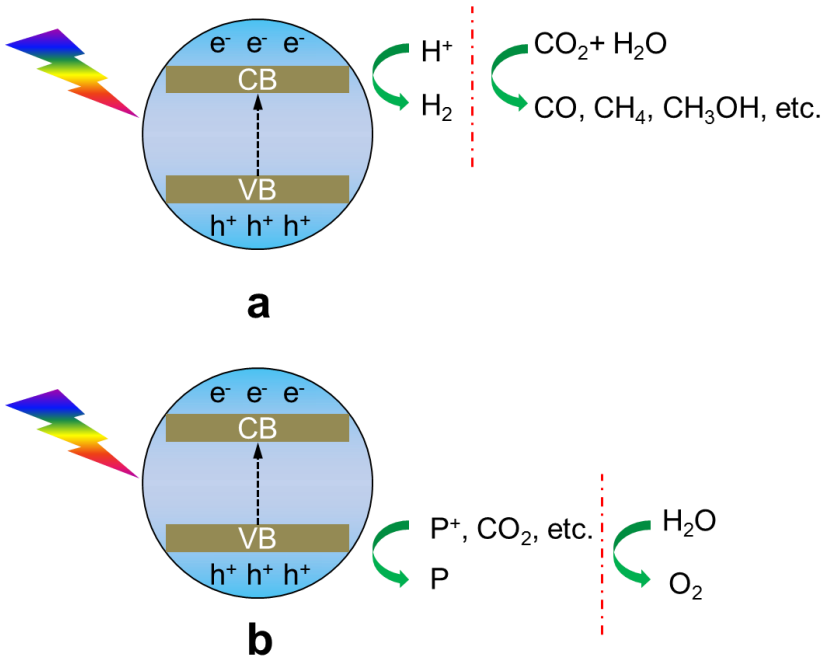

Figure 2.2 Schematics of photocatalytic processes: a) photo-reductive reactions and b) photo-oxidative reactions.

Due to many factors such as semiconductor over potential, surface states, energy band positions, co-catalyst, porosity, pH etc., overall water splitting (simultaneous production of hydrogen and oxygen) is extremely difficult to achieve. In the presence of sacrificial agents and co-catalysts, half of the water splitting, that is, either H_2 evolution or O_2 evolution, is relatively easier to accomplish.

2.2 Water splitting

2.2.1 Principles of photocatalytic water splitting

Water splitting refers to the decomposition of water molecules to hydrogen and oxygen gases, according to Eq. 2.1.

$$H_2O\ (l) \rightarrow H_2\ (g) + \frac{1}{2} O_2\ (g) \qquad \text{(Eq. 2.1)}$$

This reaction has a Gibbs free energy change of ΔG^0=+238 kJ/mol, corresponding to a typical endothermic or "uphill" reaction,[1] which means that this reaction in nature is not spontaneous. The electrical potential corresponding to the Gibbs free energy change calculated according to Eq. 2.2 is 1.23 eV. In terms of wavelength of photons, this corresponds to around 1000 nm (Eq. 2.3).

$$\Delta G^0 = -nFE^0 \qquad \text{(Eq. 2.2)}$$

Where n is the number of electrons transferred in the reaction, F is the Faraday constant

$$E\ (eV) = \frac{1240 eV\ nm}{\lambda(nm)} \qquad \text{(Eq. 2.3)}$$

Semiconductors have a typical band structure as shown in Figure 2.3, in which the CB and the VB are separated by a band gap. In order to excite a semiconductor, photons with higher energy than the band gap are needed to hit the semiconductor, generating electrons and holes in the conduction and valence band, respectively. The electrons in the CB can be used to reduce protons to H_2, while the holes in the VB can be used to oxidize water to O_2. From the angle of thermodynamics, in order to facilitate water splitting, the bottom edge of the CB must be more negative than the proton reduction potential H^+/H_2 (0.0 V vs. normal hydrogen electrode (NHE) at pH=0, -0.47 V at pH=7), and the top edge of the VB must be more positive than the water oxidation potential O_2/H_2O (1.23 V vs. NHE at pH=0, 0.82 V at pH=7).[2] Band positions of some semiconductors are illustrated in Figure 2.4.[3]

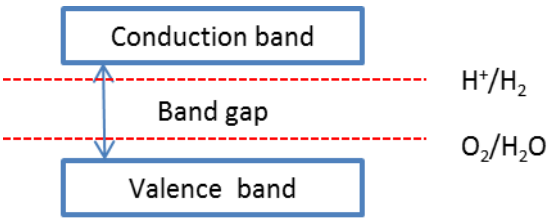

Figure 2.3 Band structures of semiconductor materials.

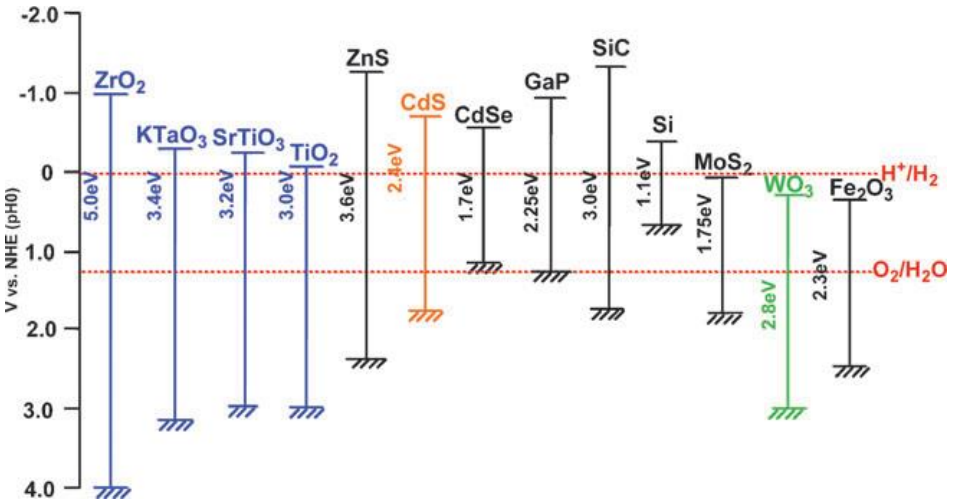

Figure 2.4 Band positions of some semiconductors.[3]

As mentioned before, theoretically, a minimum band gap of 1.23 eV is required for overall water splitting. However, due to over potential, charge separation and other factors, larger band gap is more favourable for this process as it gives the CB electrons stronger reduction power and the VB holes stronger oxidation power.

The overall photocatalytic water splitting process is shown in Figure 2.5. When a photon with high energy excites the semiconductor, an electron in the VB jumps to the CB, leaving a hole in the initial position in the VB. Then the photoexcited electrons and holes diffuse from the bulk to the surface of the semiconductor, where they react with adsorbed water molecules, forming hydrogen and oxygen. However, photoexcited electrons and holes tend to recombine at the same time, not only in the diffusion process, but also at the surface.

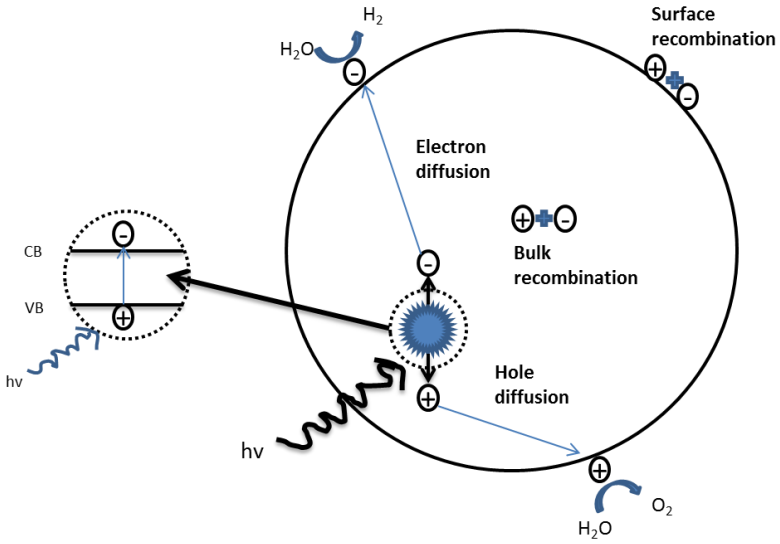

Figure 2.5 Schematic of the overall photocatalytic water splitting process.

By analysing the overall photocatalytic water splitting process, it can be found that a good photocatalyst should meet the following requirements:

1) Excellent light absorption. A good photocatalyst should be able to use a broad range of the solar spectrum. Traditional photocatalysts generally utilize the UV spectrum, which only accounts for 5% of total sunlight energy.[4, 5] So a lot of work has been done to increase visible absorption, including metal or non-metal doping, defects tailoring and so on.

2) Proper energy band position. Semiconductor with high CB has high thermodynamic reducibility, and that with low VB has high thermodynamic oxidizability. Photocatalysts need to possess enough high CB and enough low VB.

3) Efficient charge carriers transfer. The charge diffusion is the key factor affecting electron-hole recombination. If the electrons and holes can transfer to the material surface quickly and reacts with water molecules, then charge recombination will be greatly suppressed.

4) Abundant surface active sites. Even when charge carriers diffuse to the surface, they may also recombine. Therefore, sufficient active sites must be present at the surface of semiconductors, facilitating the water reduction and oxidization. In order to achieve this, some strategies have been developed including addition of co-catalysts, constructing porous structures, surface defect control, facet engineering, surface-doping, etc.

2.2.2 Important components of a water splitting system

Besides the active semiconductor photocatalyst and water, other components may be required in order to achieve efficient water splitting.

Co-catalyst

Photocatalyic activity greatly depends on the presence of co-catalyst in many material systems. Many semiconductors exhibit large over potential, which hinders the redox reactions at the surface. Co-catalysts generally have much smaller over potential in the solution, facilitating the water oxidation or reduction and thus providing active sites. So far some co-catalysts have been verified to be able to strongly promote H_2 evolution including Pt,[4, 6, 7] Au,[8-10] MoS_2,[11, 12] etc. or O_2 evolution including RuO_2,[13, 14] PbO_2,[15] etc.

Sacrificial agent

Many semiconductors are only suitable for half of water splitting, that is, either hydrogen or oxygen evolution. Then the holes in the VB (electrons in the CB) need to be consumed by sacrificial agents like methanol ($AgNO_3$), in order to prevent charge recombination.[16, 17]

Base buffer

Other than sacrificial agents, base buffers such as La_2O_3 are sometimes used to maintain the pH of the solution.[17]

2.2.3 Evaluation of efficiency

The photocatalytic efficiency of photocatalysts can be assessed by direct hydrogen or oxygen gas evolved from water in a certain period of time upon light irradiation. Typically a photocatalyst is dispersed in water, and the reaction proceeds in a quartz reactor connected with an air-free closed gas circulation system.[7, 17, 18] Then the generated gas is collected and analyzed by characterization devices such as Gas Chromatography (GC). The efficiency can be expressed in the unit of $\mu mol \cdot h^{-1}$ and $\mu mol \cdot h^{-1} \cdot g^{-1}$.

Comparison between different photocatalysts is very difficult as reaction conditions such as light source, reaction vessels, co-catalyst and sacrificial agents may vary in different labs. Quantum yield is an important concept in evaluating photocatalytic efficiency. Overall and apparent quantum yield are defined as Eq. 2.4 and Eq. 2.5, respectively. Apparent quantum yield is thought to be smaller than overall quantum yield because incident photons usually outnumber absorbed photons.

$$\text{Overall quantum yield} = \frac{number\ of\ reacted\ electons}{number\ of\ absorbed\ photons} \times 100\% \quad \text{(Eq. 2.4)}$$

$$\text{Apparent quantum yield} = \frac{number\ of\ reacted\ electrons}{number\ of\ incident\ photons} \times 100\% = \frac{2 \times number\ of\ H2\ molecules\ evolved}{number\ of\ incident\ photons} \times$$

$$100\% = \frac{4 \times number\ of\ O2\ molecules\ evolved}{number\ of\ incident\ photons} \times 100\% \quad \text{(Eq. 2.5)}$$

2.3 Heterogeneous photocatalyst

Single-semiconductor photocatalysts often have some intrinsic limitations for water splitting. For instance, many transition metal oxides such as TiO_2, $SrTiO_3$, Nb_2O_5, $K_4Nb_6O_{17}$, Ta_2O_5, $NaTaO_3$, etc. have a wide band gap, making them only active in UV region and not able to capture visible light.[4] In addition, fast charge recombination often restricts the overall photoconversion efficiency. To address some of the intrinsic weaknesses of single semiconductor, a heterostructured photocatalyst is often constructed, in which two or more functional or structural components are combined. Through the synergistic effect of multiple materials, special advantages can be obtained in heterostructured systems.

2.3.1 Mechanism of heterogeneous structure

Through the combination of different materials, unique properties can be introduced and so the working mechanisms may be widely varied in different systems. However, achieving effective charge separation is the ultimate aim of constructing heterostructured materials in many cases. The basic principle in this regard is to make reduction and oxidation reactions take place at different locations. Heterogeneous systems built with this principle can be briefly categorized to 6 groups, as shown in Figure 2.6.[19]

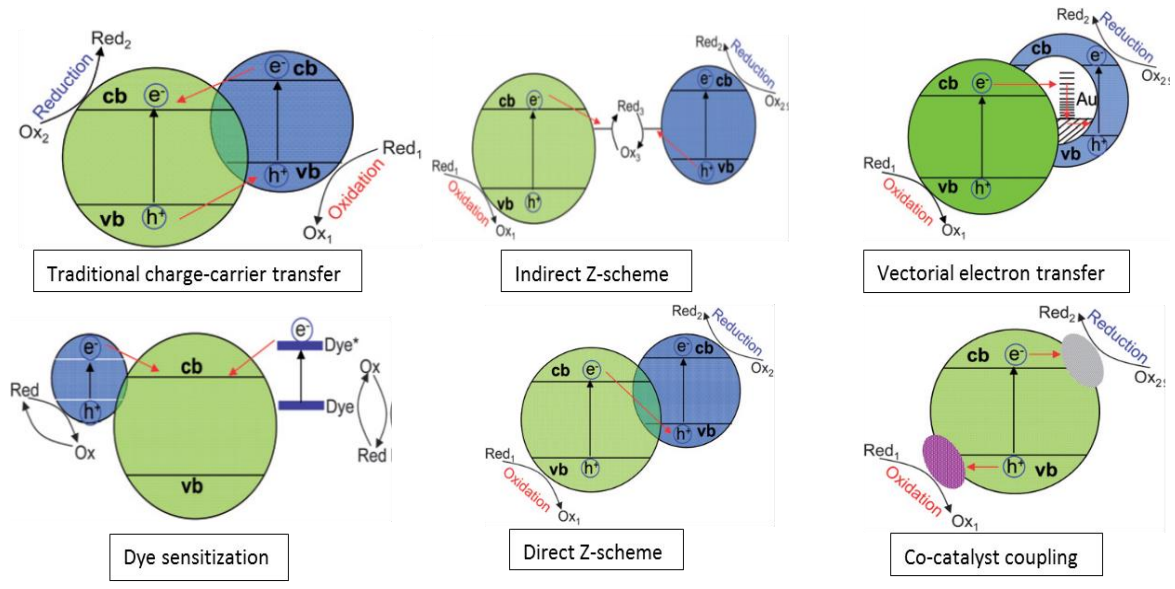

Figure 2.6 Six groups of heterogeneous photocatalyst systems for achieving effective charge separation.[19]

Traditional charge-carrier transfer

In the traditional charge-carrier transfer mechanism, electrons in the CB of a semiconductor with higher conduction band minimum (CBM) will transfer to the CB of a semiconductor with lower CBM, while holes in the VB of a semiconductor with lower valence band maximum (VBM) will transfer to the VB of a semiconductor with higher VBM. The two semiconductors must have suitable band positions and intimate contact, and the transferred electrons and holes will have lower reduction and oxidation power respectively. A typical example of this mechanism is CdS/TiO_2 composites,[20, 21] in which electrons in the CB of CdS can be injected to the CB of TiO_2 upon visible light illumination.

Dye sensitization

Similar to the traditional charge-carrier transfer mechanism, the sensitization mechanism uses a dye sensitizer with higher CBM than the semiconductor, and the electrons in the CB of dye will inject into the CB of the semiconductor. A redox couple electrolyte is required to reproduce the sensitizers.

Indirect Z-scheme

In the indirect Z-scheme mechanism, electrons will transfer from the CB of a semiconductor with lower CBM to the VB of a semiconductor with higher VBM "indirectly" via reaction with a redox couple species (I^-/IO^{3-} etc.) in the solution, so the high redox power of electrons and holes is conserved. This is an effective way to isolate reduction and oxidation reaction sites and also maintain the high redox potential of charge carriers, but the efficiency is still quite low at this stage. For example, Higashi et al. built an indirect Z-scheme system by using Pt-$ATaO_2N$ (A= Ca, Sr, Ba) as the hydrogen evolution photocatalyst, Pt-WO_3 as the oxygen evolution photocatalyst and IO_3^-/I^- as the shuttle redox mediator.[22] Impressively, when Pt-$CaTaO_2N$ or Pt-$BaTaO_2N$ is used as the H_2 evolution photocatalyst, overall water splitting is achieved.

In addition, Maeda et al. [23] reported a Z-scheme heterogeneous structure consisting of modified ZrO_2/TaON as the H_2 evolution catalyst and WO_3 as the O_2 evolution catalyst. When the ZrO_2/TaON and WO_3 were loaded with Pt, and $I^-/IO^{3-}$was used as the redox couple, stoichiometric H_2 and O_2 evolved from water, with high evolution rate of 260 and 133 $\mu mol \cdot h^{-1}$ respectively. A quantum yield of 6.3% can also be obtained in the optimal condition. Kazuhiko Maeda also tested RuO_2/TaON[24] and Ta_3N_5 modified with Ir and rutile titania[25] as the O_2 evolution part in the similar system.

Direct Z-scheme

Similar to the indirect Z-scheme, direct Z-scheme facilitates direct electron transfer between CB and VB by intimate contact between the two semiconductors, but does not require redox couple any more. This is one of the most important mechanisms of heterogeneous structure, and has been investigated by many groups.

For example, Sasaki et al. [26] reported a Z-scheme photocatalytic system in 2009, using Rh-doped $SrTiO_3$ (RuO_x-loaded as co-catalyst) and $BiVO_4$ as H_2 and O_2 evolution catalyst respectively under visible light. The highest activity can be obtained when the weight ratio of $Ru/SrTiO_3$:$Rh/BiVO_4$ was 0.1/0.1. In addition, pH played an important role in the photocatalytic process, and a pH value of 3.5 was found to be most favourable, which gave proper contact between $SrTiO_3$:Rh and $BiVO_4$ particles. 40 $\mu mol \cdot h^{-1}$ for H_2 evolution and 19 $\mu mol \cdot h^{-1}$ for O_2 evolution can be obtained in the best condition. Following Sasaki's work, Iwase et al. [27] exploited reduced graphene oxide (rGO) sheets as the electron mediator because of the good electrical conductivity of graphene.

Vectorial electron transfer

Achieving very intimate contact in the Z-scheme mechanism between two semiconductors is very difficult, so the vectorial electron transfer mechanism has been developed, in which noble metal such as Au is utilized to promote the electron injection. Essentially, the solid-interface metal phase is used to replace the redox mediators in solution. A good example is a CdS-Au-TiO_2 nanojunction developed by Tada et al., in which the vectorial electron transfer was driven by the two-step excitation of TiO_2 and CdS.[28] This three-component system showed a very high photocatalytic activity.

Co-catalyst coupling

The co-catalyst coupling mechanism draws increasing interest recently as more new efficient co-catalysts are being explored, and in this mechanism two different types of co-catalysts are exploited at the same time to catalyse reduction and oxidation reactions separately. For example, Li et al. developed a dual cocatalyst system by loading Pt and PdS on CdS as the reduction and oxidation cocatalysts, respectively, and achieved impressively high quantum efficiency for hydrogen production.[29, 30] Recently, the (010) and (110) facets of the $BiVO_4$ crystals were revealed to be reductive and oxidative, respectively.[15, 31] Based on this finding, the selectively deposited reduction and oxidation catalysts on different facets led to much improved oxygen production upon visible light irradiation compared to $BiVO_4$ with randomly distributed cocatalysts.

Even though the abovementioned six mechanisms have been carefully studied by researchers, in many cases the actual working mechanism of heterostructured materials may not be well-defined by only one certain mechanism and two possible mechanisms can both exist. For instance, Wang et al. [32] built a heterogeneous photocatalyst system composing of ZnO and CdS. Instead of ZnO rods, Wang prepared hexagonal ZnO disks with high facet ratio of the polar facet (top and bottom). The polar facets on the top and bottom were found to be more active than the non-polar facets on the side, and the ZnO/CdS heterostructure in the presence of Na_2S/Na_2SO_3 can produce H_2 at a rate of 88.6 $\mu mol \cdot h^{-1}$, which is 2.8 times that of the ZnO rod one. However the mechanism was not clear, and two mechanisms were proposed. One was the traditional charge-carrier transfer, in which electrons transferred from the CB of CdS to that of ZnO while holes transferred from the VB of ZnO to that of CdS. The other was direct Z-scheme mechanism, in which electrons in the CB of ZnO combined with holes in the VB of CdS.

2.3.2 Different structures of heterogeneous photocatalyst

Depending on the type of materials used in constructing heterogeneous photocatalysts, several structures may be formed, including semiconductor-semiconductor, semiconductor-metal, and semiconductor-graphene. Moreover, a heterogeneous system can also be built with multi-components, forming a more complex and functional heterostructure.

Semiconductor-semiconductor

A semiconductor-semiconductor composite is the most extensively investigated heterogeneous photocatalyst structure. In such a configuration, a better light absorption can be obtained as different semiconductors can utilize different spectrum of the solar light. Moreover, a proper alignment of the band energy positions can facilitate the charge transfer between semiconductors and suppress charge recombination. A good example of this type is TiO_2-semiconductor composites, which attract much interest since TiO_2 was first studied for photoelectrochemical (PEC) water splitting by Fujishima and Honda in 1972.[33] So far many semiconductors have been used to construct composites with TiO_2, such as CdS,[28, 34, 35] Cu_2O,[36-38] CdSe,[39-41] CrO_x,[42] WO_3,[43-45] etc.

Some special features can also be introduced to semiconductor-semiconductor composites, such as p-n junctions. The concept of forming p-n junctions in photocatalysts has been found to be very effective for promoting photocatalytic performance.[46-48] For

example, Meng and his co-workers directly grew p-type MoS_2 nanoplatelets onto n-type nitrogen-doped rGO.[49] The nanoscale p-n junctions in the composites significantly improved the photocatalytic hydrogen production performance. Hou and his co-workers fabricated a composite of n-type $Bi_4Ti_3O_{12}$ nanofibers and p-type BiOI nanosheets (NSs) through a simple process of electrospinning combined with a successive ionic layer adsorption and reaction, which showed enhanced visible-light-driven photocatalytic activity for rhodamine B decomposition.[46]

Semiconductor-metal

Deposition of metal particles onto semiconductors is a general method to introduce surface active sites for photocatalytic reactions. With this principal, a variety of noble metal particles have been used to synthesize semiconductor-metal composites, in which the noble metal particles are termed as co-catalyst. The most popular noble metal is Pt,[4, 6, 7] whereas others have also been investigated including Au,[8-10] Ru,[50-53] Pd,[54-56] Ag,[57-59] Rh,[60, 61] etc.

Despite the good performance of noble metals as co-catalyst, the high cost is an issue. Researchers have been trying to find alternatives, and some progress has been witnessed in recent years. One important noble metal alternative is MoS_2, which was first used by Zong et al. as an efficient co-catalyst to CdS.[11] Following Zong's research, a number of semiconductor-MoS_2 hybrids were studied such as MoS_2-TiO_2,[62, 63] MoS_2-CdSe,[64] MoS_2-C_3N_4,[65] etc. In addition, Zong's finding greatly triggered the interest of finding low-cost noble-metal-free cocatalysts, and many more candidates have been found to perform well. Those include some sulphides such as NiS,[66, 67] PdS,[68] Ag_2S,[69] WS_2,[70] etc. and other compounds such as WC,[71, 72] MnO_x,[73] Ni-Mo-N,[74] etc.

Semiconductor-graphene

Since its discovery in 2004, graphene, the single layer form of graphite, has attracted huge amount of attention in many fields due to its outstanding electrical, mechanical, thermal and optical properties.[75] In particular, as graphene has excellent electron conductivity, significantly expanded surface area and easy functionalization of its surface states, it promises to be an ideal scaffold for semiconductors. When semiconductors are loaded onto graphene sheets, the photogenerated charge carriers are supposed to quickly transfer to graphene, suppressing the charge recombination.[76] Inspired by this idea, many graphene-based photocatalysts have been developed in order to improve the

photocatalysis efficiency, including TiO_2-graphene,[77-79] CdS-graphene,[80, 81] ZnO-graphene,[82, 83] C_3N_4-graphene,[84, 85] $BiVO_4$-graphene,[86, 87] etc.

2.3.3 Building blocks of nanostructured heterogeneous photocatalyst

Traditionally, heterogeneous photocatalysts were fabricated with bulk particles, which have some limitations with regards to the contact between different components. The most advantages of heterostructured photocatalysts depend strongly on the chemical and electric interaction between different components near the interfacial region,[88] so large contact area will be very beneficial, which is not present in the bulk materials. The quick development of nanomaterials paves the way for designing novel heterogeneous nanostructures as nanomaterials not only possess much larger surface area, but also exhibit distinct properties compared to their bulk counterpart such as increased surface active sites and shifted optical absorption.[89, 90] Nanomaterials with a wide range of architectures, morphologies, dimensions provide a large and important group of building blocks for heterogeneous photocatalysts.[89]

Nanoparticles

When the size of a semiconductor particle is reduced, the energetics will be altered. As a result of quantum size confinement effect, the band gap is enlarged, with upshift of CBM and downshift of VBM.[91, 92] The optical absorption properties will also be affected. In addition, the fraction of atoms located at the surface is increased, leading to more available active surface sites and faster interfacial charge-carrier transfer rates.[90] The fascinating properties of nanoparticles drive the numerous research on semiconductor nanoparticles. For example, TiO_2 nanoparticles with various morphologies and dimensions have been synthesized via different methods, including sol-gel method, hydrothermal reaction, solvothermal reaction, sonochemical method, microwave treatment, etc.[19, 93] Via hydrolysis and polycondensation of titanium alkoxide ($Ti(OR)_4$) in an environment containing tetramethlammonium hydroxide (Me_4NOH), Chemseddine et al. successfully synthesize TiO_2 nanocrystals of different size and shapes, as shown in Figure 2.7.[94]

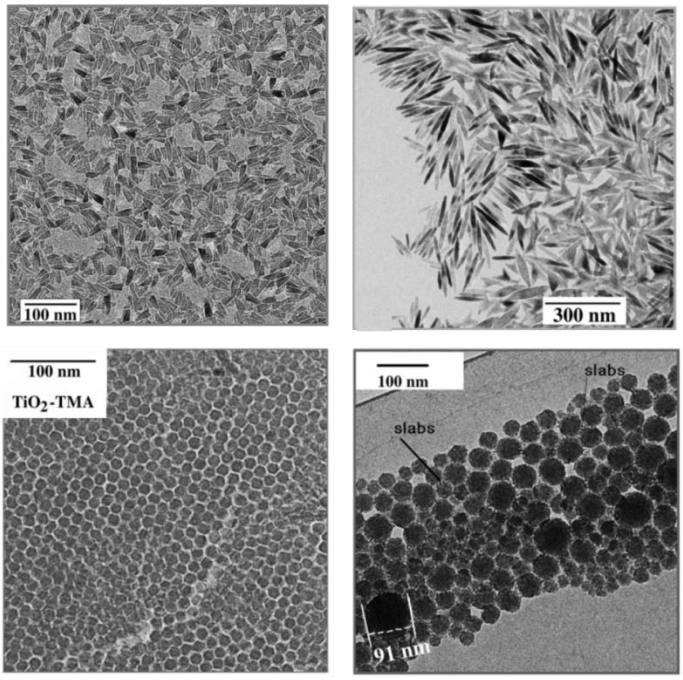

Figure 2.7 TEM images of TiO_2 nanocrystals prepared via hydrolysis of $Ti(OR)_4$ in the presence of Me_4NOH.[94]

It is also found that the facets of TiO_2 nanoparticles play an important role in determining the photocatalytic activities. Based on density functional theory calculations and first principles molecular dynamics simulations, Gong et al.[95] concluded that the minor (001) facets in anatase are more active. Yang et al.[96] first synthesized anatase TiO_2 with 47% (001) facets using HF to control the morphology, as shown in Figure 2.8. Later Han et al.[97] reported an anatase phase with 89% of exposed (001) facets prepared via hydrothermal route. Xie et al.[98] also prepared hollow TiO_2 boxes with >83% (001) facets by calcining $TiOF_2$ precursor with cubic structure.

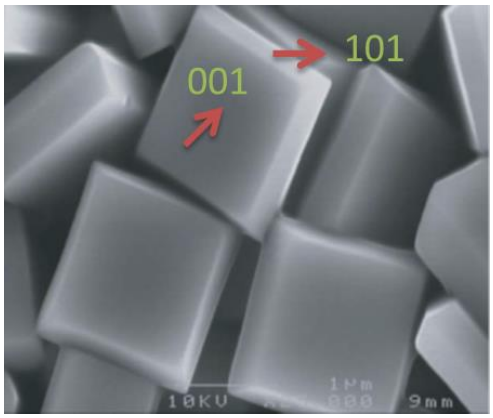

Figure 2.8 TEM image of anatase TiO_2 with 47% (001) facets synthesized by Yang et al.[96]

Besides semiconductor nanoparticles, some noble metal nanoparticles such as Ag, Au, Cu, etc. have drawn great interest recently due to their unique surface plasmon resonance (SPR) properties.[99-101] SPR is defined as the collective oscillation of free electrons when the frequency of incident photons approaches the natural frequency of surface electron oscillation.[102] SPR effect can induce a very strong localized electric field near the noble metal nanostructures, and it can be significantly influenced by the size, shape and embedding medium.[103-107] Of those noble metals, Au draws particular attention as it has strong SPR effect in visible region and many researchers have successfully synthesized Au nanoparticles with varied sizes and diverse morphologies.[107-109] Personick et al. synthesized Au nanoparticles of four different morphologies: octahedral, rhombic dodecahedra, truncated ditetragonal prisms, and concave cubes by tuning the concentration of Ag^+ in the reaction solution in a seed-mediated growth method, as shown in Figure 2.9.[109] With the arising interest in the SPR study of Au, many semiconductor/Au composites have been investigated in terms of visible light activities and it was found that in many cases the enhancement of photocatalytic activities occurred at wavelengths corresponding to the metal SPR.[110-112] The enhancement induced by SPR has been contributed to three proposed mechanisms: direct charge injection from Au nanoparticles to semiconductors, strong SPR-induced near-field electromagnetic energy and effective photon scattering.[103]

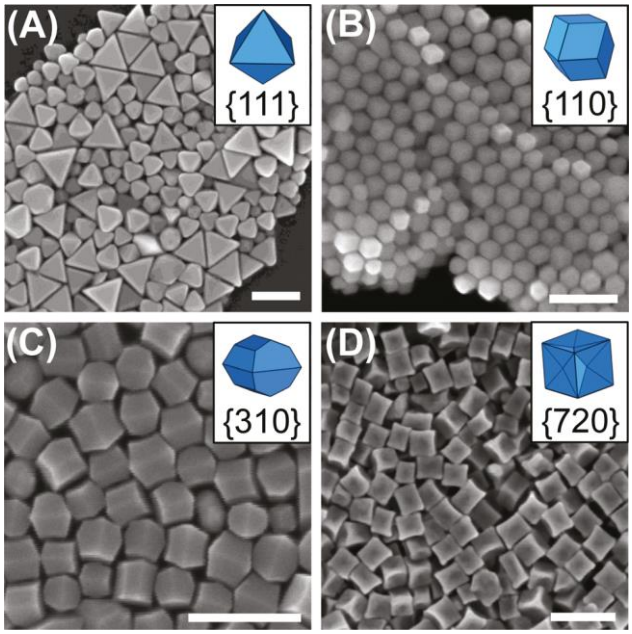

Figure 2.9 SEM images of (A) octahedra, (B) rhombic dodecahedra, (C) truncated ditetragonal prisms, and (D) concave cubes synthesized via a seed-mediated growth method. Scale bar: 200 nm.[109]

1-dimensional nanostructures

One dimensional (1D) nanostructures including nanowires, nanorods, nanotubes and nanobelts have stimulated significant interest as they are very suitable for studying the dependence of properties on the size and dimensionality.[113-115] 1D nanostructures can be synthesize via both template assisted methods (soft-template and hard-template) and template-free methods (molten salt synthesis, hydrothermal, thermolysis, etc.).

The high surface-volume ratio of 1D nanostructures is potentially beneficial for photocatalysis, and so a number of 1D nanostructures has been studied for photocatalytic reactions.[116] For example, 1D nanostructures of some perovskites including $KNbO_3$,[117] $NaTaO_3$,[118] $BiFeO_3$,[119] $SrTiO_3$,[120] etc. have been shown to have good photocatalytic activities. As an efficient visible-light-active photocatalyst, 1D CdS nanostructures have also been studied.[121-126] For example, Jang et al. prepared CdS nanowires decorated with TiO_2 nanoparticles by solvothermal method and sol-gel synthesis, which can produce more hydrogen compared to pure CdS nanowires.[127] Other semiconductor 1D nanostructures have also been investigated, such as TiO_2 and ZnO.[128-131] Composites based on 1D nanostructures have also been constructed. Lv et al. synthesized a nanocomposite of $NaNbO_3$ nanorods and In_2O_3 nanoparticles, which showed improve photocatalytic hydrogen production under visible light irradiation and pure water splitting under UV irradiation (Figure 2.10).[132]

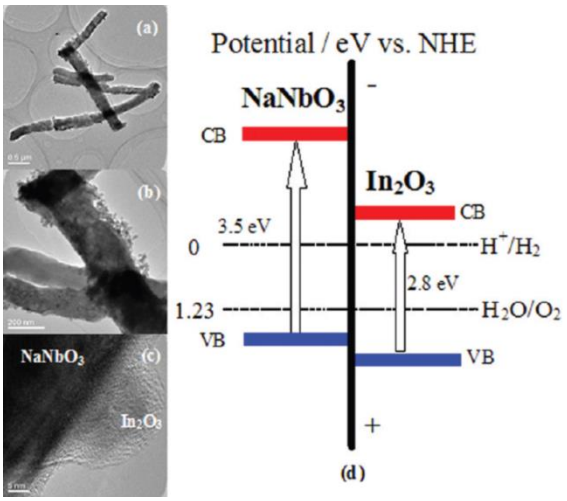

Figure 2.10 The TEM images (a,b) and HRTEM image (c) of the $NaNbO_3/In_2O_3$ nanocomposite, and its band structure diagram (d).[132]

2-dimensional nanosheets

The discovery of graphene inspires the exploration of other single-layered materials, that is, 2-dimensional (2D) nanosheets (NSs), synthesized via delamination of the layered precursors. However, single-layered materials are not new at all. The emergence of NSs dates back to the 1950s, when smectite-type clay minerals were reported to disperse well in water and yielded a colloidal suspension as a consequence of spontaneous exfoliation or delamination.[133-135]

The term “nanosheet” was first defined by Sasaki et al.[136] in 1996 when they were investigating the exfoliation process of a layered protonic titanate of lepidocrocite-type structure, $H_xTi_{2-x/4}O_4 \cdot H_2O$(x~0.7). “Nanosheet” reflects the ultimate 2D anisotropy, with extremely small thickness around 0.7 nm and lateral size from a few hundreds of nanometers to microns depending on the size of the precursor titanates. Following Sasaki’s findings, a wide variety of cation-exchangeable layered transition metal oxides and anion-exchangeable layered hydroxides, have been successfully delaminated into single host layers.[135, 137, 138]

To date, there are several groups of NSs: metal oxide NSs, layered double hydroxide (LDH) NSs, transition metal chalcogenide NSs and other types of NSs. Metal oxide NSs and carbon nitride NSs will be explained in detail in chapter 2.4.2. Notably, in 2011, Coleman et al. reported an easy method to exfoliate many transition metal dichalcogenides (TMDs) such as MoS_2, WS_2, $MoSe_2$, $MoTe_2$, $TaSe_2$, $NbSe_2$, $NiTe_2$ and other layered materials including BN and Bi_2Te_3.[139, 140] The elemental slabs of TMDs are typically composed of two layers of chalcogen atoms wrapping a hexagonal layer of metal atoms between them. Coleman et al. found that the exfoliation of those materials can be achieved by sonication in common solvents, among which N-methyl-pyrrolidone (NMP) and isopropanol (IPA) are most efficient. This method is thought to be scaled up to produce large quantities of exfoliated materials. TEM images and photographs of MoS_2, WS_2 and BN NSs are shown in Figure 2.11.

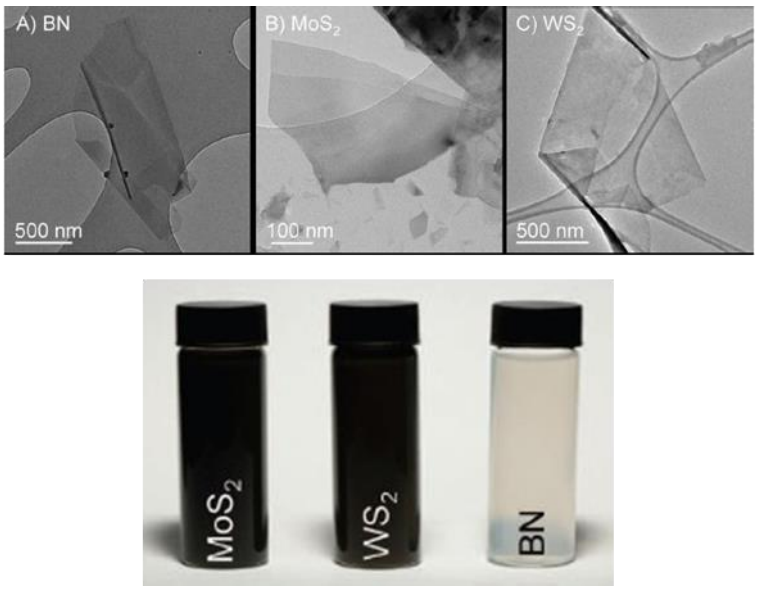

Figure 2.11 TEM images and photographs of MoS_2, WS_2 and BN NSs.[139]

2.4 Layered semiconductors and exfoliated nanosheets for photocatalysis

Layered materials form a very important large category of semiconductors for photocatalysis. These layered materials include metal oxides with layered structure ($SrTiO_3$, etc.), LDHs (Zn-Cr-LDH, etc.), transition metal chalcogenides (MoS_2, etc.), boron nitride (BN), graphitic carbon nitride (g-C_3N_4), etc. In general, ionic bonding or covalence bonding connected networks form the individual layers, with much weaker bondings holding different layers such as van der Waals force and weak ionic bonding. The unique structure of layered materials leads to some special advantages for photocatalysis.

Firstly, it is found that layered structure is beneficial to catalytic activity because the asymmetric structure can assist separation of electrons and holes.[141] For example, under atomic force micrograph (AFM), Matsumoto et al. observed that active sites for photo-reduction and photo-oxidation were located at different regions of a TiO_x NS with a lepidocropcite-type structure prepared from $K_{0.8}Ti_{1.73}Li_{0.27}O_4$.[142] The photo-reduction reactions, that is, photodepositions of Ag, Cu, and Cu_2O took place mainly at edges in the lateral direction of the TiO_x NS, while the photo-oxidation reactions, that is, photodeposition of MnO_2 occurred all over the surface. In addition, when studying the photophysical and photochemical properties of a layered semiconductor with perovskite structure, Miseki et al. found the selective photodepostion of Pt, Au, Ni and PbO_2 onto the basal or edge plane of $BaLa_4Ti_4O_{15}$.[143]

Secondly, water molecules can easily penetrate to the interlayer gallery of some layered semiconductors, so more active sites give rise to better photocatalytic activities. For example, Takata et al. reported that in a group of ion-exchangable layered perovskites with a formula of $A_{2-x}La_2Ti_{3-x}Nb_xO_{10}$ (A=interlayer cations such as K, Rb, Cs, etc.; x=0, 0.5, 1), H_2O molecules were oxidised to O_2 in the interlayer space while protons were reduced to H_2 at the surface where Ni/NiO was present.[144] Moreover, Domen et al. found that for a group layered perovskite niobates, $A(_{Mn-1}Nb_nO_{3n+1})$ (A=Na, K, Rb, Cs; M=La, Ca, etc.), the proton-exchanged form exhibited better water splitting performance as the enlarged interlayer spacing allowed reactants such as H_2O and methanol to move into the interlayer spaces.[145]

Thirdly, the relative large interlayer spacing also greatly facilitates the doping process of layered semiconductors as the the dopant source can easily diffuse to interlayer space. As a result, homogeneous doping can be achieved. Using ammonia gas as the nitrogen

source, Liu et al. demonstrated the bulk doping of a layered titanate, $Cs_{0.68}Ti_{1.83}O_4$, via a calcination process.[146] Similar method was applied to prepared N-doped $Ba_5Ta_4O_{15}$,[147] N-doped $Sr_2Ta_2O_7$,[148] N-doped $CsCa_2Ta_3O_{10}$,[149] etc.

Last but not least, the weak interlayer bonding in some layered materials provides the possibility of exfoliating the bulk materials to ultrathin NSs.[138, 150]

Here we will mainly discuss two main types of layered materials: transition metal oxides and carbon nitride.

2.4.1 Layered semiconductors

2.4.1.1 Transition metal oxides

Among layered transition metal oxides, perovskites are the most reported in terms of crystal structure. As shown in Figure 2.12, Osterloh summarized layered materials with perovskite structure in several groups including (110), (100) and (111) layered perovskites.[2] (110) layered perovskites with a generic composition of $A_mB_mO_{3m+2}$ (m=4,5; A= Ca, Sr, La; B= Nb, Ti), was discovered by Hwang et al.[151] They contain perovskite slabs parallel to (110) direction. Domen's group[152-154] first reported (100) layered structure perovskites including $A_4Nb_6O_{17}$ (A= K, Rb, Cs), with stacked niobate sheets along the b-axis of an orthorhombic unit cell. $ACa_2Nb_3O_{10}$, where A is an alkali metal, with a typical Dion-Jacobson-type perovskite structure, was first studied by Dion et al.[155] In this structure, the alkali metal ions lie between perovskite slabs composed of corner-sharing NbO_6 octahedra and Ca ions[156]. As a group of (111) layered perovskites, Aurivillius perovskites have a general formula of $(Bi_2O_2)^{2+}(A_{m-1}B_mO_{3m+1})^{2-}$, and contain m perovskite units sandwiched between bismuth oxide layers, where A and B are the two kinds of cations which enter the perovskite unit.[157, 158]

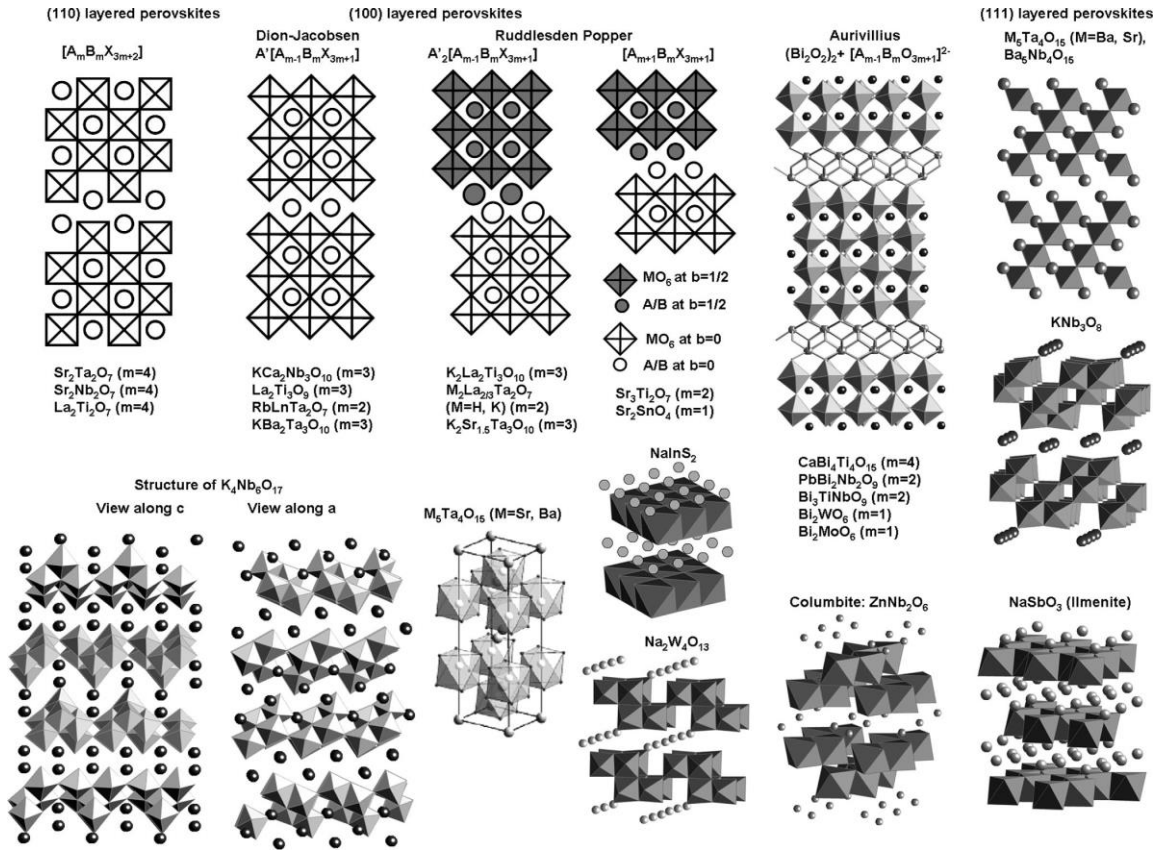

Figure 2.12 Crystal structure of layered perovskites.[2]

With regards to the composition of transition metal oxides, titanates are the most intensively investigated group, which are formed via fusion between TiO_2 and other metal oxides. Some titanates are able to achieve either H_2 or O_2 production. For example, Ishikawa et al.[159, 160] systematically studied oxysulfides $Ln_2Ti_2S_2O_5$ (Ln = Pr, Nd, Sm, Gd, Tb, Dy, Ho and Er), and the series of oxysulfides could evolve H_2 or O_2 from aqueous solution in the presence of a sacrificial electron donor (Na_2S-Na_2SO_3 or methanol) or acceptor (Ag^+) respectively under visible light (420-650 nm). They all have narrow band gaps, as shown in Table 2.1. Moreover, they are stable against photocorrosion while other photocatalysts containing S^{2-} are often subject to photodegradation due to the oxidation of S^{2-} by photoexcited holes. $Sm_2Ti_2S_2O_5$, which possesses the structure of Ruddlesden-Popper-type layered perovskite (*I4/mmm* group), has the highest quantum efficiency, 1.1% and 0.1% for O_2 and H_2 evolution, respectively. More importantly, some titantates are able to achieve overall water splitting under certain conditions. For instance, Thaminimulla et al.[161] introduced Ni and Cr oxide into $K_2La_2Ti_3O_{10}$ by co-impregnation method, and a composition of Cr (0.5 wt%)–Ni (3.0 wt%)–$K_2La_2Ti_3O_{10}$ was able to decompose KOH solution into H_2 and O_2 stoichiometrically with high evolution rates of 885 and 442 $\mu mol \cdot h^{-1}$ under λ>190 nm.

Table 2.1 Band gaps of $Ln_2Ti_2S_2O_5$.

Compound	Band gap (eV)
$Sm_2Ti_2S_2O_5$	2.13
$Gd_2Ti_2S_2O_5$	2.09
$Tb_2Ti_2S_2O_5$	2.04
$Dy_2Ti_2S_2O_5$	2.00
$Ho_2Ti_2S_2O_5$	1.98
$Er_2Ti_2S_2O_5$	1.94

$SrTiO_3$ is one of the most studied titanates, which crystallizes in a peroskite type layered structure with a band gap of 3.2 eV. $SrTiO_3$ is very active for hydrogen evolution, due to its high CBM. In order to extend its light absorption to the visible spectrum, some researchers tried to dope $SrTiO_3$, especially with metal ions. For instance, Yu et al. synthesized Cr-doped $SrTiO_3$ via sol-gel hydrothermal method, which exhibited H_2 evolution rate of 82.6 $\mu mol \cdot h^{-1}$ (methanol solution, <540 nm).[16] Konta et al. [162] doped $SrTiO_3$ with noble metal ions (Mn, Ru, Rh, Ir etc.), giving a adsorption shoulder in the visible region as shown in Figure 2.13, which is indicative of a localized level in the band gap. $SrTiO_3$ doped with 0.5% Rh has the highest H_2 evolution rate of 17.2 $\mu mol \cdot h^{-1}$ while that doped with 0.5% Ru has the highest O_2 evolution rate of 3.9 $\mu mol \cdot h^{-1}$ under visible light. Doping $SrTiO_3$ with one single metal element often causes instability as a result of charge imbalance, so codoping with two elements of different valences has been studied. For example, Niishiro et al. [163] co-doped $SrTiO_3$ with nickel and tantalum or niobium in order to achieve charge compensation as Ni possess lower valence number than Ti. Exploiting the same mechanism, Kato et al. [164] codoped $SrTiO_3$ with antimony and chromium and successfully extended the photocatalytic hydrogen evolution activity to visible region.

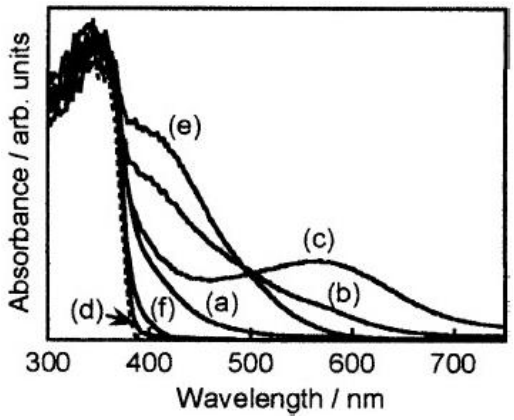

Figure 2.13 Diffuse reflectance spectra of $SrTiO_3$:M(0.5%). M= (a) Mn, (b) Ru, (c) Rh, (d) Pd, (e) Ir, and (f) Pt. A broken line represents a spectrum of nondoped $SrTiO_3$.[162]

2.4.1.2 Carbon nitride

Since the pioneer work on using graphitic carbon nitride (g-C_3N_4) for photocatalytic water splitting reported by Wang et al.[165], g-C_3N_4, a polymer semiconductor has drawn great attention as a promising metal-free photocatalyst due to its visible light absorption, suitable band position for both H_2 and O_2 production, and relatively good thermal and chemical stability.[166] g-C_3N_4 is the most stable allotrope of carbon nitride with tri-s-triazine as the repeating unit.[167] Since the s-triazine ring (C_3N_3) is aromatic, π-conjugated planar layers tend to be formed, which gives a similar structure as graphite.[13, 168, 169] In the structure of g-C_3N_4, the tri-s-triazine units are bridged by N atoms, as shown in Figure 2.14.

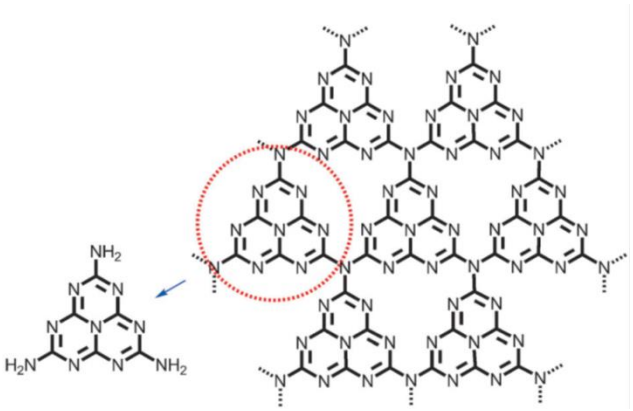

Figure 2.14 Structure of g-C_3N_4.[166]

Pyrolysis of cyanamide, dicyandiamide or melamine is generally used to synthesize g-C_3N_4, which usually exhibits a colour of yellow. However, the absorption edge may be varied depending on the preparation process, including the type of precursors, polycondensation temperature, treatment time, atmosphere, etc. The synthesis condition

may affect the packing density, defects or local structure, and thus the optical absorption.[166, 170, 171] The corresponding band gaps of g-C_3N_4 range from 2.3 to 2.8 eV.

The optical properties g-C_3N_4 of can be modified through doping. For example, Liu et al. successfully doped g-C_3N_4 with S through a calcination process in H_2S gas flow.[172] It was found that the band gap of g-C_3N_4 was increased from 2.73 to 2.85 eV after S doping, with both CBM and VBM upshifted. However, when g-C_3N_4 was doped with other elements such as P, F, etc., the band gap was often reduced. For instance, using 1-butyl-3-methylimidazolium hexafluorophosphate (BmimPF_6) as a mild phosphorus source, Zhang et al. doped g-C_3N_4 with P, which not only greatly extended its visible light absorption, but also improved the electric conductivity.[173] Wang et al. prepared fluorinated g-C_3N_4 by incorporating NH_4F to the condensation process.[174] The band gap was slightly decreased after fluorination, and the photocatalytic activity was increased with the larger amount of fluorine. In addition, Niu et al. introduced nitrogen vacancies to g-C_3N_4 through elevating the condensation temperature.[175] The nitrogen-deficient g-C_3N_4 possessed smaller band gap (2.66 eV) compared to the normal one (2.74 eV), and showed enhanced photocatalytic activities.

In order to suppress the charge recombination of g-C_3N_4 and to improve the light absorption, a number of composites were also constructed. Hybridizing g-C_3N_4 with other semiconductors provides an effective way to improve photocatalytic activities thanks to the charge transfer between g-C_3N_4 and other semiconductors. For example, a composite of g-C_3N_4 and Bi_2WO_6 showed enhanced visible light-induced photocatalytic degradation of methyl orange (MO).[176] Pan et al. synthesized a $BiPO_4$@C_3N_4 core-shell structured composite, which showed impressive improvement for photocatalytic degradation of methylene blue (MB).[177] A chemisorption method was used by Wang et al. to prepare ZnO hybrized by C_3N_4, and the photocurrent of ZnO was enhanced by 5 times under UV light irradiation.[178] Other than C_3N_4-semiconductor composites, C_3N_4-polymer hybrids were also found to have advantages for photocatalysis. For instance, a polymer composite of g-C_3N_4 and poly(3-hexylthiophene) (P3HT) prepared by Yan et al. showed a hydrogen production rate 300 times of the rate of g-C_3N_4.[179] Sui et al. reported that the hydrogen production activity of g-C_3N_4 from pure water was increased up to 50 times when conductive polymer polypyrrole (PPy) nanoparticles were loaded.[180] In addition, loading g-C_3N_4 with metal nanoparticles such as Au and Ag was also found to promote photocatalytic activities.[181, 182]

2.4.2 Exfoliation of layered semiconductors

As mentioned in chapter 2.3.3, through the exfoliation of layered materials, a number of ultrathin NSs can be obtained.

2.4.2.1 Metal oxide nanosheets

Typical synthesis process of metal oxide NSs is achieved via chemical exfoliation of a parental layered precursor in an exfoliating solution, as a result of extremely high degree of swelling and simultaneously weakened interaction between the layers, as shown in Figure 2.15. Several factors can affect the exfoliation process: composition of the host layers, the layer charge density, the ionic species between host layers, exfoliating solution etc. Careful controlling of these factors can lead to high degree of swelling of the host layers and finally single elemental layers under mechanical assistance such as shaking or ultra-sonication.[135]

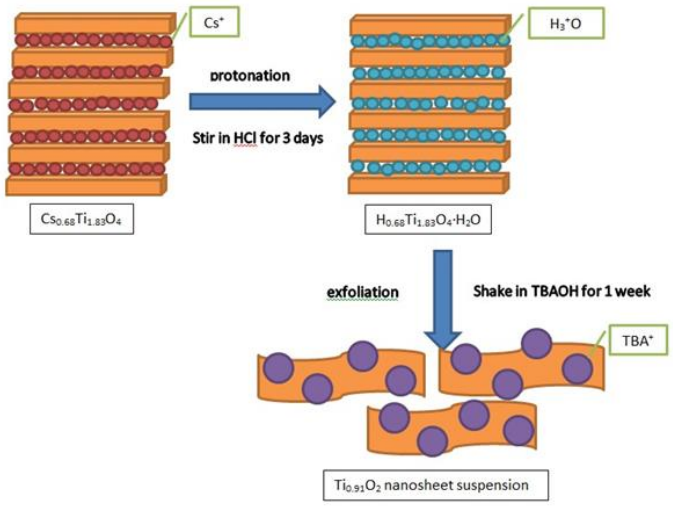

Figure 2.15 Typical synthesis process of $Ti_{0.91}O_2$ NSs.

So far, a wide variety of layered oxides have been delaminated to single layer oxide NSs, such as $Cs_{0.7}Ti_{1.825}O_4$,[136] $K_{0.45}MnO_2$,[183] $K_4Nb_6O_{17}$,[184] and $Na_{0.9}Mo_2O_4$.[185] These layered precursors are usually composed of stacked negatively charged layers with MO_6 (M=Ti, Mn, Nb etc.) octahedrons sharing corners or edges, and alkali metal ions (Cs, K, Na). They all have cation exchangeability, which enables intercalation of other ions into the galleries without changing the structure of the layers at room temperature. A three-step soft chemistry exfoliation process has been well established: the layered precursors are first synthesized via solid state reaction at high temperature; then they are treated with acid for a few days, giving a protonic hydrated form, e.g. $H_{0.7}Ti_{1.825}O_4 \cdot H_2O$; finally, shaking

the protonic precursors in exfoliating solutions which contain bulky organic cations, typically TBAOH (tetrabutylammonium hydroxide) solution, will produce the NSs suspension. Via this process, a number of metal oxide NSs have been obtained, which have been summarized in Table 2.2. Structures of several typical oxide NSs are shown in Figure 2.16. Most of the metal oxide NSs contain d^0 transition metal, which gives them valence band composed of O 2p and conduction band composed of empty d orbitals.[140, 186]

Those negatively charged NSs are covered with electrical double layers, and the electrical repulsion between NSs gives stable colloidal suspension. The good dispersibility of the NSs can be verified by a clear Tyndall light scattering effect. The size of NSs is generally determined by parental layered materials: the thickness depends on the intrinsic crystallographic thickness of the host slabs, while the lateral size is controllable by changing the crystal size of the precursors. For example, Tanaka et al. have synthesized large size titania NSs (~4 mm), starting with the synthesis of single crystal $K_{0.8}Ti_{1.73}Li_{0.27}O_4$ through flux growth method.[187]

Table 2.2 Reported materials of oxide NSs.[138]

Ti oxide	$Ti_{0.91}O_2$, $Ti_{0.87}O_2$, Ti_3O_7, Ti_4O_9, Ti_5O_{11},$Ti_{1-x}Co_xO_2$ ($x \leq 0.2$), $Ti_{1-x}Fe_xO_2$ ($x \leq 0.4$), $Ti_{1-x}Mn_xO_2$ ($x \leq 0.4$), $Ti_{0.8-x/4}Fe_{x/2}Co_{0.2-x/4}O_2$ ($x=0.2, 0.4, 0.6$)
Mn oxide	MnO_2, Mn_3O_7, $Mn_{1-x}Co_xO_2$ ($x \leq 0.4$),$Mn_{1-x}Fe_xO_2$ ($x \leq 0.2$)
Ti-Nb oxide	$TiNbO_5$, Ti_2NbO_7
Ti-Ta oxide	$TiTaO_5$
Nb oxide	Nb_3O_8, Nb_6O_{17}
Ta oxide	TaO_3
layered perovskite	$LaNb_2O_7$, $La_{0.90}Eu_{0.05}Nb_2O_7$, $Eu_{0.56}Ta_2O_7$,$SrTa_2O_7$, $Bi_2SrTa_2O_9$, $Ca_2Nb_3O_{10}$,$Sr_2Nb_3O_{10}$, $NaCaTa_3O_{10}$, $CaLaNb_2TiO_{10}$,$La_2Ti_2NbO_{10}$, $Ba_5Ta_4O_{15}$, W_2O_7
Ru oxide	$RuO_{2.1}$
W oxide	$Cs_4W_{11}O_{36}$

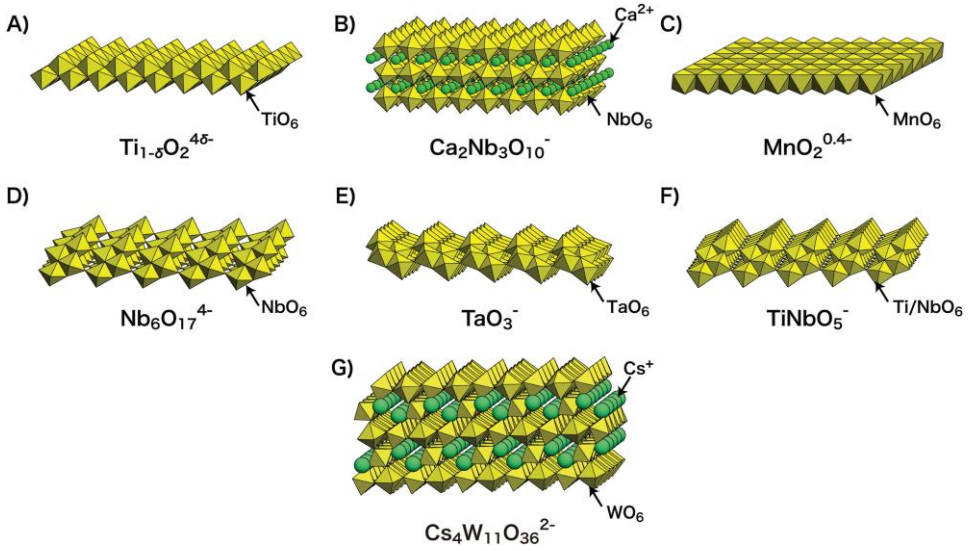

Figure 2.16 Structure of several typical oxide nanosheets.[135]

Of all those various metal oxide NSs, $Ti_{0.91}O_2$ is the most and best studied NS. The parental caesium titanate, $Cs_{0.68}Ti_{1.83}O_4$, has a lepidocrocite-type body-centered orthorhombic layered structure, with Cs^+ occupying 70% of the pseudocubic sites inside the host slabs. In the crystal structure of $Cs_{0.68}Ti_{1.83}O_4$, two layers of the network of TiO_6 octahedra sharing four edges are nested into a zigzag sheet as the structure unit, and that is also the basic unit of anatase titania.[146] The parental titanate can be converted to protonated forms by cation-exchange process with H^+. Sasaki et al.[188, 189] studied the exfoliation process of $H_{0.68}Ti_{1.83}O_4 \cdot H_2O$ by nearly infinite osmotic swelling in TBAOH solution. In the exfoliation process, bulky TBA^+ cations will replace the interlayer H_3O^+ ions, expanding the spacing until complete delamination. The ratio of TBA^+/H^+ greatly affects the exfoliation process. A ratio of 0.5-5 is found to be favourable for complete delamination, above which only swelling happens.

$Ti_{0.91}O_2$ NSs were further studied by Gateshki et al.[190] and Sasaki's group[186, 191-194] concerning the crystal structure, band structure, crystallization in restacking process and other properties. The architecture of $Ti_{0.91}O_2$ is illustrated in Figure 2.17, composed of octahedra at different levels in the b-axis sharing the edges with a thickness of 0.75 nm. Vacancies at some Ti sites make the NSs negatively charged. Band structure of the NSs is shown in Figure 2.18, in which a larger band gap can be observed than anatase due to the quantum size effect. The enlarged band gap is accompanied by a blue-shift in the UV-Vis absorption spectrum, as shown in Figure 2.19.

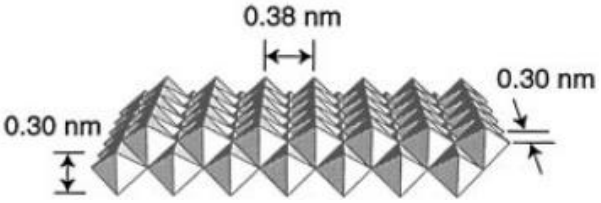

Figure 2.17 Architecture of $Ti_{0.91}O_2$ crystallites.[194]

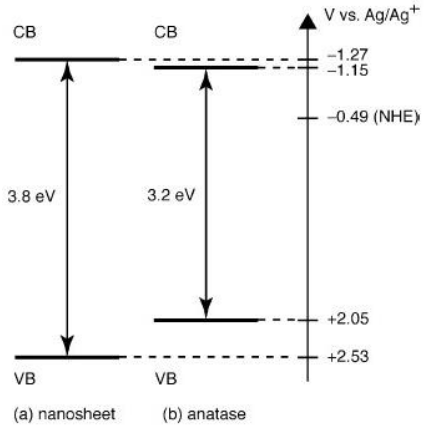

Figure 2.18 Band structures of $Ti_{0.91}O_2$ NSs and anatase.[192]

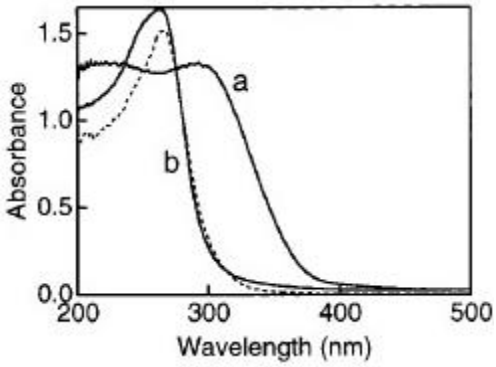

Figure 2.19 UV-visible spectra of (a) the protonic layered titanate $H_{0.68}Ti_{1.83}O_4 \cdot H_2O$ and (b) a film of NSs on a SiO_2 glass substrate. The former was recorded in a diffuse reflectance mode and the latter in a transmission. The data for the colloidal suspension is denoted by a dashed trace.[194]

The chemical composition and band structures of titania NSs can also be tailored through doping. For instance, Liu et al. prepared N-doped $Ti_{0.91}O_2$ NSs through exfoliation of an N-doped titanate precursor, $Cs_{0.68}Ti_{1.83}O_{4-x}N_x$.[195] The N-doped $Ti_{0.91}O_2$ NSs exhibited improved visible light absorption compared to the undoped counterpart. Dong et al. reported titania NSs codoped with binary transition metal ions including Mn and Fe, and the optical absorption can gradually be controlled with different ratios of dopants.[196]

2.4.2.2 Carbon nitride nanosheets

Its laminar structure triggers the interest of exfoliating bulk g-C_3N_4 to form graphene-like carbon nitride NSs, which can potentially exhibit special electronic and optical properties. In order to synthesize g-C_3N_4 NSs, both bottom-up[197] and top-down[171, 198, 199] methods have been investigated, but top-down methods remain to be prevalent. In top-down synthesis processes, bulk g-C_3N_4 is first prepared via thermal condensation before being exfoliated through chemical, thermal or other reactions. For example, Niu et al. found that g-C_3N_4 NSs with thickness of 1.65 to 2.62 nm can be obtained via a thermal oxidation etching process.[170] Moreover, sonication in different solvents such as H_2O, isopropanol, 1,3-butanediol etc. provides a facile way to delaminate bulk g-C_3N_4 to NSs of several atomic layers with thickness ranging from 1 nm to 2.5 nm.[171, 198, 200] As shown in Figure 2.20, Yang et al. obtained g-C_3N_4 NSs with an average thickness of 2 nm via sonication in isopropanol.[171] Zhao et al. combined both thermal oxidation and sonication in methanol, and successfully prepared single-atomic-layered g-C_3N_4 NSs with thickness of 0.4-0.5 nm.[199] In addition, Xu et al. also obtained single-atomic-layered g-C_3N_4 NSs by intercalation of H_2SO_4 molecules in the interplanar space and subsequent exfoliation in H_2O.[201]

Despite the fact that the aforementioned g-C_3N_4 NSs possess dramatically expanded surface area, improved electrical conductivity and altered energy band structures, the optical absorption edge was generally blue-shifted due to the enlargement of band gap.[170, 198, 201] The enlarged band gap will inevitably limit the visible light absorbance of g-C_3N_4 NSs.

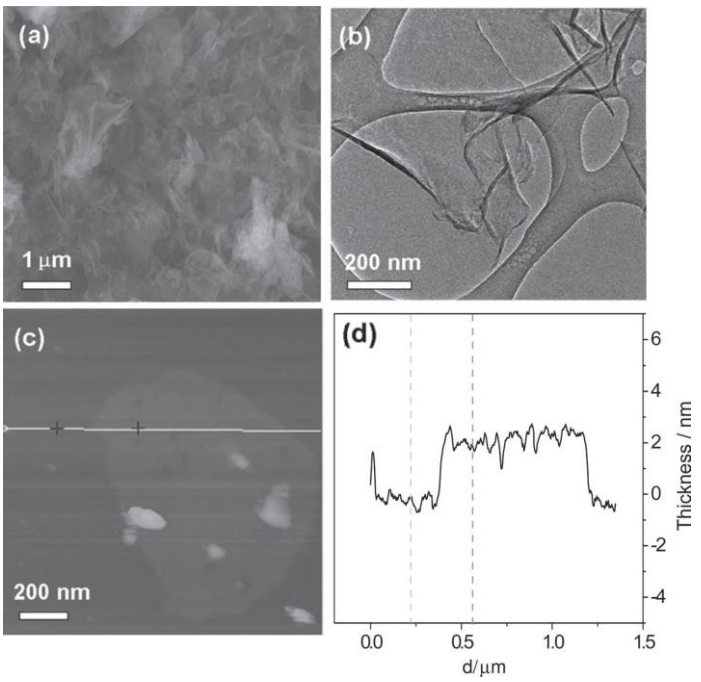

Figure 2.20 a,b) Typical FE-SEM (a) and TEM (b) images reveal the flexible g-C_3N_4 NSs with the size from 500 nm to several micrometers. c, d) Representative AFM image (c) and corresponding thickness analysis (d) taken around the white line in (c) reveal a uniform thickness of about 2 nm for g-C_3N_4 NSs.[171]

2.4.3 Nanostructures built from nanosheets

The diversity of 2D semiconductor NSs and their unique physicochemical properties open up great opportunities of developing novel heterogeneous nanostructures. Through hybridization of NSs with a great variety of guest species with different strategies, significant progress has been made in building nanocomposites for wide applications such as photocatalysis, photoelectrochemical devices, energy storage, electronic/optoelectric devices, etc.[150, 202] The nanoassemblies based on 2D NSs can be categorized to three groups: surface anchoring, exfoliation-restacking and layer-by-layer (LBL) assembly.

2.4.3.1 Surface anchoring

The extremely large surface area of NSs provides not only abundant anchoring sites for guest nanoparticles, but also nucleation sites for the in-situ growth of nanoparticles. As we discussed in chapter 2.3.2, graphene has been extensively studied as the support of various guest particles since it not only provides a good scaffold to graft nanoparticles, but also works as the cocatalyst in some cases.[203] Unlike graphene, studies on grafting nanoparticles onto semiconductor NSs are still limited. Maeda et al. prepared negative-charged potassium hexaniobate nanoscrolls (NS-$K_4Nb_6O_{17}$) via exfoliation of $K_4Nb_6O_{17}$,

which adsorbed cationic dye tris(2,2′-bipyridyl)ruthenium(II) chloride ($Ru(bpy)_3^{2+}$) on the surface.[204] The dye-grafted nanoscrolls allowed for rapid generation of photoinduced electrons and efficient hydrogen production. Similar method was also used to prepare hexaniobate nanoscrolls (NS-$H_4Nb_6O_{17}$) and acid-restacked calcium niobated NSs (R-$HCa_2Nb_3O_{10}$) adsorbed with ($Ru(bpy)_3^{2+}$) dye.[205] Moreover, Kim et al. grew Au nanoparticles onto MoS_2 and WS_2 NSs through a spontaneous redox reaction, and found that Au preferentially grew at the surface defect sites.[206]

2.4.3.2 Exfoliation-restacking

Hata et al. reported a general method to intercalate Au NPs into galleries of layered materials such as Dion-Jacobson layered perovskite $HCa_2Nb_3O_{10}$ via pre-intercalation of TBAOH and polyallylamine (PAA) to enlarge the interlayer space.[207] This general method promises to be a simpler method of embedding guest nanoparticles into layered semiconductor matrix. Nevertheless, the size of nanoparticles is greatly restricted because the degree of gallery expansion is very limited.

An exfoliation-restacking method has been developed to address the issues of the abovementioned intercalation method, which involves the electrostatic attraction of the NSs and guest nanoparticles and the restacking of the NSs. Compared to the intercalation method, exfoliation-restacking shows two major advantages: the sizes of guest particles are much more flexible; the choice of nanoparticle species is significantly broader. For instance, as the metal oxide NSs possess negative surface charges, nanoparticles with positive charges can be directly absorbed onto the NSs while negatively charged nanoparticles can be linked to the NSs through organic polycations. Through this exfoliation-restacking method, a pillared structure is often obtained, with NSs randomly stacked upon each other and guest nanoparticles sandwiched between NSs.

During the 2000s, Choy et al. conducted a number of pillaring experiments for photocatalytic purpose, and some functional species including chromia, iron oxide, nickel oxide, anatase RuS_2 etc. were introduced into pillared titania NSs structure.[42, 208-216] Nano-sized anatase particles were first introduced into titanate interlayer galleries via the interaction between anatase nanosol solution and $Ti_{0.91}O_2$ NSs suspension in Choy's work.[209, 210, 214, 215] After pillaring, the interlayer spacing was expanded to 4.36 nm from 0.92 nm of $H_{0.68}Ti_{1.83}O_4 \cdot H_2O$. From nitrogen adsorption-desorption isotherm, a microporous structure was revealed. A red shift of UV-Vis absorption spectroscopy and

better photocatalytic properties under UV spectrum can be observed for the pillared titanate.

Apart from anatase nanoparticles, other metal oxide including Cr, Zn, Fe and Ni oxide were used for pillaring titania NSs by interacting NSs suspension with metal acetate, which gave the nanohybrids visible light absorbance and stability.[42, 211, 213, 217, 218] Cu oxide was also pillared into layered titanate, and Cu exhibited both monovalency and divalency.[219] Upon calcination, the nanohybrid structure transformed to rutile and then anatase in different temperature range. Choy et al. also fabricated other pillared structures via the exfoliation-restacking method, such as RuS_2 pillared titanate,[220] TiO_2 pillared MoS_2,[208] ZnO pillared MnO_2[221] and so on. Similarly, Kim et al. synthesized a nanocomposite of rGO NSs and TiO_2 nanoparticles through the electrostatic assembly of the oppositely charged NSs and nanoparticles.[222]

The versatility of the exfoliation-restacking method allows not only the fabrication of composites of NSs and nanoparticles, but also the self-assembly of different NSs. For example, Gunjakar et al. reported a mesoporous nanohybrid of positively charged Zn-Cr-LDH NSs and negatively charged titanate NSs, as shown in Figure 2.21.[223] This nanohybrid showed not only enhanced photocatalytic activities but also improved chemical stability.

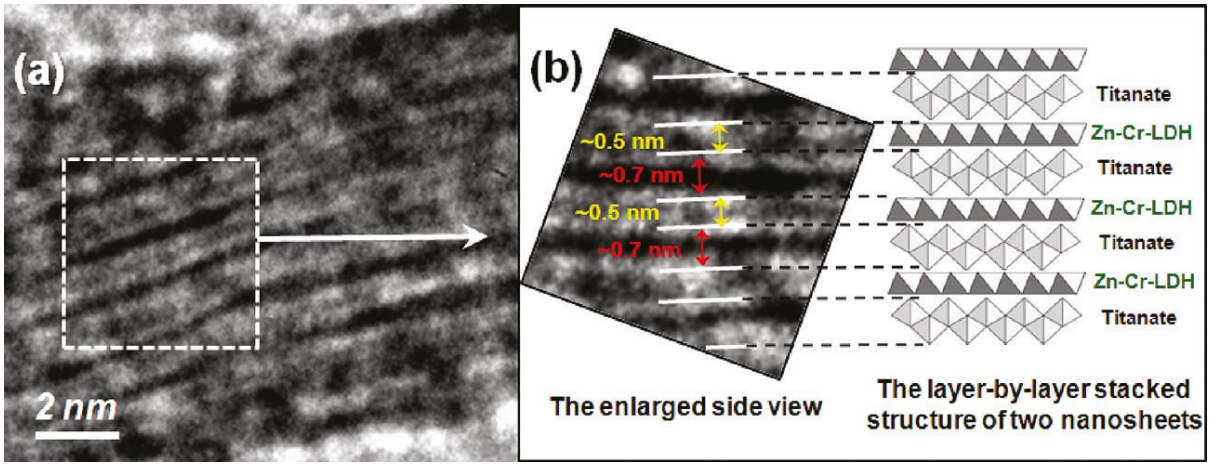

Figure 2.21 (a) Cross-sectional HR-TEM image of the Zn-Cr-LDH-titanate nanohybrid and (b) its enlarged view and structural model.[223]

2.4.3.3 Layer-by-layer (LBL) assembly

Due to their negative surface charge, transition metal oxide NSs such as $Ti_{0.91}O_2^{-0.36}$ and $MnO_2^{-0.4}$ can be used for electrostatic LBL self-assembly via sequential adsorption onto

different substrates.[135, 138] In a LBL process, colloidal NSs can be combined with oppositely charged species including organic polyelectrolytes such as polyethyleneimine (PEI) and polyaniline (PANI).[195, 224] For example, Sakai et al.[225] synthesized hybrid films with $Ti_{0.91}O_2$ NSs and MnO_2 NSs using PEI as binding agent.

Besides organic polyelectrolytes, the oppositely charged species used in LBL can also be other charge-carrying particles. For instance, Zhou et al.[226] assembled multilayered hybrid film with alternating $Ti_{0.91}O_2$ NSs and silver metal particles. By exploiting LBL method and using spherical poly-methylmethacrylate (PMMA) as templates, Wang et al.[227] successfully prepared hollow shells with titania NSs pillared by aluminium Keggin ions. In addition, Wang et al.[228] reported films of titania NSs and Ru complexes via LBL.

Interesting features can also be introduced to LBL assembly via selecting some polyelectrolytes. For instance, Seger et al. fabricated an n-type to p-type swithable photoelectrode via LBL assembly of titania NSs and PANI, as shown in Figure 2.22.[224] PANI itself can switch from an n-type to p-type semiconductor, but Seger's work demonstrated the possibility of altering the photoelectrical performance of the PANI-titania film by simply changing the electrolyte.

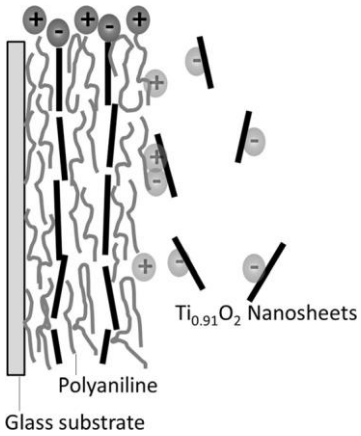

Figure 2.22 Layer-by-layer deposition of the PANI-titania film.[224]

2.5 Summary

Despite of the great variety of photocatalysts studied to date, the overall energy conversion efficiency is still quite low due to several reasons including quick recombination of charge carriers, limited light absorption in the visible region, poor photo-stability in the aqueous reaction environment, etc.

The diversity of layered semiconductors and exfoliated 2D NSs and their unique properties open up enormous possibilities of fabricating novel nanostructured photocatalysts for water splitting. In particular, by using 2D NSs as the building blocks, a number of heterogeneous materials can be designed in order to overcome the disadvantages of traditional photocatalysts.

First, due to their asymmetric structure, layer-structured semiconductors can possess separate reduction and oxidation sites, facilitating charge separation. At the same time, thanks to the single crystallinity within the 2D NSs, the confined charge transfer in the 2D direction can be greatly improved. As for nanohybrids based on NSs, proper band alignment will allow the charge transfer between different semiconductors, thus making reduction and oxidation reactions take place at different semiconductors.

Second, by hybridizing layered semiconductors or NSs with small band-gap light absorbers, the optical absorption in the visible region can be effectively improved. As different components can absorb varied spectrum of solar light, the hybrids can utilize the overall solar spectrum more efficiently. In the meanwhile, the problem that recombination centres may be introduced in doped semiconductors can be avoided.

In addition, semiconductors with layered structure essentially have more active sites as reactant molecules can penetrate into the interlayer spacing. In the nanohybrids formed with NSs, a mesoporous structure is often obtained, in which the interlayer spacing between nanosheets is expanded, facilitating photocatalytic reactions.

2.6 References

1. K. Maeda and K. Domen, *Chem. Mater.*, 2010, **22**, 612-623.

2. F. E. Osterloh, *Chem. Mater.*, 2007, **20**, 35-54.

3. A. Kudo and Y. Miseki, *Chem. Soc. Rev.*, 2008, **38**, 253-278.

4. X. Chen, S. Shen, L. Guo and S. S. Mao, *Chem. Rev.*, 2010, **110**, 6503-6570.

5. M. Ni, M. K. H. Leung, D. Y. C. Leung and K. Sumathy, *Renew. Sust. Energ. Rev.*, 2007, **11**, 401-425.

6. K. Sayama and H. Arakawa, *J. Chem. Soc., Faraday Trans.*, 1997, **93**, 1647-1654.

7. Z. Xing, Z. Chen, X. Zong and L. Wang, *Chem. Commun.*, 2014, **50**, 6762-6764.

8. G. L. Chiarello, E. Selli and L. Forni, *Appl. Catal., B*, 2008, **84**, 332-339.

9. E. Bae and W. Choi, *Environ. Sci. Technol.*, 2003, **37**, 147-152.

10. I. M. Arabatzis, T. Stergiopoulos, D. Andreeva, S. Kitova, S. G. Neophytides and P. Falaras, *J. Catal.*, 2003, **220**, 127-135.

11. X. Zong, H. Yan, G. Wu, G. Ma, F. Wen, L. Wang and C. Li, *J. Am. Chem. Soc.*, 2008, **130**, 7176-7177.

12. X. Zong, G. Wu, H. Yan, G. Ma, J. Shi, F. Wen, L. Wang and C. Li, *J. Phys. Chem. C*, 2010, **114**, 1963-1968.

13. K. Maeda, X. C. Wang, Y. Nishihara, D. L. Lu, M. Antonietti and K. Domen, *J. Phys. Chem. C*, 2009, **113**, 4940-4947.

14. K. Ikarashi, J. Sato, H. Kobayashi, N. Saito, H. Nishiyama and Y. Inoue, *J. Phys. Chem. B*, 2002, **106**, 9048-9053.

15. R. Li, F. Zhang, D. Wang, J. Yang, M. Li, J. Zhu, X. Zhou, H. Han and C. Li, *Nat. Commun.*, 2013, **4**, 1432.

16. H. Yu, S. Ouyang, S. Yan, Z. Li, T. Yu and Z. Zou, *J. Mater. Chem.*, 2011, **21**, 11347-11351.

17. X. Zong, Z. Xing, H. Yu, Z. Chen, F. Tang, J. Zou, G. Q. Lu and L. Wang, *Chem. Commun.*, 2011, **47**, 11742-11744.

18. Z. Xing, X. Zong, J. Pan and L. Wang, *Chem. Eng. Sci.*, 2013, **104**, 125-146.

19. G. Liu, L. Wang, H. G. Yang, H. M. Cheng and G. Q. M. Lu, *J. Mater. Chem.*, 2009, **20**, 831-843.

20. L. Wu, J. C. Yu and X. Z. Fu, *J. Mol. Catal. A: Chem.*, 2006, **244**, 25-32.

21. L. Spanhel, H. Weller and A. Henglein, *J. Am. Chem. Soc.*, 1987, **109**, 6632-6635.

22. M. Higashi, R. Abe, K. Teramura, T. Takata, B. Ohtani and K. Domen, *Chem. Phys. Lett.*, 2008, **452**, 120-123.

23. Y. Sasaki, H. Nemoto, K. Saito and A. Kudo, *J. Phys. Chem. C*, 2009, **113**, 17536-17542.

24. A. Iwase, Y. H. Ng, Y. Ishiguro, A. Kudo and R. Amal, *J. Am. Chem. Soc*, 2011, **133**, 11054-11057.

25. K. Maeda, M. Higashi, D. Lu, R. Abe and K. Domen, *J. Am. Chem. Soc.*, 2010, **132**, 5858-5868.

26. K. Maeda, R. Abe and K. Domen, *J. Phys. Chem. C*, 2011, **115**, 3057-3064.

27. M. Tabata, K. Maeda, M. Higashi, D. Lu, T. Takata, R. Abe and K. Domen, *Langmuir*, 2010, **26**, 9161-9165.

28. H. Tada, T. Mitsui, T. Kiyonaga, T. Akita and K. Tanaka, *Nat. Mater.*, 2006, **5**, 782-786.

29. J. Yang, H. Yan, X. Wang, F. Wen, Z. Wang, D. Fan, J. Shi and C. Li, *J. Catal.*, 2012, **290**, 151-157.

30. J. Yang, D. Wang, H. Han and C. Li, *Acc. Chem. Res.*, 2013, **46**, 1900-1909.

31. R. Li, H. Han, F. Zhang, D. Wang and C. Li, *Energy Environ. Sci.*, 2014, **7**, 1369-1376.

32. X. Wang, L. Yin, G. Liu, L. Wang, R. Saito, G. Q. M. Lu and H.-M. Cheng, *Energy Environ. Sci.*, 2011, **4**, 3976-3979.

33. A. Fujishima and K. Honda, *Nature*, 1972, **238**, 37-38.

34. W. T. Sun, Y. Yu, H. Y. Pan, X. F. Gao, Q. Chen and L. M. Peng, *J. Am. Chem. Soc.*, 2008, **130**, 1124-1125.

35. D. R. Baker and P. V. Kamat, *Adv. Funct. Mater.*, 2009, **19**, 805-811.

36. W. Siripala, A. Ivanovskaya, T. F. Jaramillo, S. H. Baeck and E. W. McFarland, *Sol. Energy Mater. Sol. Cells*, 2003, **77**, 229-237.

37. Y. Bessekhouad, D. Robert and J. V. Weber, *Catal. Today*, 2005, **101**, 315-321.

38. L. X. Yang, S. L. Luo, Y. Li, Y. Xiao, Q. Kang and Q. Y. Cai, *Environ. Sci. Technol.*, 2010, **44**, 7641-7646.

39. J. Hensel, G. M. Wang, Y. Li and J. Z. Zhang, *Nano Lett.*, 2010, **10**, 478-483.

40. Y. L. Lee, C. F. Chi and S. Y. Liau, *Chem. Mater.*, 2010, **22**, 922-927.

41. T. Lopez-Luke, A. Wolcott, L. P. Xu, S. W. Chen, Z. H. Wcn, J. H. Li, E. De La Rosa and J. Z. Zhang, *J. Phys. Chem. C*, 2008, **112**, 1282-1292.

42. T. W. Kim, S. G. Hur, S. J. Hwang, H. Park, W. Choi and J. H. Choy, *Adv. Funct. Mater.*, 2007, **17**, 307-314.

43. X. Z. Li, F. B. Li, C. L. Yang and W. K. Ge, *J. Photochem. Photobiol. A-Chem.*, 2001, **141**, 209-217.

44. Y. T. Kwon, K. Y. Song, W. I. Lee, G. J. Choi and Y. R. Do, *J. Catal.*, 2000, **191**, 192-199.

45. J. H. Pan and W. I. Lee, *Chem. Mater.*, 2006, **18**, 847-853.

46. D. Hou, X. Hu, P. Hu, W. Zhang, M. Zhang and Y. Huang, *Nanoscale*, 2013, **5**, 9764-9772.

47. L. Yang, S. Luo, Y. Li, Y. Xiao, Q. Kang and Q. Cai, *Environ. Sci. Technol.*, 2010, **44**, 7641-7646.

48. M. Long, W. M. Cai, J. Cai, B. X. Zhou, X. Y. Chai and Y. H. Wu, *J. Phys. Chem. B*, 2006, **110**, 20211-20216.

49. F. Meng, J. Li, S. K. Cushing, M. Zhi and N. Wu, *J. Am. Chem. Soc.*, 2013, **135**, 10286-10289.

50. R. M. Navarro, F. del Valle and J. L. G. Fierro, *Int. J. Hydrog. Energy*, 2008, **33**, 4265-4273.

51. J. Xing, J. F. Chen, Y. H. Li, W. T. Yuan, Y. Zhou, L. R. Zheng, H. F. Wang, P. Hu, Y. Wang, H. J. Zhao and H. G. Yang, *Chem. Eur. J.*, 2014, **20**, 2138-2144.

52. I. Tsuji, H. Kato and A. Kudo, *Angew. Chem., Int. Ed.*, 2005, **44**, 3565-3568.

53. M. Hara, J. Nunoshige, T. Takata, J. N. Kondo and K. Domen, *Chem. Commun.*, 2003, 3000-3001.

54. T. Sreethawong and S. Yoshikawa, *Catal. Commun.*, 2005, **6**, 661-668.

55. T. Sano, S. Kutsuna, N. Negishi and K. Takeuchi, *J. Mol. Catal. A: Chem.*, 2002, **189**, 263-270.

56. S. Jin and F. Shiraishi, *Chem. Eng. J.*, 2004, **97**, 203-211.

57. D. N. Ke, T. Y. Peng, L. Ma, P. Cai and P. Jiang, *Appl. Catal., A*, 2008, **350**, 111-117.

58. R. Georgekutty, M. K. Seery and S. C. Pillai, *J. Phys. Chem. C*, 2008, **112**, 13563-13570.

59. W. W. Lu, S. Y. Gao and J. J. Wang, *J. Phys. Chem. C*, 2008, **112**, 16792-16800.

60. B. Pal, S. Ikeda, H. Kominami, Y. Kera and B. Ohtani, *J. Catal.*, 2003, **217**, 152-159.

61. Y. Sasaki, A. Iwase, H. Kato and A. Kudo, *J. Catal.*, 2008, **259**, 133-137.

62. Q. J. Xiang, J. G. Yu and M. Jaroniec, *J. Am. Chem. Soc.*, 2012, **134**, 6575-6578.

63. W. J. Zhou, Z. Y. Yin, Y. P. Du, X. Huang, Z. Y. Zeng, Z. X. Fan, H. Liu, J. Y. Wang and H. Zhang, *Small*, 2013, **9**, 140-147.

64. F. A. Frame and F. E. Osterloh, *J. Phys. Chem. C*, 2010, **114**, 10628-10633.

65. L. Ge, C. C. Han, X. L. Xiao and L. L. Guo, *Int. J. Hydrog. Energy*, 2013, **38**, 6960-6969.

66. L. Zhang, B. Z. Tian, F. Chen and J. L. Zhang, *Int. J. Hydrog. Energy*, 2012, **37**, 17060-17067.

67. J. D. Hong, Y. S. Wang, Y. B. Wang, W. Zhang and R. Xu, *ChemSusChem*, 2013, **6**, 2263-2268.

68. H. J. Yan, J. H. Yang, G. J. Ma, G. P. Wu, X. Zong, Z. B. Lei, J. Y. Shi and C. Li, *J. Catal.*, 2009, **266**, 165-168.

69. S. H. Shen, L. J. Guo, X. B. Chen, F. Ren and S. S. Mao, *Int. J. Hydrog. Energy*, 2010, **35**, 7110-7115.

70. X. Zong, J. F. Han, G. J. Ma, H. J. Yan, G. P. Wu and C. Li, *J. Phys. Chem. C*, 2011, **115**, 12202-12208.

71. J. S. Jang, D. J. Ham, N. Lakshminarasimhan, W. Y. Choi and J. S. Lee, *Appl. Catal., A*, 2008, **346**, 149-154.

72. A. T. Garcia- Esparza, D. Cha, Y. Ou, J. Kubota, K. Domen and K. Takanabe, *ChemSusChem*, 2013, **6**, 168-181.

73. A. Indra, P. W. Menezes, I. Zaharieva, E. Baktash, J. Pfrommer, M. Schwarze, H. Dau and M. Driess, *Angew. Chem., Int. Ed.*, 2013, **52**, 13206-13210.

74. B. Cao, G. M. Veith, J. C. Neuefeind, R. R. Adzic and P. G. Khalifah, *J. Am. Chem. Soc.*, 2013, **135**, 19186-19192.

75. K. S. Novoselov, A. K. Geim, S. V. Morozov, D. Jiang, Y. Zhang, S. V. Dubonos, I. V. Grigorieva and A. A. Firsov, *Science*, 2004, **306**, 666-669.

76. Q. J. Xiang, J. G. Yu and M. Jaroniec, *Chem. Soc. Rev.*, 2012, **41**, 782-796.

77. G. Williams, B. Seger and P. V. Kamat, *ACS nano*, 2008, **2**, 1487-1491.

78. H. Zhang, X. J. Lv, Y. M. Li, Y. Wang and J. H. Li, *ACS nano*, 2010, **4**, 380-386.

79. X. Y. Zhang, H. P. Li, X. L. Cui and Y. H. Lin, *J. Mater. Chem.*, 2010, **20**, 2801-2806.

80. Q. Li, B. D. Guo, J. G. Yu, J. R. Ran, B. H. Zhang, H. J. Yan and J. R. Gong, *J. Am. Chem. Soc.*, 2011, **133**, 10878-10884.

81. L. Jia, D. H. Wang, Y. X. Huang, A. W. Xu and H. Q. Yu, *J. Phys. Chem. C*, 2011, **115**, 11466-11473.

82. B. J. Li and H. Q. Cao, *J. Mater. Chem.*, 2011, **21**, 3346-3349.

83. T. G. Xu, L. W. Zhang, H. Y. Cheng and Y. F. Zhu, *Appl. Catal., B*, 2011, **101**, 382-387.

84. Q. J. Xiang, J. G. Yu and M. Jaroniec, *J. Phys. Chem. C*, 2011, **115**, 7355-7363.

85. G. Z. Liao, S. Chen, X. Quan, H. T. Yu and H. M. Zhao, *J. Mater. Chem.*, 2012, **22**, 2721-2726.

86. Y. H. Ng, A. Iwase, A. Kudo and R. Amal, *J. Phys. Chem. Lett.*, 2010, **1**, 2607-2612.

87. Y. S. Fu, X. Q. Sun and X. Wang, *Mater. Chem. Phys.*, 2011, **131**, 325-330.

88. J. L. Gunjakar, I. Y. Kim, J. M. Lee, Y. K. Jo and S. J. Hwang, *J. Phys. Chem. C*, 2014, **118**, 3847-3863.

89. H. Tong, S. Ouyang, Y. Bi, N. Umezawa, M. Oshikiri and J. Ye, *Adv. Mater.*, 2012, **24**, 229-251.

90. X. L. Hu, G. S. Li and J. C. Yu, *Langmuir*, 2010, **26**, 3031-3039.

91. F. E. Osterloh, *Chem. Soc. Rev.*, 2013, **42**, 2294-2320.

92. D. Beydoun, R. Amal, G. Low and S. McEvoy, *J. Nanopart. Res.*, 1999, **1**, 439-458.

93. X. Chen and S. S. Mao, *Chem. Rev.*, 2007, **107**, 2891-2959.

94. A. Chemseddine and T. Moritz, *Eur. J. Inorg. Chem.*, 1999, **1999**, 235-245.

95. X. Q. Gong and A. Selloni, *J. Phys. Chem. B*, 2005, **109**, 19560-19562.

96. H. G. Yang, C. H. Sun, S. Z. Qiao, J. Zou, G. Liu, S. C. Smith, H. M. Cheng and G. Q. Lu, *Nature*, 2008, **453**, 638-641.

97. X. G. Han, Q. Kuang, M. S. Jin, Z. X. Xie and L. S. Zheng, *J. Am. Chem. Soc.*, 2009, **131**, 3152-+.

98. S. Xie, X. Han, Q. Kuang, J. Fu, L. Zhang, Z. Xie and L. Zheng, *Chem. Commun.*, 2011, **47**, 6722-6724.

99. M. Murdoch, G. Waterhouse, M. Nadeem, J. Metson, M. Keane, R. Howe, J. Llorca and H. Idriss, *Nat. Chem.*, 2011, **3**, 489-492.

100. H. Yuzawa, T. Yoshida and H. Yoshida, *Appl. Catal. B*, 2012, **115–116**, 294-302.

101. C. u. Gomes Silva, R. Juárez, T. Marino, R. Molinari and H. García, *J. Am. Chem. Soc.*, 2010, **133**, 595-602.

102. H. Wang, T. T. You, W. W. Shi, J. H. Li and L. Guo, *J. Phys. Chem. C*, 2012, **116**, 6490-6494.

103. S. Linic, P. Christopher and D. B. Ingram, *Nat. Mater.*, 2011, **10**, 911-921.

104. K. L. Kelly, E. Coronado, L. L. Zhao and G. C. Schatz, *J. Phys. Chem. B*, 2003, **107**, 668-677.

105. Y. Xia and N. J. Halas, *MRS Bull.*, 2005, **30**, 338-348.

106. N. Halas, *MRS Bull.*, 2005, **30**, 362-367.

107. C. J. Orendorff, T. K. Sau and C. J. Murphy, *Small*, 2006, **2**, 636-639.

108. P. J. Chung, L. M. Lyu and M. H. Huang, *Chem. Eur. J.*, 2011, **17**, 9746-9752.

109. M. L. Personick, M. R. Langille, J. Zhang and C. A. Mirkin, *Nano Lett.*, 2011, **11**, 3394-3398.

110. E. Kowalska, O. O. P. Mahaney, R. Abe and B. Ohtani, *Phys. Chem. Chem. Phys.*, 2010, **12**, 2344-2355.

111. N. Sakai, Y. Fujiwara, Y. Takahashi and T. Tatsuma, *ChemPhysChem*, 2009, **10**, 766-769.

112. Y. Tian and T. Tatsuma, *J. Am. Chem. Soc.*, 2005, **127**, 7632-7637.

113. T. Y. Zhai, X. S. Fang, L. Li, Y. Bando and D. Golberg, *Nanoscale*, 2010, **2**, 168-187.

114. P. M. Rorvik, T. Grande and M. A. Einarsrud, *Adv. Mater.*, 2011, **23**, 4007-4034.

115. Y. Li, X. Y. Yang, Y. Feng, Z. Y. Yuan and B. L. Su, *Crit. Rev. Solid State Mat. Sci.*, 2012, **37**, 1-74.

116. A. I. Hochbaum and P. D. Yang, *Chem. Rev.*, 2010, **110**, 527-546.

117. Q. P. Ding, Y. P. Yuan, X. Xiong, R. P. Li, H. B. Huang, Z. S. Li, T. Yu, Z. G. Zou and S. G. Yang, *J. Phys. Chem. C*, 2008, **112**, 18846-18848.

118. X. Yi and J. L. Li, *J. Sol-Gel Sci. Technol.*, 2010, **53**, 480-484.

119. F. Gao, Y. Yuan, K. F. Wang, X. Y. Chen, F. Chen and J. M. Liu, *Appl. Phys. Lett.*, 2006, **89**.

120. M. Miyauchi, *J. Phys. Chem. C*, 2007, **111**, 12440-12445.

121. J. S. Jang, U. A. Joshi and J. S. Lee, *J. Phys. Chem. C*, 2007, **111**, 13280-13287.

122. Y. X. Li, Y. F. Hu, S. Q. Peng, G. X. Lu and S. B. Li, *J. Phys. Chem. C*, 2009, **113**, 9352-9358.

123. S. Q. Liu, N. Zhang, Z. R. Tang and Y. J. Xu, *ACS Appl. Mater. Interfaces*, 2012, **4**, 6378-6385.

124. L. Wang, H. W. Wei, Y. J. Fan, X. Gu and J. H. Zhan, *J. Phys. Chem. C*, 2009, **113**, 14119-14125.

125. S. L. Xiong, B. J. Xi and Y. T. Qian, *J. Phys. Chem. C*, 2010, **114**, 14029-14035.

126. F. Zhang and S. S. Wong, *Chem. Mater.*, 2009, **21**, 4541-4554.

127. J. S. Jang, H. G. Kim, U. A. Joshi, J. W. Jang and J. S. Lee, *Int. J. Hydrog. Energy*, 2008, **33**, 5975-5980.

128. Z. Y. Yuan and B. L. Su, *Colloid Surf. A-Physicochem. Eng. Asp.*, 2004, **241**, 173-183.

129. G. M. Wang, H. Y. Wang, Y. C. Ling, Y. C. Tang, X. Y. Yang, R. C. Fitzmorris, C. C. Wang, J. Z. Zhang and Y. Li, *Nano Lett.*, 2011, **11**, 3026-3033.

130. T. J. Kuo, C. N. Lin, C. L. Kuo and M. H. Huang, *Chem. Mater.*, 2007, **19**, 5143-5147.

131. T. J. Sun, J. S. Qiu and C. H. Liang, *J. Phys. Chem. C*, 2008, **112**, 715-721.

132. J. Lv, T. Kako, Z. S. Li, Z. G. Zou and J. H. Ye, *J. Phys. Chem. C*, 2010, **114**, 6157-6162.

133. G. F. Walker, *Nature*, 1960, **187**, 312-313.

134. A. J. Jacobson, in *Soft Chemistry Routes to New Materials - Chimie Douce*, eds. J. Rouxel, M. Tournoux and R. Brec, 1994, vol. 152-, pp. 1-12.

135. R. Z. Ma and T. Sasaki, *Adv. Mater.*, 2010, **22**, 5082-5104.

136. M. W. Takayoshi Sasaki, Hideo Hashizume, Hirohisa Yamada, and Hiromoto Nakazawa, *J. Am. Chem. Soc.*, 1996, **118**, 8329–8335.

137. M. Osada and T. Sasaki, *Adv. Mater.*, 2012, **24**, 210-228.

138. M. Osada and T. Sasaki, *J. Mater. Chem.*, 2009, **19**, 2503-2511.

139. J. N. Coleman, M. Lotya, A. O'Neill, S. D. Bergin, P. J. King, U. Khan, K. Young, A. Gaucher, S. De, R. J. Smith, I. V. Shvets, S. K. Arora, G. Stanton, H. Y. Kim, K. Lee, G. T. Kim, G. S. Duesberg, T. Hallam, J. J. Boland, J. J. Wang, J. F. Donegan, J. C. Grunlan, G. Moriarty, A. Shmeliov, R. J. Nicholls, J. M. Perkins, E. M. Grieveson, K. Theuwissen, D. W. McComb, P. D. Nellist and V. Nicolosi, *Science*, 2011, **331**, 568-571.

140. M. Osada and T. Sasaki, *Adv. Mater.*, 2011, **24**, 210-228.

141. E. M. Sabio, M. F. Chi, N. D. Browning and F. E. Osterloh, *Langmuir*, 2010, **26**, 7254-7261.

142. Y. Matsumoto, S. Ida and T. Inoue, *J. Phys. Chem. C*, 2008, **112**, 11614-11616.

143. Y. Miseki, H. Kato and A. Kudo, *Energy Environ. Sci.*, 2009, **2**, 306-314.

144. T. Takata, Y. Furumi, K. Shinohara, A. Tanaka, M. Hara, J. N. Kondo and K. Domen, *Chem. Mater.*, 1997, **9**, 1063-1064.

145. K. Domen, J. Yoshimura, T. Sekine, A. Tanaka and T. Onishi, *Catal. Lett.*, 1990, **4**, 339-343.

146. G. Liu, L. Wang, C. Sun, X. Yan, X. Wang, Z. Chen, S. C. Smith, H. M. Cheng and G. Q. Lu, *Chem. Mater.*, 2009, **21**, 1266-1274.

147. A. Mukherji, C. Sun, S. C. Smith, G. Q. Lu and L. Wang, *J. Phys. Chem. C*, 2011, **115**, 15674-15678.

148. A. Mukherji, B. Seger, G. Q. Lu and L. Wang, *ACS nano*, 2011, **5**, 3483-3492.

149. X. Zong, C. Sun, Z. Chen, A. Mukherji, H. Wu, J. Zou, S. C. Smith, G. Q. Lu and L. Wang, *Chem. Commun.*, 2011, **47**, 6293-6295.

150. J. L. Gunjakar, I. Y. Kim, J. M. Lee, Y. K. Jo and S. J. Hwang, *J. Phys. Chem. C*, 2014, **118**, 3847-3863.

151. D. W. Hwang, H. G. Kim, J. Kim, K. Y. Cha, Y. G. Kim and J. S. Lee, *J. Catal.*, 2000, **193**, 40-48.

152. K. Sayama, A. Tanaka, K. Domen, K. Maruya and T. Onishi, *J. Catal.*, 1990, **124**, 541-547.

153. K. Domen, A. Kudo, M. Shibata, A. Tanaka, K. Maruya and T. Onishi, *J. Chem. Soc., Chem. Commun.* , 1986, 1706-1707.

154. K. Domen, A. Kudo, A. Shinozaki, A. Tanaka, K. Maruya and T. Onishi, *J. Chem. Soc., Chem. Commun.* , 1986, 356-357.

155. M. Dion, M. Ganne and M. Tournoux, *Mater. Res. Bull.*, 1981, **16**, 1429-1435.

156. H. Fukuoka, T. Isami and S. Yamanaka, *J. Solid State Chem.*, 2000, **151**, 40-45.

157. H. G. Kim, D. W. Hwang and J. S. Lee, *J. Am. Chem. Soc.*, 2004, **126**, 8912-8913.

158. X. Du and I. Chen, *J. Am. Ceram. Soc.*, 1998, **81**, 3253-3259.

159. A. Ishikawa, T. Takata, T. Matsumura, J. N. Kondo, M. Hara, H. Kobayashi and K. Domen, *J. Phys. Chem. B*, 2004, **108**, 2637-2642.

160. A. Ishikawa, T. Takata, J. N. Kondo, M. Hara, H. Kobayashi and K. Domen, *J. Am. Chem. Soc.*, 2002, **124**, 13547-13553.

161. C. Thaminimulla, T. Takata, M. Hara, J. Kondo and K. Domen, *J. Catal.*, 2000, **196**, 362-365.

162. R. Konta, T. Ishii, H. Kato and A. Kudo, *J. Phys. Chem. B*, 2004, **108**, 8992-8995.

163. R. Niishiro, H. Kato and A. Kudo, *Phys. Chem. Chem. Phys.*, 2005, **7**, 2241-2245.

164. H. Kato and A. Kudo, *J. Phys. Chem. B*, 2002, **106**, 5029-5034.

165. X. Wang, K. Maeda, A. Thomas, K. Takanabe, G. Xin, J. M. Carlsson, K. Domen and M. Antonietti, *Nat. Mater.*, 2009, **8**, 76-80.

166. Y. Wang, X. Wang and M. Antonietti, *Angew. Chem., Int. Ed.*, 2012, **51**, 68-89.

167. D. S. Su, J. Zhang, B. Frank, A. Thomas, X. C. Wang, J. Paraknowitsch and R. Schlogl, *ChemSusChem*, 2010, **3**, 169-180.

168. Y. Cui, Z. Ding, X. Fu and X. Wang, *Angew. Chem., Int. Ed.*, 2012, **51**, 11814-11818.

169. X. Wang, S. Blechert and M. Antonietti, *ACS Catal.*, 2012, **2**, 1596-1606.

170. P. Niu, L. L. Zhang, G. Liu and H. M. Cheng, *Adv. Funct. Mater.*, 2012, **22**, 4763-4770.

171. S. Yang, Y. Gong, J. Zhang, L. Zhan, L. Ma, Z. Fang, R. Vajtai, X. Wang and P. M. Ajayan, *Adv. Mater.*, 2013, **25**, 2452-2456.

172. G. Liu, P. Niu, C. Sun, S. C. Smith, Z. Chen, G. Q. Lu and H. M. Cheng, *J. Am. Chem. Soc.*, 2010, **132**, 11642-11648.

173. Y. Zhang, T. Mori, J. Ye and M. Antonietti, *J. Am. Chem. Soc.*, 2010, **132**, 6294-6295.

174. Y. Wang, Y. Di, M. Antonietti, H. R. Li, X. F. Chen and X. C. Wang, *Chem. Mat.*, 2010, **22**, 5119-5121.

175. P. Niu, G. Liu and H. M. Cheng, *J. Phys. Chem. C*, 2012, **116**, 11013-11018.

176. L. Ge, C. Han and J. Liu, *Appl. Catal., A,* 2011, **108**, 100-107.

177. C. Pan, J. Xu, Y. Wang, D. Li and Y. Zhu, *Adv. Funct. Mater.*, 2012, **22**, 1518-1524.

178. Y. Wang, R. Shi, J. Lin and Y. Zhu, *Energy Environ. Sci.*, 2011, **4**, 2922-2929.

179. H. Yan and Y. Huang, *Chem. Commun.*, 2011, **47**, 4168-4170.

180. Y. Sui, J. Liu, Y. Zhang, X. Tian and W. Chen, *Nanoscale*, 2013, **5**, 9150-9155.

181. Y. L. Meng, J. Shen, D. Chen and G. Xin, *Rare Metals*, 2011, **30**, 276-279.

182. N. Cheng, J. Tian, Q. Liu, C. Ge, A. H. Qusti, A. M. Asiri, A. O. Al-Youbi and X. Sun, *ACS Appl. Mater. Interfaces*, 2013, **5**, 6815-6819.

183. Z. Liu, K. Ooi, H. Kanoh, W. Tang and T. Tomida, *Langmuir*, 2000, **16**, 4154-4164.

184. G. B. Saupe, C. C. Waraksa, H. N. Kim, Y. J. Han, D. M. Kaschak, D. M. Skinner and T. E. Mallouk, *Chem. Mater.*, 2000, **12**, 1556-1562.

185. D. S. Kim, T. C. Ozawa, K. Fukuda, S. Ohshima, I. Nakai and T. Sasaki, *Chem. Mater.*, 2011, **23**, 2700-2702.

186. H. Sato, K. Ono, T. Sasaki and A. Yamagishi, *J. Phys. Chem. B*, 2003, **107**, 9824-9828.

187. T. Tanaka, Y. Ebina, K. Takada, K. Kurashima and T. Sasaki, *Chem. Mater.*, 2003, **15**, 3564-3568.

188. T. Sasaki, M. Watanabe, H. Hashizume, H. Yamada and H. Nakazawa, *J. Am. Chem. Soc.*, 1996, **118**, 8329-8335.

189. T. Sasaki and M. Watanabe, *J. Am. Chem. Soc.*, 1998, **120**, 4682-4689.

190. M. Gateshki, S. J. Hwang, D. H. Park, Y. Ren and V. Petkov, *Chem. Mater.*, 2004, **16**, 5153-5157.

191. K. Fukuda, Y. Ebina, T. Shibata, T. Aizawa, I. Nakai and T. Sasaki, *J. Am. Chem. Soc.*, 2007, **129**, 202-209.

192. N. Sakai, Y. Ebina, K. Takada and T. Sasaki, *J. Am. Chem. Soc.*, 2004, **126**, 5851-5858.

193. T. Sasaki, Y. Ebina, Y. Kitami, M. Watanabe and T. Oikawa, *J. Phys. Chem. B*, 2001, **105**, 6116-6121.

194. T. Sasaki and M. Watanabe, *J. Phys. Chem. B*, 1997, **101**, 10159-10161.

195. G. Liu, L. Wang, C. Sun, Z. Chen, X. Yan, L. Cheng, H. M. Cheng and G. Q. M. Lu, *Chem. Commun.*, 2009, 1383-1385.

196. X. Dong, J. Fu and F. Xi, *J. Mater. Res.*, 2011, **26**, 1285-1291.

197. M. Sadhukhan and S. Barman, *J. Mater. Chem. A*, 2013, **1**, 2752-2756.

198. X. Zhang, X. Xie, H. Wang, J. Zhang, B. Pan and Y. Xie, *J. Am. Chem. Soc.*, 2012, **135**, 18-21.

199. H. X. Zhao, H. T. Yu, X. Quan, S. Chen, H. M. Zhao and H. Wang, *RSC Adv.*, 2014, **4**, 624-628.

200. X. She, H. Xu, Y. Xu, J. Yan, J. Xia, L. Xu, Y. Song, Y. Jiang, Q. Zhang and H. Li, *J. Mater. Chem. A*, 2014, **2**, 2563-2570.

201. J. Xu, L. Zhang, R. Shi and Y. Zhu, *J. Mater. Chem. A*, 2013, **1**, 14766-14772.

202. X. Huang, C. Tan, Z. Yin and H. Zhang, *Adv. Mater.*, 2014, **26**, 2185-2204.

203. G. C. Xie, K. Zhang, B. D. Guo, Q. Liu, L. Fang and J. R. Gong, *Adv. Mater.*, 2013, **25**, 3820-3839.

204. K. Maeda, M. Eguchi, W. J. Youngblood and T. E. Mallouk, *Chem. Mater.*, 2008, **20**, 6770-6778.

205. K. Maeda, M. Eguchi, S. H. A. Lee, W. J. Youngblood, H. Hata and T. E. Mallouk, *J. Phys. Chem. C*, 2009, **113**, 7962-7969.

206. J. Kim, S. Byun, A. J. Smith, J. Yu and J. X. Huang, *J. Phys. Chem. Lett.*, 2013, **4**, 1227-1232.

207. H. Hata, S. Kubo, Y. Kobayashi and T. E. Mallouk, *J. Am. Chem. Soc.*, 2007, **129**, 3064-3065.

208. S. M. Paek, H. Jung, M. Park, J. K. Lee and J. H. Choy, *Chem. Mater.*, 2005, **17**, 3492-3498.

209. S. M. Paek, H. Jung, Y. J. Lee, M. Park, S. J. Hwang and J. H. Choy, *Chem. Mater.*, 2006, **18**, 1134-1140.

210. H. C. Lee, H. Jung, J. M. Oh and J. H. Choy, *Bull. Korean Chem. Soc.*, 2002, **23**, 477-480.

211. T. W. Kim, H. W. Ha, M. J. Paek, S. H. Hyun, I. H. Baek, J. H. Choy and S. J. Hwang, *J. Phys. Chem. C*, 2008, **112**, 14853-14862.

212. H. Jung, H. C. Lee, S. M. Paek, S. J. Hwang and J. H. Choy, *J. Phys. Chem. Solids*, 2006, **67**, 2435-2435.

213. H. W. Ha, T. W. Kim, J. H. Choy and S. J. Hwang, *J. Phys. Chem. C*, 2009, **113**, 21941-21948.

214. J. H. Choy, H. C. Lee, H. Jung, H. Kim and H. Boo, *Chem. Mater.*, 2002, **14**, 2486-2491.

215. J. H. Choy, H. C. Lee, H. Jung and S. J. Hwang, *J. Mater. Chem.*, 2001, **11**, 2232-2234.

216. J. H. Choy, *J. Phys. Chem. Solids*, 2004, **65**, 373-383.

217. T. W. Kim, S. J. Hwang, S. H. Jhung, J. S. Chang, H. Park, W. Choi and J. H. Choy, *Adv. Mater.*, 2008, **20**, 539-542.

218. T. W. Kim, S. J. Hwang, Y. Park, W. Choi and J. H. Choy, *J. Phys. Chem. C*, 2007, **111**, 1658-1664.

219. T. W. Kim, H. W. Ha, M. J. Paek, S. H. Hyun, J. H. Choy and S. J. Hwang, *J. Mater. Chem.*, 2010, **20**, 3238-3245.

220. H. Jung, H. C. Lee, S. M. Paek, S. J. Hwang and J. H. Choy, *J. Phys. Chem. Solids*, 2006, **67**, 1248-1251.

221. T. W. Kim, A. R. Han, S. J. Hwang and J. H. Choy, *J. Phys. Chem. C*, 2007, **111**, 16774-16780.

222. I. Y. Kim, J. M. Lee, T. W. Kim, H. N. Kim, H. I. Kim, W. Choi and S. J. Hwang, *Small*, 2012, **8**, 1038-1048.

223. J. L. Gunjakar, T. W. Kim, H. N. Kim, I. Y. Kim and S. J. Hwang, *J. Am. Chem. Soc.*, 2011, **133**, 14998-15007.

224. B. Seger, J. McCray, A. Mukherji, X. Zong, Z. Xing and L. Wang, *Angew. Chem., Int. Ed.*, 2013, **52**, 6400-6403.

225. N. Sakai, K. Fukuda, Y. Omomo, Y. Ebina, K. Takada and T. Sasaki, *J. Phys. Chem. C*, 2008, **112**, 5197-5202.

226. Y. Zhou, R. Ma, Y. Ebina, K. Takada and T. Sasaki, *Chem. Mater.*, 2006, **18**, 1235-1239.

227. L. Wang, Y. Ebina, K. Takada and T. Sasaki, *J. Phys. Chem. B*, 2004, **108**, 4283-4288.

228. Z. S. Wang, Y. Ebina, K. Takada, M. Watanabe and T. Sasaki, *Langmuir*, 2003, **19**, 9534-9537.

3. Research methodology

3.1 Materials synthesis

3.1.1 Synthesis of exfoliated titania NSs

Titania NSs suspension ($Ti_{0.91}O_2$ NSs) was prepared according to previous reports by Sasaki's group.[1-4] In a typical synthesis process, the layered $Cs_{0.68}Ti_{1.83}O_4$ precursor was first obtained by solid state reaction, followed by proton-exchange to $H_{0.68}Ti_{1.83}O_4 \cdot H_2O$ in hydrochloric acid and a delamination step in the presence of tetrabutylammonium cations (TBA^+). Stoichiometric mixture of Cs_2CO_3 and TiO_2 were thoroughly ground before heated at 1033 K for 30 min. Then the sample was reground and reheated at 1033 K for another 12 h. The obtained $Cs_{0.68}Ti_{1.83}O_4$ titanate precursor was subsequently placed in excess amount of hydrochloric acid (1 M) and stirred vigorously for three days. The hydrochloric acid was refreshed every 24 h and the proton-exchanged titanate $H_{0.68}Ti_{1.83}O_4 \cdot H_2O$ can be collected by centrifugation and wash with deionised water. The dried $H_{0.68}Ti_{1.83}O_4 \cdot H_2O$ was re-dispersed in tetrabutylammonium hydroxide (TBAOH) solution containing same amount of TBA+ as protons, and the white suspension was shaken for over 7 days. To remove the un-delaminated precursors, the suspension was centrifuged under 4700 rpm and the supernatant suspension was collected for use. The concentration of $Ti_{0.91}O_2$ NSs suspension is ca. 1.79 g/L.

3.1.2 Synthesis of octahedral gold nanoparticles

Octahedral Au nanoparticles (NPs) were synthesized via a simple hydrothermal method reported before.[5] 0.055 g of cetyltrimethylammonium bromide (CTAB) was first dissolved in 9.7 mL of deionised water, and then 250 μL of 0.01 M $HAuCl_4$ and 50 μL of 0.1 M trisodium citrate were added. The solution was then transferred to a Teflon-lined autoclave and heated at 383 K in an oven for 48 h. The concentration of Au NPs suspension is ca. 0.05 g/L.

3.1.3 Synthesis of CdTe@CdS nanocrystals

The CdTe@CdS NCs were prepared via a simple one-pot hydrothermal reaction.[6] Typically, $CdCl_2$ (51.52 mg), tri-sodium citrate dehydrate (560 mg) and mercaptosuccinic acid (MSA) (141.4 mg) were dissolved in 66 mL of deionized water in 3-neck flask. The solution was bubbled with N_2 gas for some time. Then 2 mL of Na_2TeO_3 solution (0.014 M) was added to the flask rapidly under vigorous stirring and N_2 gas bubbling. After 5 min, 2 mL freshly prepared $NaBH_4$ solution (0.93 M) was quickly added to the flask. When color of the solution became golden, it was transferred to a Teflon-lined autoclave and heated in oven at 453 K for 50 min. In the synthesis process, the amount of Cd^{2+} is excessive so the concentration of the CdTe core is determined to be 0.096 g/L based on the concentration of Te source.

3.1.4 Synthesis of nanohybrid of titania NSs and gold nanoparticles

Under vigorous stirring, 2 mL of Au NPs suspension was added dropwise to 50 mL of $Ti_{0.91}O_2$ NSs suspension. After 30 min of stirring to reach a uniform mixture of NPs and NSs, hydrochloric acid (1 M) were added to flocculate the NSs coupled with NPs. The nanohybrids were centrifuged, washed with deionised water and ethanol for several times and dried in a 373 K oven. The as-prepared sample is denoted as O-Au-NS. Then O-Au-NS was placed in an alumina crucible and calcined at 723 K for 2 h, which is denoted as O-Au-A. The ratio of Au in both O-Au-NS and O-Au-A is calculated to be around 0.11 wt%.

As comparison, two types of nanohybrids between $Ti_{0.91}O_2$ NSs and irregular Au NPs were prepared, in which the ratio of Au was kept to be 0.11 wt%. One sample was prepared by direct deposition of Au particles onto $Ti_{0.91}O_2$ NSs via photo-deposition, flocculation with protons and calcination. First, 2 mL of $HAuCl_4$ solution (0.01 M) and ethanol were added to 50 mL of $Ti_{0.91}O_2$ NSs suspension. Under stirring, the suspension was illuminated by Xenon lamp for 6 h, and flocculated with hydrochloric acid (1 M). To ensure that $HAuCl_4$

has been completely reduced to Au, the supernatant solution after centrifugation was treated with $NaBH_4$ solution and its absorption spectrum was measured by a UV-Vis spectrometer. The flocculated product was then calcined at 723 K and this sample was denoted as Au-A-1.

The other sample was prepared by photo-depositing gold onto restacked NSs after calcination. 50 mL of $Ti_{0.91}O_2$ NSs suspension was first flocculated with hydrochloric acid (1 M), followed by calcination 723 K for 2 h. The obtained product (A) was then dispersed in ethanol solution containing 2 mL of $HAuCl_4$ (0.01 M), and illuminated by Xenon lamp for 6 h. Similar method was implemented to ensure the complete reduction of $HAuCl_4$ as used in the preparation of Au-A-1. This sample was denoted as Au-A-2.

3.1.5 Synthesis of nanocomposite of CdTe@CdS nanocrystals and titania NSs

CdTe@CdS NCs suspension was first washed in order to remove excessive organic chemicals and other ions. CdTe@CdS NCs suspension was mixed with equal volume of ethanol, and centrifuged at 4500 rpm for 10 min. After centrifugation, the supernatant solution was removed and the deposits were redispersed in deionized water to keep the same concentration. Under vigorous stirring, 10 mL of CdTe@CdS NCs suspension was added to 25 mL of titania NSs suspension. CdTe@CdS NCs and titania NSs were allowed to fully mix for 30 min, and 5 ml of PEI solution (0.125 wt%)was then added. After stirring for another 1 h, the suspension was centrifuged at 4700 rpm and washed for several times. The nanohybrid was finally dried at 313 K in a vacuum oven, and ca. 45 mg of final product was obtained. In this nanohybrid, the ratio of CdTe is calculated to be 2.1 wt% based on the concentrations of $Ti_{0.91}O_2$ NSs and CdTe core.

3.1.6 Synthesis of graphitic carbon nitride (g-C_3N_4)

The g-C_3N_4 powders are prepared via polycondensation of dicyandiamide according a reported method.[7] In a typical synthesis, dicyandiamide powder was placed in an alumina crucible, covered with cap and heated at 823 K for 4 h in a muffle furnace with a ramp rate of 2.3 K/min and in the cooling process the ramp rate was maintained at 1 K/min. The obtained yellow agglomerates were ground to fine powders in an agate mortar for later use.

3.1.7 Synthesis of C_3N_4-PEDOT composites

To prepare the C_3N_4-PEDOT composites, the g-C_3N_4 powders were mixed with commercial PEDOT:PSS "solution" containing 0.5 wt%, 1 wt%, 2 wt% and 5 wt% of PEDOT:PSS respectively. The suspension was then evaporated under vigorous stirring via heating. To make the PEDOT insoluble, the dried powders were subsequently soaked in ethylene glycol (EG) and stirred for 1 h. After treatment with EG, the C_3N_4-PEDOT composites were centrifuged, washed with deionized water and ethanol for several times and dried in a 373 K oven. The final products were ground again after being dried, and different composites were denoted as C_3N_4-0.5%PEDOT, C_3N_4-1%PEDOT, C_3N_4-2%PEDOT and C_3N_4-5%PEDOT, respectively.

3.1.8 Synthesis of phosphorus-doped C_3N_4 NSs

To prepare the phosphorus-doped g-C_3N_4, 0.5 g of sodium hypophosphite monohydrate ($NaH_2PO_2 \cdot H_2O$) and 0.5 g of g-C_3N_4 were thoroughly ground together before being transferred to a quartz boat. The mixture was then placed in a tube furnace and heated at 773 K for 1 h under N_2 gas flow. The as-prepared phosphorus-doped g-C_3N_4 powder was then washed via dialysis.

The phosphorus-doped g-C_3N_4 was then dispersed in water and sonicated with an ultra-sonication probe (300 W, 40 kHz) for 1 h. After exfoliation, the nanosheets (NSs) suspension was centrifuged at 4700 rpm to remove unexfoliated precursors. The concentration was determined to be 2.4 g/L. The NSs suspension is very stable and no visible precipitates can be found within 6 months.

As a comparison, g-C_3N_4 was also dispersed in water and sonicated with ultra-sonication probe for 1h. However, the sonicated g-C_3N_4 suspension fully precipitated in 2 weeks, leaving the supernatant solution clear. So the sonication time was extended from 1 h to 8 h, but same phenomenon was observed.

3.1.9 Layer-by-layer assembly with phosphorus-doped C_3N_4 NSs

Both quartz and fluorine doped tin oxide (FTO) glass substrates were cleaned by being sonicated in diluted HCl solution, acetone, ethanol and deionized water for 10 min each. The clean substrates were stored in deionlised water before use.

Layer-by-layer assembly of poly(diallyldimethylammonium chloride) (PDDA) and P-doped g-C_3N_4 NSs was conducted on quartz substrate. The substrate was immersed in an

aqueous PDDA solution (20 g/L) for 10 min and diluted NSs suspension (100 mg/L) for 4 min for each layer. After the deposition of each layer, the substrate was rinsed with copious deionized water and dried with N_2 gas.

Layer-by-layer assembly of PEI and P-doped g-C_3N_4 NSs was conducted on FTO glass substrate. The substrate was immersed in an aqueous PEI solution (2.5 g/L) for 20 min and diluted NSs suspension (100 mg/L) for 20 min for each layer. After the deposition of each layer, the substrate was rinsed with copious deionized water and dried with N_2 gas.

3.2 Materials characterisations

The absorption spectra were measured using a Shimadzu 2200 UV-Vis spectrometer. The X-ray diffraction (XRD) measurements were conducted on a Rigaku Miniflex XRD instrument with Co Kα (λ=1.78897 Å) radiation. Photoluminescence (PL) measurements were performed with an Edinburgh Instruments FLS 920 Fluorescence spectrometer. Zeta potential was recorded on a Malvern Instruments Nano ZS Zetasizer. The transmission electron microscopy (TEM) images were taken using a JEOL JEM 1010. The high resolution TEM (HRTEM) images were taken using a JEOL JEM 2100. The X-ray photoelectron spectroscopy (XPS) measurements were conducted on a Thermo Escalab 250 spectrometer with monochromatic Al KR x-ray source. Atomic force microscope (AFM) measurements were performed with Asylum MFP-3D stand alone AFM.

3.3 Photocatalytic water splitting

The photocatalytic hydrogen reactions were carried out in a quartz reactor connected to a closed-gas circulation and evacuation system. In a typical test, certain amount of catalyst was suspended in 300 mL aqueous solution containing sacrificial agent. 1 wt% of Pt was added as co-catalyst. The reactor was thoroughly evacuated before the photocatalytic reaction, and then irradiated by a 300 W Xe lamp (Beijing Trusttech Co. Ltd., PLS-SXE-300UV) equipped with an optical cut-off filter (λ>420 nm or λ>400 nm) to remove UV light. A water filter was applied to eliminate infrared light. A cooling water cycle system was used to keep the temperature at 293±5 K. The produced H_2 gas was detected by gas chromatography (GC) with Ar as the carrier gas.

3.4 Photoelectrochemical tests

The photoelectrochemical tests were conducted in a quartz cell in a three-electrode setup using a CH instruments 660D electrochemical workstation. Pt foil was used as the counter electrode and an Ag/AgCl electrode was used as the reference electrode. The electrolyte was 0.5 M Na_2SO_4 solution and the visible light source was provided by a solar simulator (Newport Oriel 69907) equipped with an optical cut-off filter (λ > 400 nm).

3.5 References

1. T. Sasaki, M. Watanabe, H. Hashizume, H. Yamada and H. Nakazawa, *J. Am. Chem. Soc.*, 1996, **118**, 8329-8335.

2. T. Sasaki and M. Watanabe, *J. Am. Chem. Soc.*, 1998, **120**, 4682-4689.

3. T. Sasaki, Y. Ebina, Y. Kitami, M. Watanabe and T. Oikawa, *J. Phys. Chem. B*, 2001, **105**, 6116-6121.

4. T. Sasaki and M. Watanabe, *J. Phys. Chem. B*, 1997, **101**, 10159-10161.

5. C. C. Chang, H. L. Wu, C. H. Kuo and M. H. Huang, *Chem. Mater.*, 2008, **20**, 7570-7574.

6. Y. Zhu, Z. Li, M. Chen, H. M. Cooper, G. Q. Lu and Z. P. Xu, *J. Colloid Interface Sci.*, 2013, **390**, 3-10.

7. P. Niu, L. L. Zhang, G. Liu and H. M. Cheng, *Adv. Funct. Mater.*, 2012, **22**, 4763-4770.

4. Nanohybrid materials of titania nanosheets and plasmonic gold nanoparticles for effective hydrogen evolution

Nanohybrid materials of titania nanosheets and plasmonic gold nanoparticles for effective hydrogen evolution

Zheng Xing, Xu Zong, Teera Butburee, Jian Pan, Yang Bai, and Lianzhou Wang*

Submitted to ***Chemcatchem***

4.1 Abstract

A nanohybrid material containing exfoliated titania nanosheets and gold nanoparticles was prepared by the coupling between negatively charged $Ti_{0.91}O_2$ nanosheets and surfactant-capped Au nanoparticles, followed by flocculation and calcination. After hybridization with titania nanosheets, octahedral Au nanoparticles were embedded into the matrix of titania, which led to a broad absorption peak assigned to surface plasmon resonance (SPR) effect in the visible region. The obtained nanohybrid showed considerably improved photocatalytic hydrogen evolution performance compared to naked titania and conventional titania photo-deposited with Au due to the special SPR effect of the relatively large octahedral Au NPs. Through some comparison experiments, we demonstrated that the octahedral Au NPs mainly function as local light intensifier and photon scattering agent.

4.2 Introduction

Finding suitable semiconductors for artificial photosynthesis purpose is the key to solving many environmental and energy-related issues. One of the most important and promising artificial photosynthesis processes is hydrogen production from solar water splitting in the presence of semiconductor particulate catalyst, in which the clean hydrogen fuel with high energy capacity can be generated from water.[1, 2] Among various semiconductor photocatalysts, TiO_2 has been the most intensively investigated one because of its attractive features such as low cost, photo- and chemical- stability, and high synthesis controllability.[3, 4] However, TiO_2 has a relatively wide band gap (ca. 3.2 eV) and thus can only absorb UV light while it remains inactive in the visible region. To improve the photocatalytic activities of TiO_2 in visible region, guest species are often introduced via two different strategies: doping and heterostructuring. Doping is an effective way to incorporate guest atoms into the crystal lattice of TiO_2 and render visible light absorption. Nevertheless, doping often creates crystal defects, which may act as recombination centres for photoinduced electrons and holes.[5]

Unlike doping, heterostructuring allows the introduction of relatively bulky guest species by directly combining different materials with proper energy band alignment. A good example is the metal/semiconductor heterogeneous structure, in which noble metals such as Pt[6] and Au[7, 8] are often loaded onto semiconductors, and such a structure can provide effective charge separation and more active sites for water splitting. In addition, noble metal nanoparticles such as Ag, Au, Cu etc. have attracted much interest recently due to their unique surface plasmon resonance (SPR) properties.[4, 9, 10] SPR is defined as the collective oscillation of free electrons when the frequency of incident photons approaches the natural frequency of surface electron oscillation.[1] SPR effect can induce a very strong localized electric field near the noble metal nanostructures, and it can be significantly influenced by the size, shape and embedding medium.[11-15] Of those noble metals, Au draws particular attention as it has strong SPR effect in visible region and many researchers have successfully synthesized Au nanoparticles (NPs) with varied sizes and diverse morphologies.[15-17]

With the arising interest in the SPR study of Au, many semiconductor/Au composites have been investigated in terms of visible light activities and it was found that in many cases the enhancement of photocatalytic activities occurred at wavelengths corresponding to the metal SPR.[18-20] The enhancement induced by SPR has been contributed to three proposed mechanisms: direct charge injection from Au NPs to semiconductors, strong SPR-induced near-field electromagnetic energy and effective photon scattering.[11] In order to verify these mechanisms, titania-supported Au NPs have been prepared in various methods: direct adsorption of pre-synthesized Au colloids, photo-deposition, deposition-precipitation, core-shell structure construction, etc.[21] However, there are two great limitations of these methods. First, generally the size and morphologies of Au NPs cannot be precisely controlled owing to the absence of morphology-control reagents. In most cases, the Au NPs are of spherical shape. Second, Au NPs tend to aggregate or grow up at the surface of TiO_2 particles during the composite material synthesis process, which will lead to the variation of SPR properties. This issue can be solved by separating gold nanoparticles with titania, and thus forming a structure in which Au nanoparticles are embedded into titania, for example, core-shell structures.[22-25]

Although constructing core-shell structure provides an effective way to separate Au NPs, the coating process of tiania shell often involves careful and complex chemical and physical control.[26] Hata et al. reported a general method to intercalate Au NPs into galleries of layered materials such as Dion-Jacobson layered perovskite $HCa_2Nb_3O_{10}$ via

pre-intercalation of tetrabutylammonium hydroxide (TBAOH) and polyallylamine (PAA) to enlarge the interlayer space.[27] This general method promises a simpler method of embedding Au NPs into semiconductor matrix compared to the core-shell structure. Nevertheless, the size of gold is greatly restricted because the degree of gallery expansion is very limited. Here we report a facile way to prepare titania-gold nanohybrid materials with easily tunable Au NPs. By thorough mixing of exfoliated titania nanosheets (NSs) and pre-synthesized Au NPs followed by flocculation and calcination, most of the octahedral Au NPs can be incorporated into the matrix of anatase titania. The Au NPs can be simply controlled in terms of their shapes and sizes during the synthesis process, so particular SPR properties can be intentionally introduced into the hybrid material. We successfully synthesized an Au/TiO_2 composite material containing relatively large Au NPs. The Au NPs were well separated in the nanohybrid. Moreover, large octahedral Au NPs provide good SPR-induced optical properties such as localized light intensity enhancement and photon scattering improvement, and thus the as-prepared nanohybrid exhibited dramatically improved hydrogen evolution performance compared to the naked titania.

4.3 Results and Discussion

Formation and microstructure of the nanohybrid materials

The $Ti_{0.91}O_2$ NSs used in this work were obtained from exfoliation of a layered protonic titanate of lepidocrocite-type, $H_{0.68}Ti_{1.83}O_4 \cdot H_2O$ in aqueous solution of TBAOH.[28, 29] The prepared NSs possess a thickness of 0.75 nm taking the outer edge of surface oxygen atoms, and negative charges of ca. -39 mV.[30, 31] TEM image in Figure 4.1a confirms the ultrathin nature of $Ti_{0.91}O_2$ NSs and their extremely high two-dimensional anisotropy.

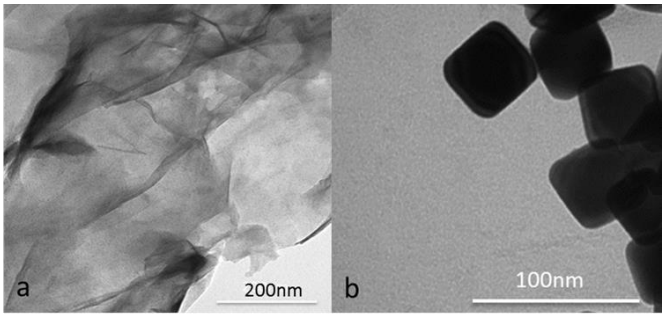

Figure 4.1 TEM images of (a) $Ti_{0.91}O_2$ NSs and (b) octahedral Au NPs prepared via hydrothermal method.

As shown in Figure 4.1b, the pre-synthesized Au NPs possessed octahedral morphology and relatively uniform size. To confirm the size of the octahedral Au NPs, dynamic light

scattering (DLS) technique was implemented. The octahedral Au NPs have very uniform size distribution around 69 nm. As the octahedral Au NPs synthesized via hydrothermal method are capped with cetyltrimethylammonium bromide (CTAB), their surface will be positively charged. Zeta potential measurement showed that the octahedral Au NPs carried a positive charge of +59 mV.

The synthesis routes and denotation of all the samples are shown in Scheme 4.1. When Au NPs were added to NSs suspension, Au NPs were attracted to the surface of NSs as a result of electrostatic force and so the white suspension became pink-ish. Upon the addition of hydrochloric acid, the NSs attached with octahedral Au NPs flocculated and settled, leaving the supernatant solution colourless. The flocculated NSs remained pink-ish after drying at 100 °C (O-Au-NS) and calcination at 450 °C (O-Au-A). As a comparison, other two types of Au-TiO_2 composites were also prepared, in which Au nanoparticles were introduced to different locations in the composites via direct photo-deposition. In one composite, Au particles were directly photo-deposited onto NSs before calcination, so most of the Au particles were distributed in the interior of the final composite (Au-A-1). In the other composite, however, flocculated NSs were first calcined to anatase particles (A) and then photo-deposited with Au particles (Au-A-2), so the Au particles were dispersed only on the surface of Au-A-2. It should be noted that all nanohybrids contain the same amount of Au (0.11 wt%).

Figure 4.2 illustrates the XRD patterns for all nanohybrid materials synthesized. The XRD patterns of O-Au-NS exhibited a (010) peak at $2\theta=8.74$ °, corresponding to d spacing of 1.17 nm (Figure 4.2a). There were no distinct peaks assigned to titania phase in O-Au-NS, which reflects the lack of three-dimensional order in long distance. Its XRD pattern is typical for intercalated complex with lattice expansion along the b-axis.[32, 33] The relatively broader peaks of the nanohybrid result from elastic deformation of host layers upon lattice expansion[34]. The XRD result demonstrated the randomly restacked structure of NSs in O-Au-NS. After calcination at 450 °C, the small angle peak disappeared while peaks assigned to anatase phase evolved in the XRD pattern of O-Au-A (Figure 4.2b), which indicates that the stacked sheets structure collapsed to form an anatase crystal structure. It has been previously demonstrated by Fukuda et al. that a very thin film made of several stacked layers of single titania NSs could transform into anatase at elevated temperatures and the transformed temperature decreased for thicker films.[35] The films composed of more than five layers of NSs were found to transform to anatase at 400-500 °C. Considering that our nanohybrid was prepared by stacking multilayers of $Ti_{0.91}O_2$ NSs,

calcination at 450 °C could induce the recrystallization of titania NSs to form three-dimensional crystalline anatase structure. It is noted that no peaks of Au appeared in the XRD patterns of neither O-Au-NS nor O-Au-A, which we believe is due to the fact that most Au NPs have been sandwiched between $Ti_{0.91}O_2$ NSs. Similar to O-Au-A, both Au-A-1 and Au-A-2 showed peaks of anatase phase in their XRD patterns, but a small peak at 2Θ=52 ° assigned to Au appeared (Figure 4.2c and 4.2d).

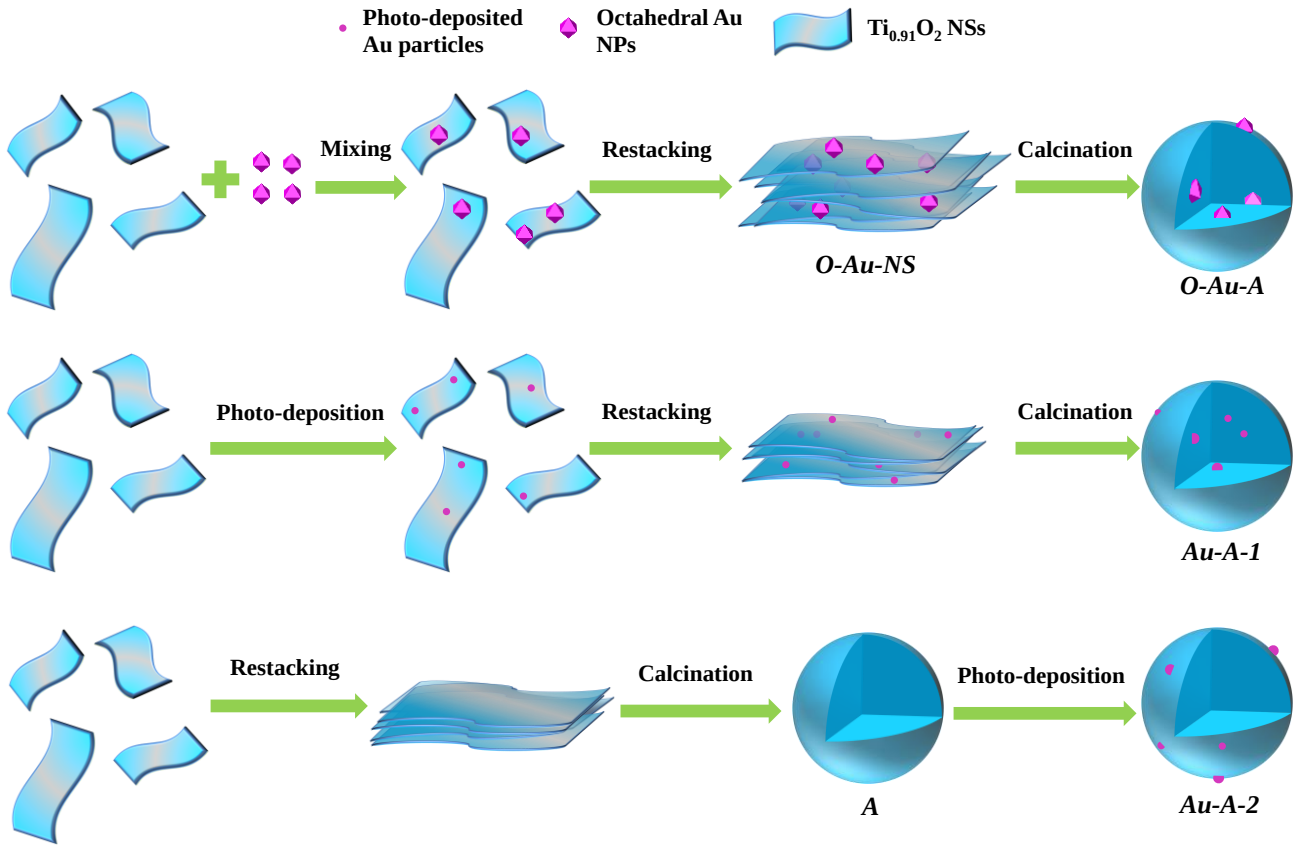

Scheme 4.1 Schematics of the synthesis routes of different hybrid samples.

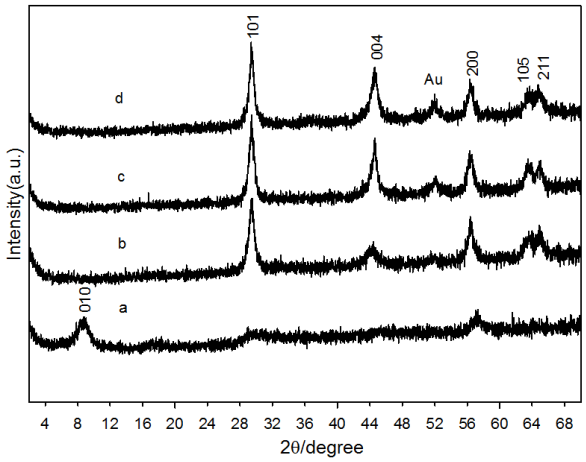

Figure 4.2 XRD patterns of (a) O-Au-NS, (b) O-Au-A, (c) Au-A-1, and (d) Au-A-2.

To investigate the morphology of the nanohybrid materials, TEM was performed. In O-Au-NS, the ultrathin NSs formed a randomly stacked structure, in which the Au NPs were extremely difficult to find (Figure 4.3a and 4.3b). This is in good agreement with our observation in the XRD patterns. After very careful searching in TEM, we only found very few octahedral Au NPs which were wrapped by NSs, and all NPs were well separated because of their small amount and thorough mixing before flocculation. After calcination at 450 °C, the stacking structure of NSs collapsed due to recrystallization, transforming to irregular-shaped porous anatase particles in O-Au-A (Figure 4.3c). Similar to O-Au-NS, Au NPs were very scarce and we were only able to find one after very long time of searching in TEM (Figure 4.3d). We believe that most Au NPs were embedded into the matrix of anatase after calcination. It is noted that after calcination, the morphology and size of Au NPs remained unchanged. We assign the stability of Au NPs to the protection of titania surrounding Au NPs. TEM images of Au-A-1 and Au-A-2 are presented in Figure 4.3e and 4.3f, respectively, and it can be seen that the photo-deposited Au particles are of irregular spherical shape and possess smaller sizes compared to the pre-synthesized octahedral Au NPs.

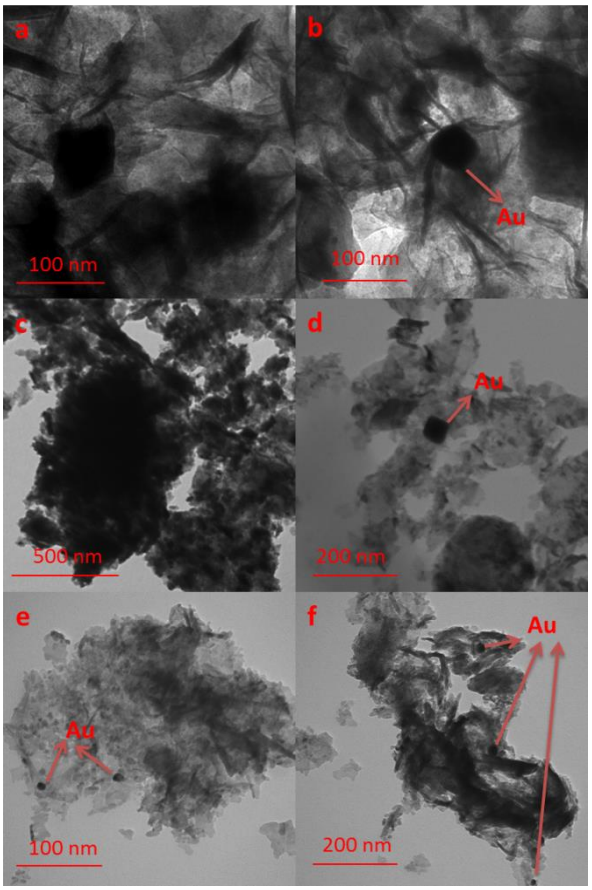

Figure 4.3 TEM images of (a) and (b) O-Au-NS, (c) and (d) O-Au-A, (e) Au-A-1 and (f) Au-A-2.

Nitrogen adsorption-desorption isotherm measurements were carried out to further study the microstructure of the prepared nanohybrids. As shown in Figure 4.4, all nanohybrids exhibited Type IV isotherms, corresponding to mesoporous structure.[36] Isotherm of O-Au-NS showed a H3-type hysteresis loop in the IUPAC classification,[36] revealing the presence of slit-shaped pores. Such type of isotherms have been observed in nickel oxide pillared titania NSs before, which highlighted the existence of open slit-shaped capillaries with very wide bodies and narrow short necks.[34] It is noted that the hysteresis loops of O-Au-NS appeared in the region with relative pressure $p/p_0>0.5$, which suggests that the majority of the porosity in the nanohybrid originates from mesopores in the randomly stracked structure.[32, 37] After calcination, an H1-type hysteresis loop appeared in the isotherms of all nanohybrids containing anatase phase (O-Au-A, Au-A-1 and Au-A-2), indicating that the materials microstructure has changed to agglomerates of spheres.[36] All results from nitrogen adsorption-desorption isotherms agreed well with our previous analysis of XRD and TEM data. Table 4.1 summarizes the surface area of all nanohybrids according to BET equation based fitting analysis. Calcination caused collapse of the stacking structure and agglomeration of anatase particles, which is reflected in the drop in surface area of O-Au-A (84 m^2/g) compared to O-Au-NS (135 m^2/g).

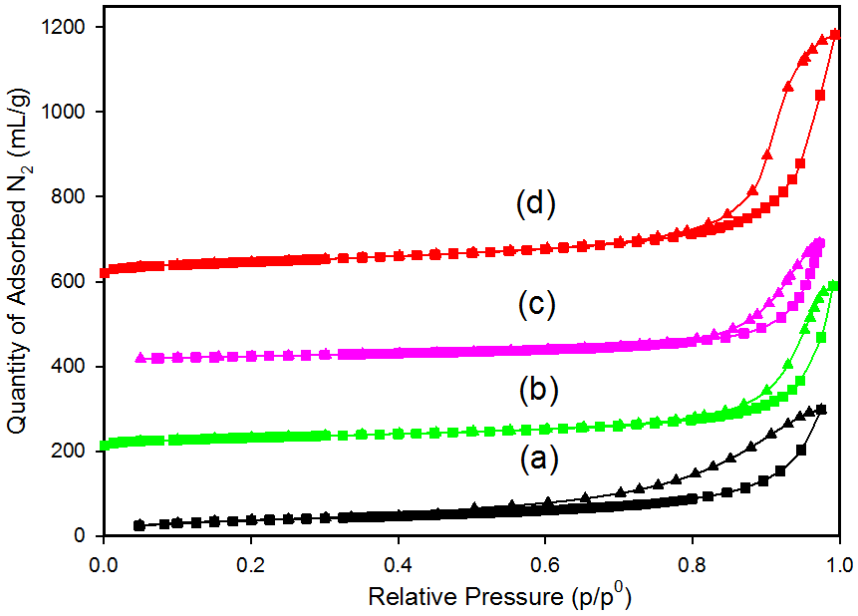

Figure 4.4 Nitrogen adsorption-desorption isotherms of (a) O-Au-NS, (b) Au-A-2, (c) O-Au-A, and (d) Au-A-1.

Table 4.1. BET surface areas of all nanohybrid materials.	
Sample	BET surface area (m^2/g)
O-Au-NS	135
O-Au-A	84
Au-A-1	166
Au-A-2	114

Chemical state analysis

To investigate the chemical states of Au present in the nanohybrids, the Au 4f levels were measured using XPS. As shown in Figure 4.5, the peaks of Au $4f_{7/2}$ located at 83.3-83.4 eV are close to metallic Au^0 $4f_{7/2}$ (84.0 eV), and different from Au^+ $4f_{7/2}$ (85.2 eV) and Au^{3+} $4f_{7/2}$ (86.7 eV),[38, 39] which confirms the metallic state of Au. The surface Au:Ti atomic ratios detected by XPS in Au-A-2 and Au-A-1 are 0.018:1 and 0.0033:1 respectively, which verified the fact that most Au particles existed at the surface of Au-A-2 and in the interior of Au-A-1. However, no signals of Au 4f were detected in XPS spectra of O-Au-NS and O-Au-A. This is possibly due to the fact that Au NPs were mostly wrapped by titania and the numbers of Au NPs were very small, so the signals of Au NPs were screened by titania. We implemented Ar ion-sputtering to O-Au-NS and O-Au-A, scanned the samples again but the signals of Au were still not detected even though a 40 nm-thick surface layer was removed. Considering the scarcity of Au NPs and the fact that the XPS technique can only detect a tiny area of the sample, this phenomenon is understandable.

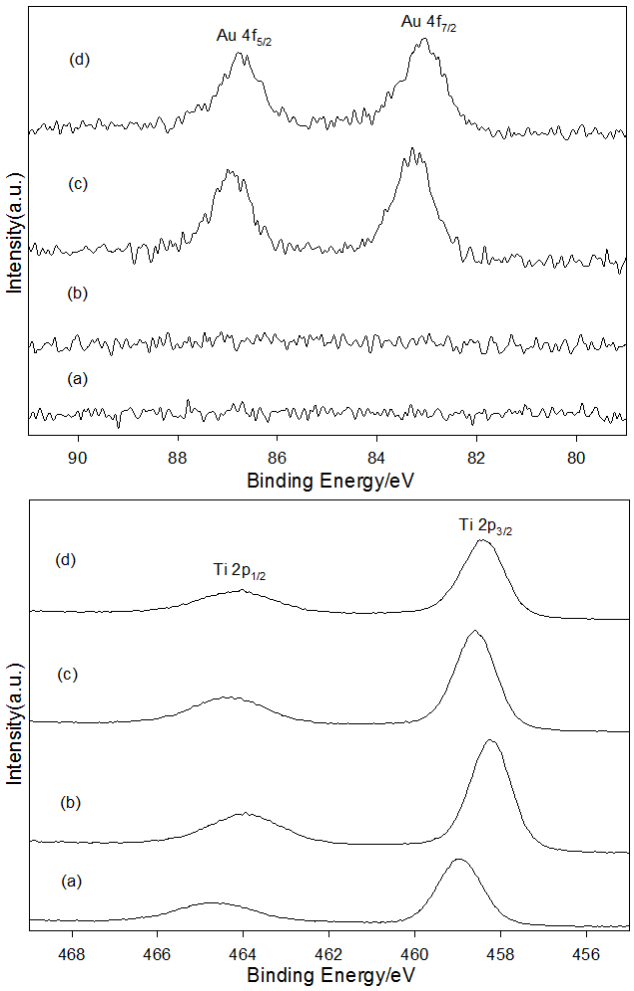

Figure 4.5 High resolution XPS spectra of Au 4f (top) and Ti 2p (bottom) in (a) O-Au-NS, (b) O-Au-A, (c) Au-A-2 and (d) Au-A-1.

Light absorption properties analysis

Figure 4.6 gives the overall light absorption spectra for all hybrid materials along with the naked titania (A). All hybrid materials containing Au particles exhibited a broad absorption peak in the wavelength range of 500-600 nm, which can be assigned to the SPR effect of Au particles. The naked titania (A) showed an absorption edge at a wavelength of 418 nm corresponding to a band gap of 2.97 eV (Figure 4.6a), which is slightly smaller than normal band gap measured for anatase (ca. 3.2 eV). Since A was prepared by calcining flocculated NSs and some organic chemicals like TBA^+ might be incorporated into flocculated NSs, a little amount of C may exist in A, leading to the extended light absorption above 400 nm. All the other hybrid materials possessed larger band gaps of around 3.12-3.26 eV, compared to A. It has been reported that in an Au-TiO_2 composite, the Fermi level equilibration between TiO_2 and Au leads to Au nanoparticles undergoing charging, which induces a negative shift in the Fermi level of TiO_2.[40-42] O-Au-NS (Figure

4.6c) and O-Au-A (Figure 4.6b) exhibited slightly red-shifted SPR peaks at around 565 nm compared to those of Au-A-1 (Figure 4.6e) and Au-A-2 (Figure 4.6d) at around 550 nm, which is due to the presence of larger octahedral Au NPs in the former two nanohybrids. This phenomenon has been observed before,[15,18,43,44] and it agrees well with the observations from TEM images. Moreover, Noguez reported that compared to polyhedral nanoparticles, spherical ones will have blue-shifted SPR peaks.[45] At the same time, we noticed that there was no obvious change of the SPR peak position after O-Au-NS was calcined, which again reflects the retainment of the size and shape of octahedral Au NPs.

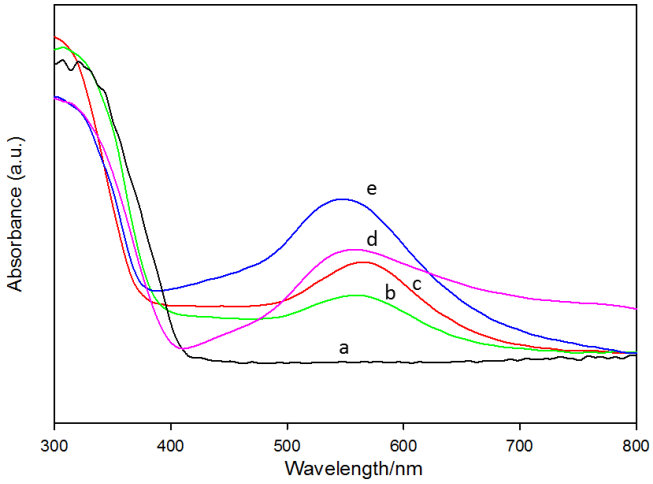

Figure 4.6 UV-Vis absorption spectra of (a) A, (b) O-Au-A, (c) O-Au-NS, (d) AU-A-2 and (e) Au-A-1.

Photocatalytic hydrogen production test

The average hydrogen evolution rates for all samples are shown in Figure 4.7. The Xe lamp produces both UV light and visible light (Figure S4.2). Naked titania A can only produce H_2 at a low rate of 1474 $\mu mol \bullet h^{-1} \bullet g^{-1}$. O-Au-NS showed very low activities, which is mainly because of its low crystallinity. However, after calcination, the hydrogen evolution rate dramatically increased (up to over 270 times), to 6753 $\mu mol \bullet h^{-1} \bullet g^{-1}$, which is 3.6 times faster than A. O-Au-A can also produce hydrogen faster than Au-A-1 (5071 $\mu mol \bullet h^{-1} \bullet g^{-1}$) and Au-A-2 (3443 $\mu mol \bullet h^{-1} \bullet g^{-1}$).

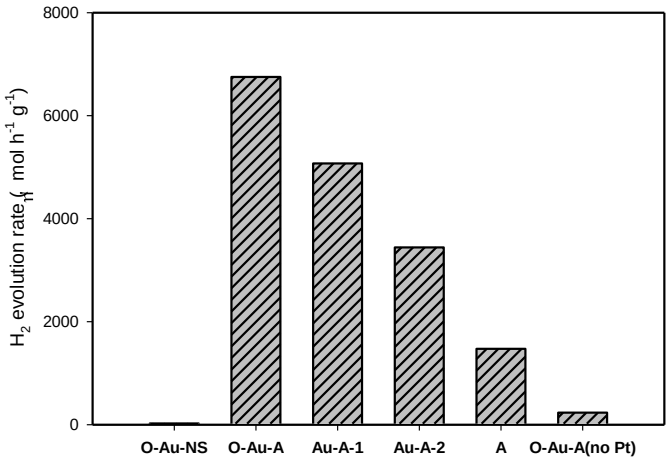

Figure 4.7 Normalized average hydrogen evolution rates for all samples prepared. Experimental conditions: 40 mg of catalyst powder photo-deposited with 1wt% Pt (except the last one) was dispersed in 300 mL of aqueous ethanol solution (20vol%), light source was 300 W Xenon lamp.

Analysis on the role of Au NPs

The most efficient nanohybrid, O-Au-A, can evolve hydrogen more than 3.6 times faster than naked titania A, even though the ratio of Au is extremely low (ca. 0.11 wt%). The phenomenon indicates the vital role of octahedral Au NPs in the photocatalytic reaction. As mentioned before, several mechanisms regarding the role of Au NPs have been proposed by researchers. We conducted some experiments to investigate the roles of Au NPs in our material system.

Conventionally, Au in a metal-semiconductor composite system can act as a sink for photoinduced electrons and catalyse the reduction of water molecules, in which way Au improves the photocatalytic performance as the co-catalyst. In order to effectively act as co-catalyst, Au must exist in the interfacial region between semiconductors and the solution. In a control experiment, we conducted hydrogen evolution with O-Au-A in the absence of Pt. Surprisingly, O-Au-A alone produced even less hydrogen compared to A-TiO_2 deposited with Pt, as shown in Figure 4.7. This phenomenon can be explained in the way that due to the scarcity of Au NPs at the surface of O-Au-A, the ability of octahedral Au NPs as co-catalyst was very limited in the nanohybrid. However, we believe that octahedral Au NPs still partly acted as co-catalyst, which is a minor function of Au NPs in our nanocomposite system.

In the direct electron injection mechanism, Au NPs undergo SPR-induced excitation upon visible light irradiation and electrons in the surface plasmon (SP) states possess enough energy to be injected to the conduction band of the semiconductors. This mechanism has

been very controversial in Au-TiO_2 composite systems. Even though water splitting under visible light has been reported by several groups,[2, 4, 10] no direct evidence of electron transfer between Au particles and titania were provided. At the same time, the possibility of photoexcitation of Au NPs by visible light has been ruled out in several papers of Cronin's Group in recent years.[38, 46, 47] They claimed that there is no highest occupied molecular orbital-lowest unoccupied molecular orbital (HOMO-LUMO) energy band configuration like semiconductors in a plasmon excitation, so the visible activities originated from the sub-bandgap transition in TiO_2 with some dopants. In another control experiment, we equipped the Xe lamp with a 420 nm cut-off filter so only visible light can reach the reactor. For all samples, no hydrogen can be detected. Since titania cannot be excited by photons with wavelength longer than 420 nm, Au NPs did not seem to act as visible light sensitizer in our case. Similar results were obtained by Chen and his co-workers.[48] In their work, they synthesized an Au-TiO_2 (Degussa P25) composite, which showed no appreciable H_2 evolution under only visible light. Although their composite produced more hydrogen under UV plus visible light than under pure UV light due to SPR effect, they did not give detailed explanation.

From the discussion above, octahedral Au NPs seem to work insignificantly as co-catalyst and hardly as visible photosensitizer. However, the dramatically improved hydrogen production capability of O-Au-A compared to A highlights the importance of octahedral Au NPs. Therefore, in our opinion, the other two effects of SPR, that is, intensified localized electric field and photon scattering, are likely to work at the same time to enhance the photocatalytic water splitting. The mechanism of the two effects is shown in Scheme 4.2. Upon SPR-induced excitation of Au NPs, charges are concentrated at the metal-semiconductor interface, yielding a dramatic amplification of localized electric field.[13] In this case, Au NPs essentially act as light concentrators and the localized field is distributed very unevenly, with the highest intensity at the surface of Au NPs and decreasing exponentially within 20-30 nm from the surface and linearly further away.[11] Through finite-difference time-domain (FDTD) simulation, Christopher et al. reported that an isolated Ag nanocube with an edge length of 75 nm can produce a SPR-induced electric fields with intensity of ~10^3 times larger than the incident photon flux while two same nanocubes with 1 nm distance can enhance the light intensity up to ~10^6 times.[49] Using similar FDTD simulation, Liu et al. also found that the localized SPR-induced electric field intensity in their Au-anodic TiO_2 film can reach up to 1000 times that of the incident electric field intensity.[46] This largely enhanced local light intensity will promote photoexcitation of

semiconductor and thus produce more electrons and holes, considering that the charger pair formation rate is proportional to the local light intensity.[11] In addition, the plasmonic nanostructure acts as a nanomirror, maintaining the resonant photons in the system for a longer time.[11, 50, 51] In this way, photons are given many more passes through the materials and utilized more efficiently. It has been previously found that with the increase of the size of metal nanoparticles, the photon scattering effect become more significant.[51] This photon scattering mechanism can explain why O-Au-A showed better photocatalytic performance than Au-A-1 and Au-A-2. The bigger octahedral Au NPs embedded in O-Au-A can scatter photons throughout the catalyst particles more efficiently than the small irregular-spherical Au particles in Au-A-1 and Au-A-2.

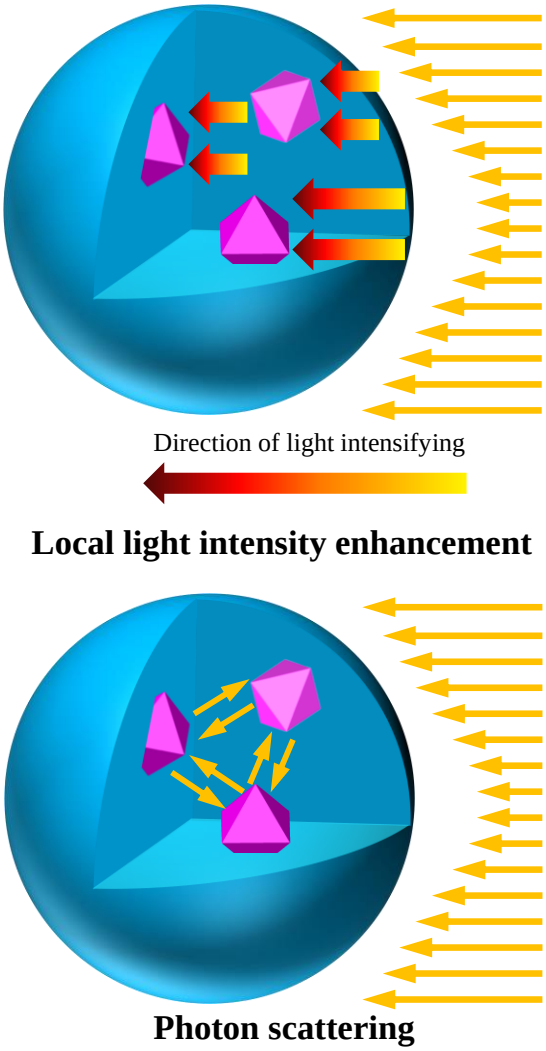

Scheme 4.2 Schematics of the two effects of octahedral Au NPs: Local light intensity enhancement and photon scattering.

So to briefly conclude, we believe that Au NPs mainly function to enhance local light intensity and scatter photons in our system. On the contrary, the possibility of photosensitization of Au NPs can be ruled out and the role as co-catalyst is minor.

4.4 Conclusions

We demonstrated a method to prepare Au-TiO_2 nanohybrid with well separated octahedral Au NPs of relatively large size. By using $Ti_{0.91}O_2$ NSs and pre-synthesized Au NPs as the starting materials, it is easy to achieve the embedding of Au NPs with designed size and morphology into the matrix of anatase. The synthesized nanohybrid showed much better photocatalytic hydrogen evoluition performance compared to naked titania and titania photo-deposited with Au due to the excellent SPR properties of the pre-synthesized octahedral Au NPs. The strategy is important for the development of nanohybrid materials, which is applicable to both other NSs ($Nb_6O_{17}^{4-}$, $Ca_2Nb_3O_{10}^{-}$, etc.) and plasmonic metal NPs (Ag, Cu, etc.).

4.5 References

1. H. Wang, T. T. You, W. W. Shi, J. H. Li and L. Guo, *J. Phys. Chem. C*, 2012, **116**, 6490-6494.

2. S. Mubeen, J. Lee, N. Singh, S. Krämer, G. D. Stucky and M. Moskovits, *Nat. Nanotech.*, 2013, **8**, 247-251.

3. G. Liu, L. Wang, H. G. Yang, H. M. Cheng and G. Q. M. Lu, *J. Mater. Chem.*, 2009, **20**, 831-843.

4. C. u. Gomes Silva, R. Juárez, T. Marino, R. Molinari and H. García, *J. Am. Chem. Soc.*, 2010, **133**, 595-602.

5. H. Irie, Y. Watanabe and K. Hashimoto, *J. Phys. Chem. B*, 2003, **107**, 5483-5486.

6. X. W. Wang, G. Liu, Z. G. Chen, F. Li, L. Z. Wang, G. Q. Lu and H. M. Cheng, *Chem. Commun.*, 2009, 3452-3454.

7. G. R. Bamwenda, S. Tsubota, T. Nakamura and M. Haruta, *J. Photochem. Photobiol. A*, 1995, **89**, 177-189.

8. T. Puangpetch, S. Chavadej and T. Sreethawong, *Energy Conv. Manag.*, 2011, **52**, 2256-2261.

9. M. Murdoch, G. Waterhouse, M. Nadeem, J. Metson, M. Keane, R. Howe, J. Llorca and H. Idriss, *Nat. Chem.*, 2011, **3**, 489-492.

10. H. Yuzawa, T. Yoshida and H. Yoshida, *Appl. Catal. B*, 2012, **115–116**, 294-302.

11. S. Linic, P. Christopher and D. B. Ingram, *Nat. Mater.*, 2011, **10**, 911-921.

12. K. L. Kelly, E. Coronado, L. L. Zhao and G. C. Schatz, *J. Phys. Chem. B*, 2003, **107**, 668-677.

13. Y. Xia and N. J. Halas, *MRS Bull.*, 2005, **30**, 338-348.

14. N. Halas, *MRS Bull.*, 2005, **30**, 362-367.

15. C. J. Orendorff, T. K. Sau and C. J. Murphy, *Small*, 2006, **2**, 636-639.

16. P. J. Chung, L. M. Lyu and M. H. Huang, *Chem. Eur. J.*, 2011, **17**, 9746-9752.

17. M. L. Personick, M. R. Langille, J. Zhang and C. A. Mirkin, *Nano Lett.*, 2011, **11**, 3394-3398.

18. E. Kowalska, O. O. P. Mahaney, R. Abe and B. Ohtani, *Phys. Chem. Chem. Phys.*, 2010, **12**, 2344-2355.

19. N. Sakai, Y. Fujiwara, Y. Takahashi and T. Tatsuma, *ChemPhysChem*, 2009, **10**, 766-769.

20. Y. Tian and T. Tatsuma, *J. Am. Chem. Soc.*, 2005, **127**, 7632-7637.

21. A. Primo, A. Corma and H. García, *Phys. Chem. Chem. Phys.*, 2010, **13**, 886-910.

22. Z. F. Bian, J. Zhu, F. L. Cao, Y. F. Lu and H. X. Li, *Chem. Commun.*, 2009, 3789-3791.

23. R. J. Dillon, J. B. Joo, F. Zaera, Y. D. Yin and C. J. Bardeen, *Phys. Chem. Chem. Phys.*, 2013, **15**, 1488-1496.

24. N. Zhang, S. Q. Liu, X. Z. Fu and Y. J. Xu, *J. Phys. Chem. C*, 2011, **115**, 9136-9145.

25. X. F. Wu, H. Y. Song, J. M. Yoon, Y. T. Yu and Y. F. Chen, *Langmuir*, 2009, **25**, 6438-6447.

26. S. H. Liu, S. Q. Bai, Y. G. Zheng, K. W. Shah and M. Y. Han, *ChemCatChem*, 2012, **4**, 1462-1484.

27. H. Hata, S. Kubo, Y. Kobayashi and T. E. Mallouk, *J. Am. Chem. Soc.*, 2007, **129**, 3064-3065.

28. T. Sasaki, M. Watanabe, H. Hashizume, H. Yamada and H. Nakazawa, *J. Am. Chem. Soc.*, 1996, **118**, 8329-8335.

29. T. Sasaki and M. Watanabe, *J. Am. Chem. Soc.*, 1998, **120**, 4682-4689.

30. T. Sasaki and M. Watanabe, *J. Phys. Chem. B*, 1997, **101**, 10159-10161.

31. G. Liu, L. Wang, C. Sun, Z. Chen, X. Yan, L. Cheng, H. M. Cheng and G. Q. M. Lu, *Chem. Commun.*, 2009, 1383-1385.

32. T. W. Kim, S. J. Hwang, Y. Park, W. Choi and J. H. Choy, *J. Phys. Chem. C*, 2007, **111**, 1658-1664.

33. T. W. Kim, S. G. Hur, S. J. Hwang and J. H. Choy, *Chem. Commun.*, 2006, 220-222.

34. T. W. Kim, S. J. Hwang, S. H. Jhung, J. S. Chang, H. Park, W. Choi and J. H. Choy, *Adv. Mater.*, 2008, **20**, 539-542.

35. K. Fukuda, Y. Ebina, T. Shibata, T. Aizawa, I. Nakai and T. Sasaki, *J. Am. Chem. Soc.*, 2007, **129**, 202-209.

36. K. S. W. Sing, D. H. Everett, R. A. W. Haul, L. Moscou, R. A. Pierotti, J. Rouquerol and T. Siemieniewska, *Pure Appl. Chem.*, 1985, **57**, 603-619.

37. T. W. Kim, H. W. Ha, M. J. Paek, S. H. Hyun, I. H. Baek, J. H. Choy and S. J. Hwang, *J. Phys. Chem. C*, 2008, **112**, 14853-14862.

38. W. B. Hou, W. H. Hung, P. Pavaskar, A. Goeppert, M. Aykol and S. B. Cronin, *ACS Catal.*, 2011, **1**, 929-936.

39. Y. Tian and T. Tatsuma, *J. Am. Chem. Soc.*, 2005, **127**, 7632-7637.

40. O. Rosseler, M. V. Shankar, M. K. L. Du, L. Schmidlin, N. Keller and V. Keller, *J. Catal.*, 2010, **269**, 179-190.

41. S. W. Chen and R. W. Murray, *J. Phys. Chem. B*, 1999, **103**, 9996-10000.

42. V. Subramanian, E. E. Wolf and P. V. Kamat, *J. Am. Chem. Soc.*, 2004, **126**, 4943-4950.

43. D. Andreescu, T. K. Sau and D. V. Goia, *J. Colloid Interface Sci.*, 2006, **298**, 742-751.

44. A. M. Schwartzberg, T. Y. Olson, C. E. Talley and J. Z. Zhang, *J. Phys. Chem. B*, 2006, **110**, 19935-19944.

45. C. Noguez, *J. Phys. Chem. C*, 2007, **111**, 3806-3819.

46. Z. Liu, W. Hou, P. Pavaskar, M. Aykol and S. B. Cronin, *Nano Lett.*, 2011, **11**, 1111-1116.

47. W. B. Hou, Z. W. Liu, P. Pavaskar, W. H. Hung and S. B. Cronin, *J. Catal.*, 2011, **277**, 149-153.

48. J. J. Chen, J. C. S. Wu, P. C. Wu and D. P. Tsai, *J. Phys. Chem. C*, 2011, **115**, 210-216.

49. P. Christopher, H. Xin, A. Marimuthu and S. Linic, *Nat. Mater.*, 2012, **11**, 1044-1050.

50. C. Burda, X. B. Chen, R. Narayanan and M. A. El-Sayed, *Chem. Rev.*, 2005, **105**, 1025-1102.

51. D. D. Evanoff and G. Chumanov, *ChemPhysChem*, 2005, **6**, 1221-1231.

4.6 Supporting information

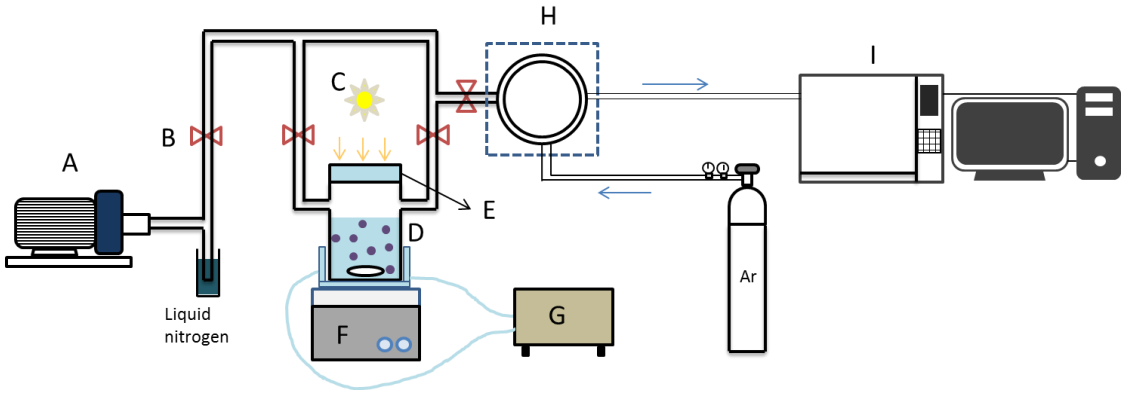

Figure S4.1 Overall system set-up for solar water splitting. A, pump; B, on/off valve; C, Xenon lamp; D, reactor containing reaction suspension; E, water filter; F, magnetic stirrer; G, cooling water cycle system; H, sampling device, and I, gas chromatography.

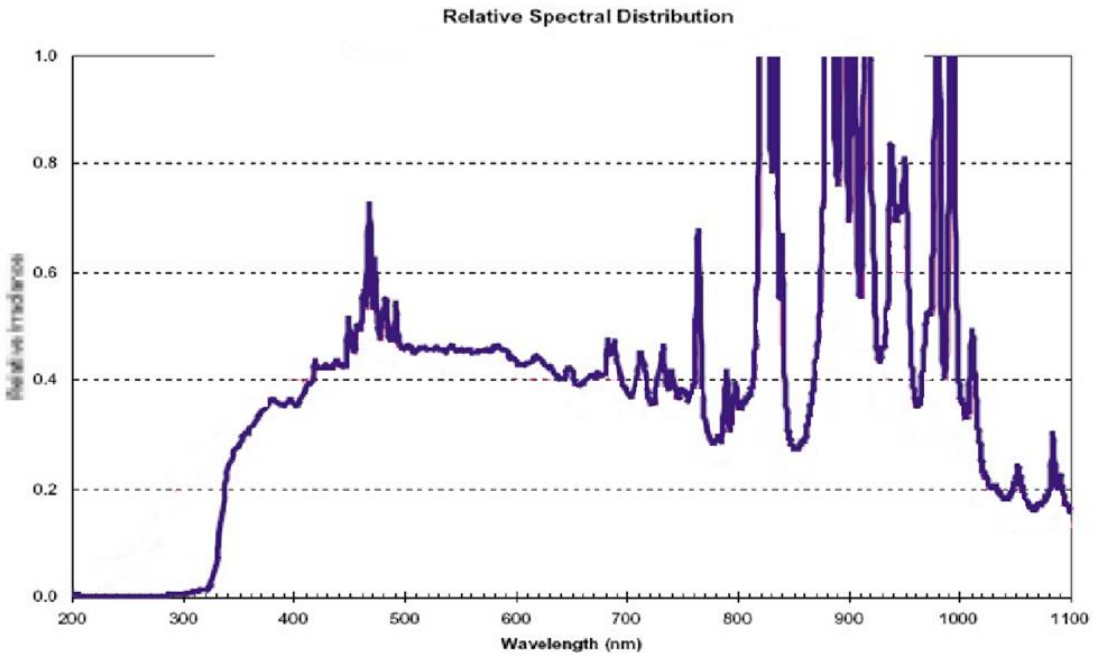

Figure S4.2 Light spectrum of the Xe lamp.

5. A nanohybrid of CdTe@CdS nanocrystals and titania nanosheets with p-n nanojunctions for improved visible light-driven hydrogen production

A nanohybrid of CdTe@CdS nanocrystals and titania nanosheets with p-n nanojunctions for improved visible light-driven hydrogen production

Zheng Xing, Yang Bai, Xu Zong, Yian Zhu, ZhiGang Chen, Lianzhou Wang*

Submitted to ***Nanoscale***

5.1 Abstract

A nanohybrid photocatalyst composed of CdTe@CdS nanocrystals and single-layered titania nanosheets was synthesized through a well-defined restacking approach. The nanohybrid possessed an expanded layered structure, with ultrathin titania nanosheets randomly restacked upon each other and CdTe@CdS nanocrystals sandwiched between the titania nanosheets. The introduction of CdTe@CdS nanocrystals not only extended the light absorption of titania nanosheets to the visible range, but also formed p-n nanojunctions in the nanohybrid. This nanohybrid containing same amount of CdTe@CdS nanocrystals showed 43.4 times higher activity than pure CdTe@CdS nanocrystals for hydrogen production under visible light irradiation (λ> 420 nm) while titania nanosheets stayed inactive. The excellent photocatalytic efficiency of the nanohybrid can be attributed to the effective charge separation, which is achieved by the synergetic effect of suitable arrangement of energy bands and the p-n nanojunctions.

5.2 Introduction

Photocatalytic hydrogen production provides a potential solution for the future energy shortage, and thus draws great attention worldwide.[1] In photocatalytic reactions (artificial photosynthesis), a semiconductor photocatalyst is used to absorb incident light, generate excited electrons and holes, and subsequently drive the reactions. Despite the large amount of work dedicated to developing different photocatalysts, titanium oxide (TiO_2) remains the most intensively researched material.[2] As a typical n-type semiconductor, TiO_2 has good stability and relatively good photocatalytic performance upon band gap excitation. However, due to its relative large band gap of 3.2 eV, TiO_2 is only able to utilize the high-energy UV irradiation, which merely accounts for less than 5% of the overall sunlight spectrum. In order to extend the light absorption, researchers have tried to dope TiO_2 with metal and non-metal elements, which can effectively introduce visible light absorbance to TiO_2.[3] However, doping with guest elements often introduces recombination centers for

electrons and holes, and although visible light activity can be obtained, the photocatalytic performance under the whole solar spectrum is deteriorated.[4] Another method to extend the light absorption is to couple TiO_2 with other narrow-band-gap semiconductors to form a heterogeneous structure.[5] Unlike doping in TiO_2, heterogeneous photocatalysts have improved charge separation because the energy band alignment in the composite structure can allow photoinduced charge carriers to flow between the narrow-band-gap semiconductor and TiO_2 upon visible light illumination.

In the heterogeneous structures, the physicochemical interaction between different components near the interfacial region is critically important. In this regard, nanostructured materials are the ideal building blocks for heterogeneous structure due to their unique surface properties and enlarged specific surface area.[6] The successful preparation of various inorganic 2D semiconductor nanosheets (NSs) with surface charges,[7, 8] makes it possible to deliberately synthesize some unique heterogeneous structures. Based on 2D semiconductor NSs, Hwang and his co-workers synthesized a series of hybrid materials with very porous structure and well-controlled electronic properties, by coupling NSs with guest species including metal oxide nanoparticles and different types of NSs.[9-12] In particular, the assembly of 2D NSs and 0D nanoparticles will form a layered structure with 0D nanoparticles pillared between 2D NSs, as a result of the house-of-cards-type stacking of the sheet-like crystallites. Our group also reported a nanohybrid of titania NSs and anatase nanoparticles, which greatly improved the performance of dye-sensitized solar cell (DSSC) due to suppressed charge recombination and unique properties related to its special porous structure such as excellent light scattering and increased dye adsorption.[13]

To make the aforementioned heterogeneous structure, various guest nanoparticles can be incorporated into the restacked NSs. Among all different types of nanoparticles, we are particularly interested in metal chalcogenides nanocrystals (NCs) such as CdTe, CdSe, CdS, etc. because they generally possess small band gaps (visible light absorption) and high conduction band (driving force for hydrogen production).[14-17] Moreover, as these NCs are capped with stabilizing organic molecules, their surface charges can be easily tailored by ligand exchange or using different stabilizing molecules.[17, 18] Compared to CdSe and CdS, CdTe has higher conduct band edge,[19, 20] which makes it an excellent material not only for photocatalytic and photoelectrochemical hydrogen production, but also for quantum dot sensitized solar cells (QDSSCs).[15, 19, 21, 22] Besides single phase NCs, type-II core-shell structure NCs such as CdTe@CdS, CdTe@CdSe and CdSe@CdS have also been constructed, which are found to have some advantages including prolonged charge

lifetime, enhanced charge transfer, extended absorption edge and improved photo-stability.[19, 22, 23] A good example of typical type-II core-shell structure is CdTe@CdS, in which electrons are allowed to be transferred to the shell and the holes to the core. In addition, as CdTe is p-type semiconductor while CdS is n-type, a p-n nanojunction will form at the interface, which can further promote charge separation with its induced electric field.[19] The concept of forming p-n junction in photocatalysts has been found to be very effective for promoting photocatalytic performance.[24-26] For example, Meng and his co-workers directly grew p-type MoS_2 nanoplatelets onto n-type nitrogen-doped reduced graphene oxide (rGO).[27] The nanoscale p-n junctions in the composites significantly improved the photocatalytic hydrogen production performance. Therefore, the special properties of CdTe@CdS make it a potentially better photocatalyst compared to pure CdTe.

Herein we reported a new nanohybrid photocatalyst for efficient visible light hydrogen production, which was prepared by hybridization of single-layered titania NSs and CdTe@CdS NCs. Even though titania NSs were inactive in the visible region (λ>420 nm) while pure CdTe@CdS NCs had extremely low activity, the as-prepared nanohybrid showed dramatically enhanced photocatalytic activity under the same conditions. By coupling CdTe@CdS NCs and titania NSs, many p-n nanojunctions are formed in the nanohybrid, which can enhance the electron transfer from CdTe to titania, suppress the charge recombination, and subsequently improve the photocatalytic hydrogen production.

5.3 Results and discussion

The synthesis of the nanohybrid material is schematically shown in Scheme 5.1. CdTe@CdS NCs and $Ti_{0.91}O_2$ NSs were first thoroughly mixed under stirring conditions. The mixed suspension remained stable because both $Ti_{0.91}O_2$ NSs and CdTe@CdS NCs carry negative charges. $Ti_{0.91}O_2$ NSs have been reported to possess negative charge of ca. -39 mV.[29] Moreover, CdTe@CdS NCs also carry negative charge (-28 mV detected by Zeta potential measurement) because of the thiol group in the capping agent, that is, mercaptosuccinic acid (MSA). After the complete mixing of NSs and NCs, poly(ethyleneimine) (PEI) chains with positive charges were added to the suspension. The introduction of PEI will not only bind NSs and NCs together as glue, but also restack the $Ti_{0.91}O_2$ NSs. The randomly restacked $Ti_{0.91}O_2$ NSs will form a layered structure with CdTe@CdS NCs located in the interlayer gallery. This nanohybrid material is denoted as CT.

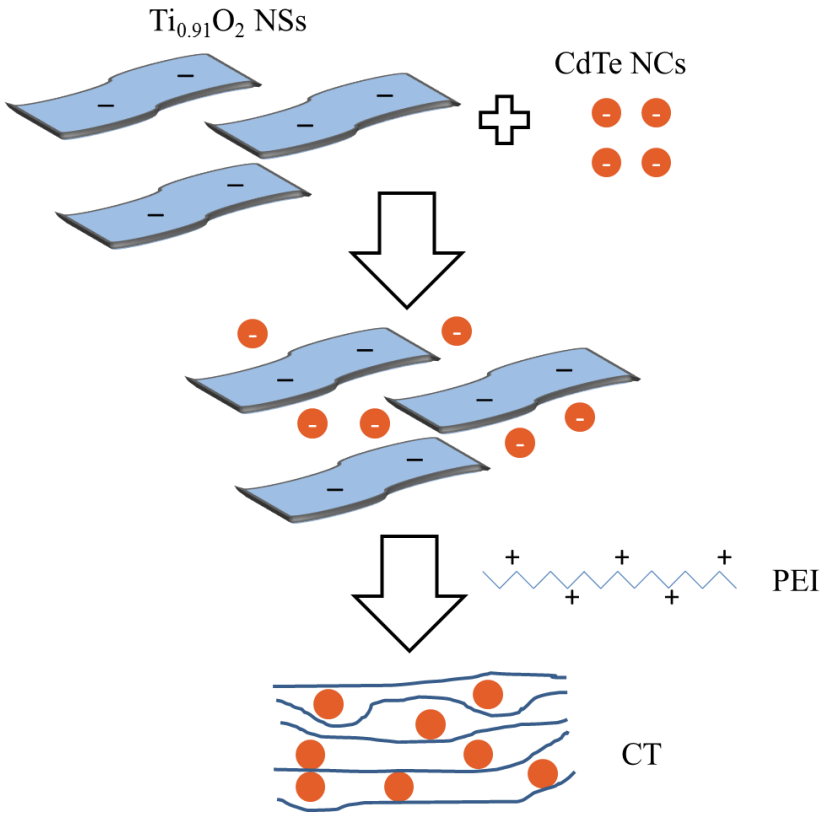

Scheme 5.1 Formation mechanism of the nanohybrid CT.

To analyze the structure of the NCs and the nanohybrid, X-ray diffraction (XRD) was conducted. The XRD pattern of the as-prepared CdTe@CdS NCs (Figure S5.1, ESI†) indicated a cubic crystal structure, with peaks located between cubic CdTe and cubic CdS. The XRD pattern proved the co-existence of both CdTe and CdS in the NCs. Similar phenomenon was observed in previous studies of CdTe@CdS core-shell NCs.[28, 30]

After the hybridization of $Ti_{0.91}O_2$ NSs and CdTe@CdS NCs, the XRD pattern of CT (Figure 5.1c) showed a broad peak around 10.8 °, which is a typical feature of restacked layered materials.[31, 32] Several other weak peaks were also observed, which can be assigned to the individual $Ti_{0.91}O_2$ NS layers.[33] As the ratio of CdTe@CdS NCs in CT is very low (2.1 wt% of CdTe), we were not able to identify the peaks of CdTe or CdS.

To compare the interlayer spacing difference between CT and the titanate precursors, we also conducted XRD of both $Cs_{0.68}Ti_{1.83}O_4$ and $H_{0.68}Ti_{1.83}O_4 \cdot H_2O$. Based on the position of the (020) peak, the layered titanate precursor $Cs_{0.68}Ti_{1.83}O_4$ has a basal spacing of 0.86 nm (Figure 5.1a), which is expanded to 0.95 nm after proton exchange (Figure 5.1b). The nanohybrid CT (Figure 5.1c) showed a similar gallery spacing of 0.95 nm to that of the protonated titanate $H_{0.68}Ti_{1.83}O_4 \cdot H_2O$. The increased interlayer distance indicated the successful intercalation of CdTe@CdS NCs and PEI chains. Moreover, the expanded

interlayer space can also promote electrolyte to diffuse into the space between layers and react with active sites of the photocatalyst.[34]

To explore the morphology of the nanohybrid, HRTEM was performed. Figure 5.2a showed a typical cross-sectional view of CT, displaying a layered structure composed of stacked $Ti_{0.91}O_2$ NS (parallel dark lines). The interlayer spacing of CT was estimated to be ca. ~0.93 nm, which is in good agreement with the calculation based on its XRD pattern. Moreover, CdTe@CdS NCs were observed in the HRTEM images of CT (Figure 5.2b). The sizes of NCs were determined to be 3-4 nm, and the clear interplanar spacing of 0.18 nm corresponds to the (311) lattice fringe of the CdTe crystal. The observations in HRTEM confirm the proposed layered structure of the nanohybrid.

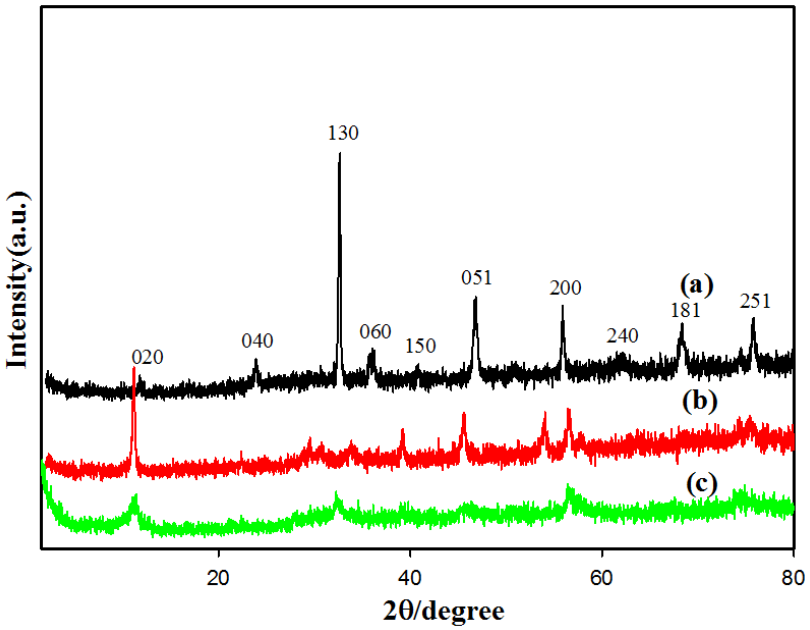

Figure 5.1 The powder XRD patterns of (a) $Cs_{0.68}Ti_{1.83}O_4$, (b) $H_{0.68}Ti_{1.83}O_4 \cdot H_2O$ and (c) CT.

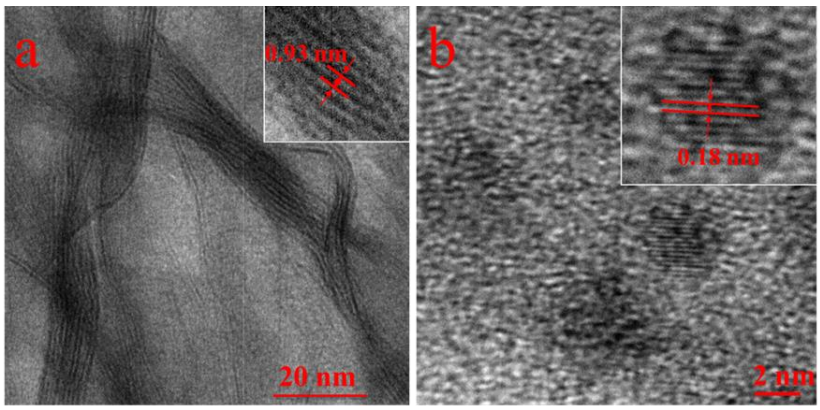

Figure 5.2 HRTEM images of CT. (a) relatively large-scale view of the restacked layered structure, and (b) local view of the CdTe@CdS NCs.

The UV-Vis absorption spectrum of CdTe@CdS NCs (Figure 5.3b) showed a low energy excitonic absorption peak around 570 nm, which is in good agreement with previous reported NCs of similar sizes.[21, 28] Peng and his co-workers[35] built up a link between the position of this excitonic absorption peak with the size of CdTe NCs, as shown in Eq. 5.1. Calculated from this equation, the size of our CdTe is 3.43 nm, which is very close to our observations in HRTEM. The titania NSs have an absorption edge around 300 nm (Figure 5.3a), corresponding to a band gap of 4.1 eV, which makes it unable to capture visible light. After the hybridization, CT underwent significant enhancement of visible absorption, with an absorption edge of 670nm (Insert of Figure 5.3). The extended light absorption of CT also indicated the successfully intercalation of CdTe@CdS NCs.

$$D = (9.8127 \times 10^{-7})\lambda^3 - (1.7147 \times 10^{-3})\lambda^2 + (1.0064)\lambda - (194.84) \qquad \text{(Eq. 5.1)}$$

Where D (nm) is the size of CdTe NCs and λ is the wavelength of the low energy excitonic absorption peak.

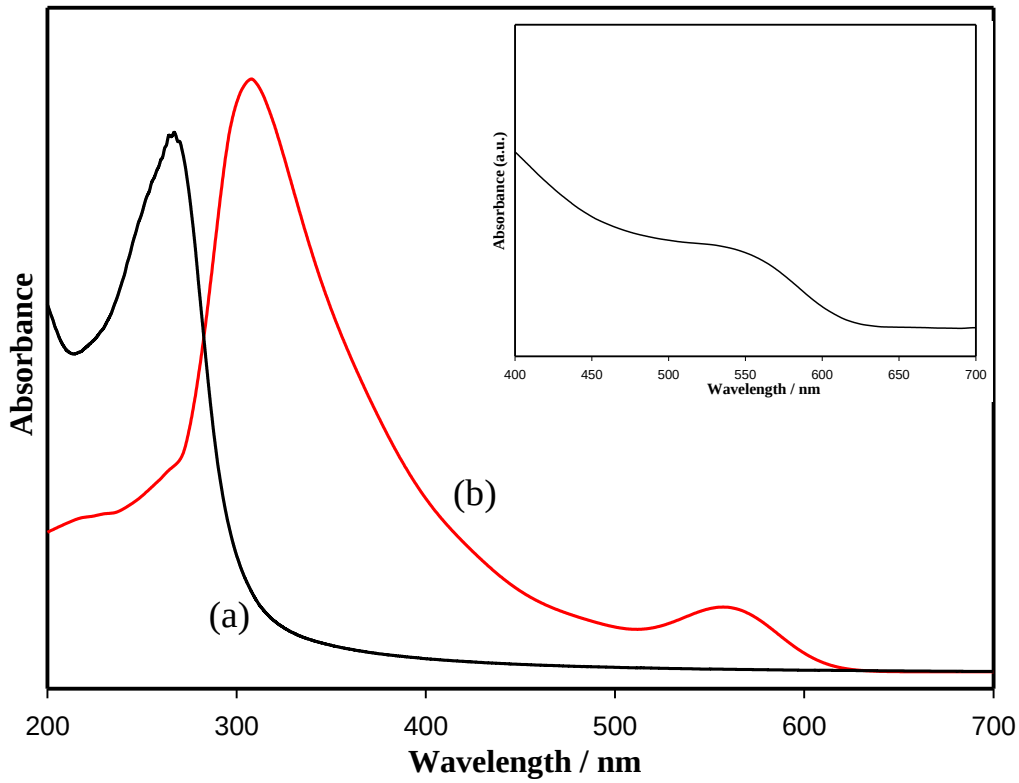

Figure 5.3 UV-Visible absorption spectra of (a) $Ti_{0.91}O_2$ NSs suspension and (b) CdTe@CdS NCs suspension. Insert: powder UV-Visible absorption spectrum of CT.

To further confirm the existence of CdTe@CdS NCs in the nanohybrid, X-ray photoelectron spectroscopy (XPS) analysis was performed. As shown in Figure 5.4, Te 3d showed two peaks, with Te $3d_{5/2}$ and Te $3d_{3/2}$ located at 572.5 eV and 582.8 eV

respectively. The position of Te 3d peaks are very close to previous reports of Te 3d in CdTe,[36, 37] which indicates that Te exists in the form of Te^{2-} instead of TeO_2 or Te. The S 2p spectrum can be fitted with a single doublet with S $2p_{3/2}$ located at 161.4 eV and S $2p_{1/2}$ at 162.6 eV, when using Shirley type background function. This doublet agreed well with S 2p in CdS.[28, 38] It has been reported that a Cd-MSA complex will form on the surface of CdTe NCs during the synthesis, which gradually decomposes and generates a layer of CdS.[28] After the hydrothermal reaction, a CdTe@CdS core-shell structure will be obtained. The analysis of S 2p spectrum verified the formation of CdTe@CdS core-shell structure. The peak positions of Cd 3d are very close in CdTe and CdS.[36-39] The peaks of Cd $3d_{5/2}$ and Cd $3d_{3/2}$ of CT are centered at 405.2 eV and 411.9 eV, respectively, which fall into the region of Cd 3d in CdTe and CdS.

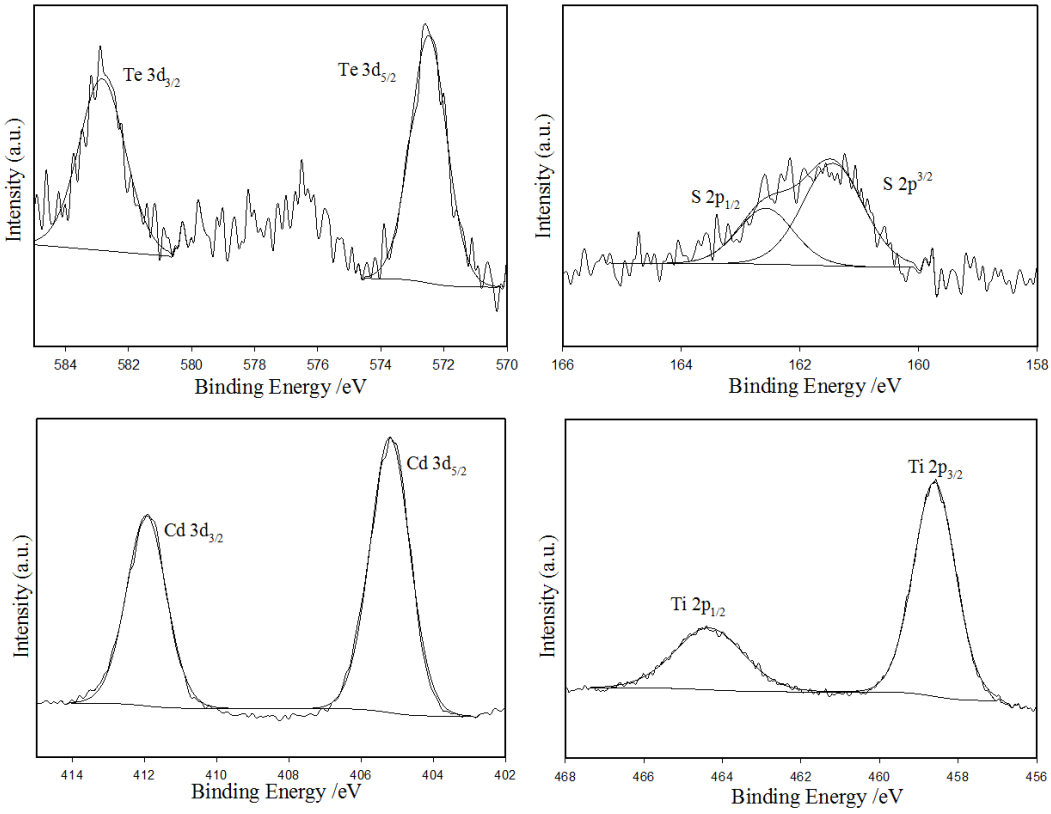

Figure 5.4 High-resolution XPS spectra for Te 3d, S 2p, Cd 3d and Ti 2p in CT.

The photocatalytic activity of CT was tested by hydrogen production under visible light illumination. As shown in Figure 5.5, pure $Ti_{0.91}O_2$ NSs (25 mL) were not able to produce any hydrogen and CdTe@CdS NCs (10 mL) can only produce hydrogen at a very slow rate of 0.47 $\mu mol \cdot h^{-1}$. Impressively, when CT (ca. 45 mg) containing the same amount of CdTe@CdS NCs was tested, the activity was significantly improved and an average hydrogen evolution rate of 20.85 $\mu mol \cdot h^{-1}$ was obtained, which is 43.4 times higher than pure CdTe@CdS NCs. This gives a normalized hydrogen rate of 463.24 $\mu mol \cdot h^{-1} \cdot g^{-1}$

based on the weight of CT, even though the ratio of the NCs in CT is very low (ca. 2.1 wt% in terms of the CdTe core in the CdTe@CdS NCs). In a control experiment, we also tested hydrogen production with only the sacrificial agent Na_2S/Na_2SO_3 solution, and no hydrogen was detected. Figure 5.6 shows the typical time course of hydrogen evolution over CT. There is a subtle induction time in the first hour, [21] which is possibly due to the photodeposition of Pt.

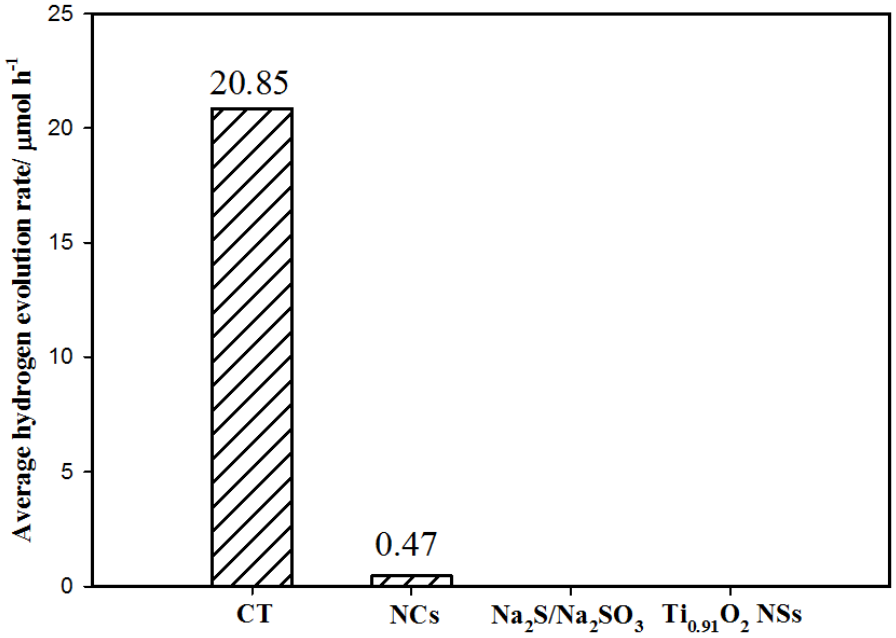

Figure 5.5 Normalized hydrogen production rates of CT, pure CdTe@CdS NCs, Na_2S/Na_2SO_3 solution and $Ti_{0.91}O_2$ NSs. In the test, the catalyst was loaded with 1 wt% Pt as cocatalyst, and 300 mL of Na_2S/Na_2SO_3 (0.01 mol) solution was used as the sacrificial agent. High energy Xenon lamp equipped with 420 nm cut-off filter was used as the light source.

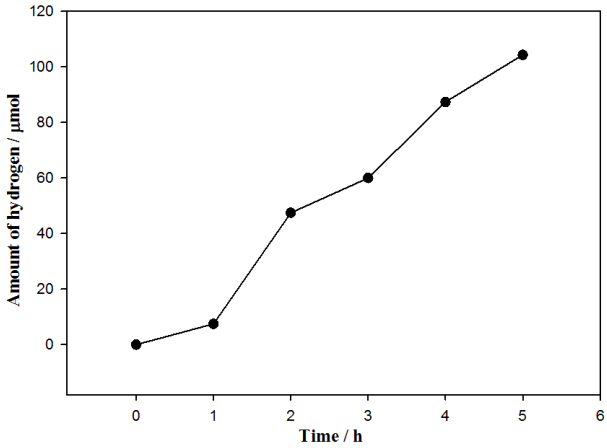

Figure 5.6 Time course of hydrogen evolution with CT. 45 mg of CT was dispersed in 300 mL Na_2S/Na_2SO_3 (0.01 mol) solution, and 1 wt% Pt was loaded as cocatalyst. High energy Xenon lamp equipped with 420 nm cut-off filter was used as the light source.

To explain the origin of significant photocatalytic hydrogen evolution activity enhancement of CT compared to that of pure NCs, photoluminescence (PL) analysis was performed. As shown in Figure 5.7a, CdTe@CdS NCs exhibited a PL peak at around 610 nm, which is close to previous reports based on the size of CdTe NCs.[28, 40] However, CT showed significantly weakened PL signal and nearly complete quenched peak (Figure 5.7b). The huge change in the PL intensity indicated that the electron-hole recombination was vastly suppressed in CT.

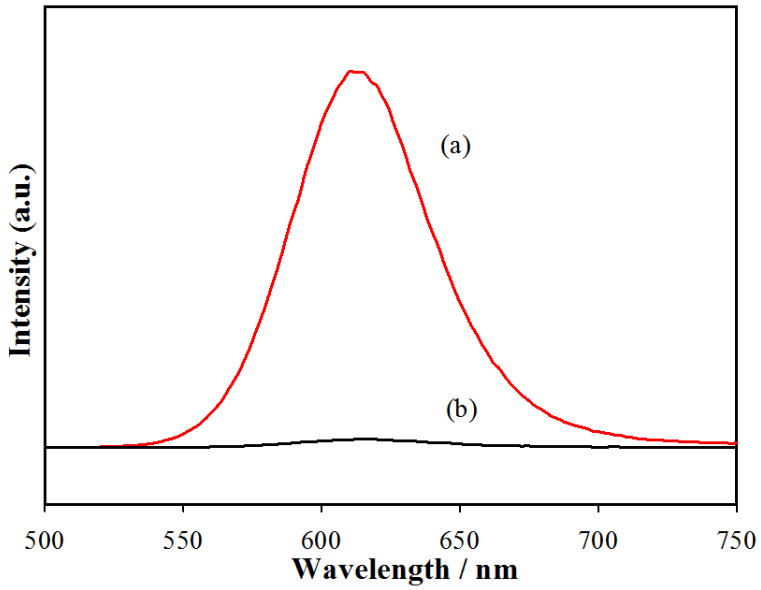

Figure 5.7 PL spectra of (a) CdTe@CdS NCs and (b) CT. Excitation wavelength: 420 nm.

Even though CdTe NCs have been used as the visible light absorber in the process of photocatalytic hydrogen production,[15, 21] we only detected extremely small amount of H_2 product on the CdTe@CdS NCs alone. There are two possible reasons for this phenomenon. First, due to the very rapid charge recombination in the CdTe@CdS NCs, photoinduced electrons will be annihilated before diffusing to Pt particles and reducing protons. Second, photocorrosion of CdTe may happen. Previous studies showed that when Au was grown on CdTe nanostructure via photodeposition method using Au (III) as precursor, CdTe will be consumed and Te^{2-} be oxidized to Te^0.[41, 42] Earlier work showed that the S^{2-}/S_n^{2-} redox couple has a reduction potential of around -0.5 V (vs NHE), which is capable of capturing the photoinduced holes in the valence band of CdTe.[20, 43] Nevertheless, as the reaction of holes and S^{2-} is a rate-determining process, the self-corrosion of CdTe may dominate over the hole capture by S^{2-}.[20] Some researchers reported that S^{2-}/S_n^{2-} redox couple is not very efficient in terms of stabilizing CdTe in aqueous solution.[44, 45] So CdTe NCs may undergo decay not only during the

photodeposition process of Pt particles, but also in the following photocatalytic reaction process. However, Sheng et al. reported that in a CdTe@CdS core-shell structure, due to much lower oxidation potential of the CdS shell than the CdTe core, the photooxidative degradation can be reduced.[19] To rule out the possibility that the poor photocatalytic performance of CdTe@CdS NCs was due to an improper sacrificial agent, we also tested hydrogen production with ascorbic acid (H_2A) as the sacrificial agent. Even though H_2A has been shown to be quite effective in CdTe-based systems,[15, 21] we still could only obtain similar small amount of hydrogen product (not shown). Therefore, the rapid charge recombination may be the dominant factor which limited the photocatalytic hydrogen production capability of the pure CdTe@CdS NCs.

Despite the very low activity of pure CdTe@CdS NCs, CT has dramatically improved hydrogen production capability even though the ratio of CdTe@CdS NCs in CT is very low. Jasieniak et al. conducted a systematically study on the size dependence of the conduction band and valence band positions of several nanocrystals including CdTe, CdSe, PbS etc., and the relationship between the band position and the size of CdTe NCs can be described in Eq. 5.2 and 5.3.[46] Based on the size of our CdTe NCs and Eq. 5.2 and 5.3, the CB and VB edge are located at -2.35 eV and -4.99 eV, respectively, with reference to E_{vac}. After converting to the redox potential with reference to NHE, the CB and VB edge are -2.15 V and 0.49 V, respectively. So the conduction band edge of our CdTe NCs is well above those of CdS and titania.[47, 48] Scheme 5.2 shows the energy alignment in CT. The proper energy band configuration in CT facilitates the electron flow in the direction of CdTe-> CdS-> $Ti_{0.91}O_2$, and therefore electrons can be effectively separated from holes. Therefore, the significantly suppressed charge recombination is a result of the charge transfer between CdTe@CdS NCs and $Ti_{0.91}O_2$ NSs. Moreover, as CdTe is a p-type semiconductor while CdS and titania are n-type semiconductors, p-n nanojunctions will form at the interface. The Fermi level alignment near the p-n junction interface results in the upward and downward shifts of the energy bands of CdTe and CdS, respectively.[19] The interfacial electric field induced by the p-n nanojunction can further promote the electron flow from CdTe to CdS. Therefore, the configuration of our semiconductor composite greatly facilitates the charge separation and thus the photocatalytic hydrogen production.

$$E_{cb} = -3.29 + 4.19 \times D^{-1.21} \quad \text{(Eq. 5.2)}$$

$$E_{vb} = -4.74 - 0.80 \times D^{-0.97} \quad \text{(Eq. 5.3)}$$

Where the E_{cb} (eV) and E_{vb} (eV) are the conduction band edge and valence band edge with reference to the vacuum energy (E_{vac}), respectively, and D (nm) is the diameter of the CdTe NCs.

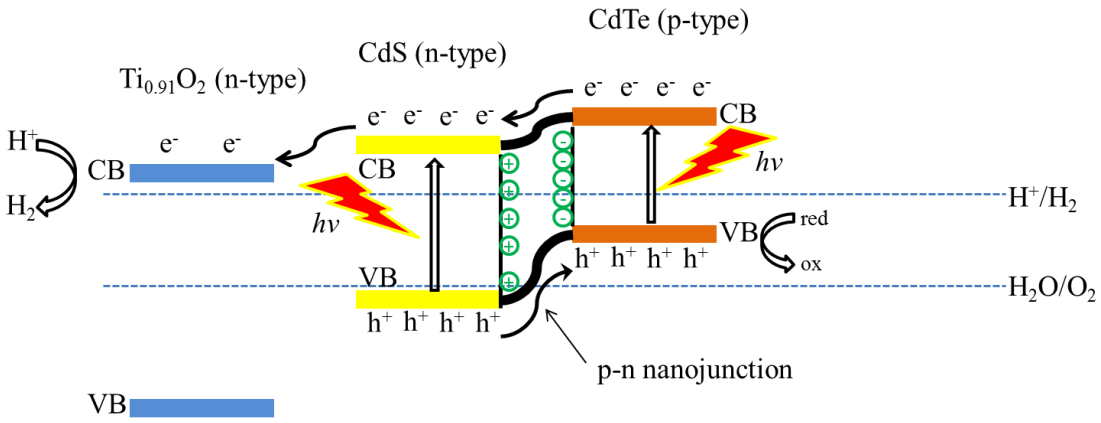

Scheme 5.2 Schematic of the energy alignment in the CT.

To determine whether CT was photocorroded after the reaction, we collected CT after test and performed XPS again. The XPS spectrum of Te 3d showed identical position to that of fresh CT (Figure S5.2, ESI†), and no peaks of Te 3d in metallic state showed up. This indicates that CT remained relatively stable in the photocatalytic reaction process.

5.4 Conclusions

In summary, a nanohybrid composed of CdTe@CdS nanocrystals and titania nanosheets with layered structure was synthesized and used for photocatalytic H_2 production under visible light. Despite the fact that neither pure CdTe@CdS NCs nor pure titania nanosheets were efficient photocatalyst for hydrogen production, the nanohybrid of the two showed very impressive hydrogen production capability. The improved photocatalytic performance can be attributed to two factors: the excellent visible light absorption introduced by the incorporation of CdTe@CdS NCs and the greatly enhanced charge recombination due to the proper energy band alignment and the formation of p-n nanojunctions. The finding demonstrates the great importance of the dual functions of CdTe@CdS NCs, i.e., visible light absorber and p-n nanojunction. More important, this concept can be extended to other nanocrystals (either single component or core-shell structured) and nanosheets (metal oxide nanosheets, layered double hydroxides, polymer semiconductor nanosheets like C_3N_4, etc.), which holds promise for synthesizing highly efficient photocatalyst for producing H_2 fuel from solar energy.

5.5 References

1. G. C. Xie, K. Zhang, B. D. Guo, Q. Liu, L. Fang and J. R. Gong, *Adv. Mater.*, 2013, **25**, 3820-3839.

2. G. Liu, L. Wang, H. G. Yang, H. M. Cheng and G. Q. M. Lu, *J. Mater. Chem.*, 2009, **20**, 831-843.

3. X. Chen and S. S. Mao, *Chem. Rev.*, 2007, **107**, 2891-2959.

4. X. Chen, S. Shen, L. Guo and S. S. Mao, *Chem. Rev.*, 2010, **110**, 6503-6570.

5. Y. Q. Qu and X. F. Duan, *Chem. Soc. Rev.*, 2013, **42**, 2568-2580.

6. J. L. Gunjakar, I. Y. Kim, J. M. Lee, Y. K. Jo and S. J. Hwang, *J. Phys. Chem. C*, 2014, **118**, 3847-3863.

7. M. Osada and T. Sasaki, *Adv. Mater.*, 2012, **24**, 210-228.

8. R. Z. Ma and T. Sasaki, *Adv. Mater.*, 2010, **22**, 5082-5104.

9. T. W. Kim, S. G. Hur, S. J. Hwang and J. H. Choy, *Chem. Commun.*, 2006, 220-222.

10. J. L. Gunjakar, T. W. Kim, H. N. Kim, I. Y. Kim and S. J. Hwang, *J. Am. Chem. Soc.*, 2011, **133**, 14998-15007.

11. T. W. Kim, S. G. Hur, S. J. Hwang, H. Park, W. Choi and J. H. Choy, *Adv. Funct. Mater.*, 2007, **17**, 307-314.

12. S. I. Shin, A. Go, I. Y. Kim, J. M. Lee, Y. Lee and S. J. Hwang, *Energy Environ. Sci.*, 2013, **6**, 608-617.

13. Y. Bai, Z. Xing, H. Yu, Z. Li, R. Amal and L. Wang, *ACS Appl. Mater. Interfaces*, 2013, **5**, 12058-12065.

14. Z. Han, F. Qiu, R. Eisenberg, P. L. Holland and T. D. Krauss, *Science*, 2012, **338**, 1321-1324.

15. F. Wang, W. G. Wang, X. J. Wang, H. Y. Wang, C. H. Tung and L. Z. Wu, *Angew. Chem., Int. Ed.*, 2011, **50**, 3193-3197.

16. M. A. Holmes, T. K. Townsend and F. E. Osterloh, *Chem. Commun.*, 2011, **48**, 371-373.

17. X. Michalet, F. F. Pinaud, L. A. Bentolila, J. M. Tsay, S. Doose, J. J. Li, G. Sundaresan, A. M. Wu, S. S. Gambhir and S. Weiss, *Science*, 2005, **307**, 538-544.

18. I. L. Radtchenko, G. B. Sukhorukov, N. Gaponik, A. Kornowski, A. L. Rogach and H. Möhwald, *Adv. Mater.*, 2001, **13**, 1684-1687.

19. P. Sheng, W. Li, J. Cai, X. Wang, X. Tong, Q. Cai and C. A. Grimes, *J. Mater. Chem. A*, 2013, **1**, 7806-7815.

20. J. H. Bang and P. V. Kamat, *ACS nano*, 2009, **3**, 1467-1476.

21. Z. J. Li, X. B. Li, J. J. Wang, S. Yu, C. B. Li, C. H. Tung and L. Z. Wu, *Energy Environ. Sci.*, 2013, **6**, 465-469.

22. J. Wang, I. Mora-Seró, Z. Pan, K. Zhao, H. Zhang, Y. Feng, G. Yang, X. Zhong and J. Bisquert, *J. Am. Chem. Soc.*, 2013, **135**, 15913-15922.

23. X. Peng, M. C. Schlamp, A. V. Kadavanich and A. Alivisatos, *J. Am. Chem. Soc.*, 1997, **119**, 7019-7029.

24. D. Hou, X. Hu, P. Hu, W. Zhang, M. Zhang and Y. Huang, *Nanoscale*, 2013, **5**, 9764-9772.

25. L. Yang, S. Luo, Y. Li, Y. Xiao, Q. Kang and Q. Cai, *Environ. Sci. Technol.*, 2010, **44**, 7641-7646.

26. M. Long, W. M. Cai, J. Cai, B. X. Zhou, X. Y. Chai and Y. H. Wu, *J. Phys. Chem. B*, 2006, **110**, 20211-20216.

27. F. Meng, J. Li, S. K. Cushing, M. Zhi and N. Wu, *J. Am. Chem. Soc.*, 2013, **135**, 10286-10289.

28. Y. Zhu, Z. Li, M. Chen, H. M. Cooper, G. Q. Lu and Z. P. Xu, *J. Colloid Interface Sci.*, 2013, **390**, 3-10.

29. G. Liu, L. Wang, C. Sun, Z. Chen, X. Yan, L. Cheng, H. M. Cheng and G. Q. M. Lu, *Chem. Commun.*, 2009, 1383-1385.

30. Z. T. Deng, O. Schulz, S. Lin, B. Q. Ding, X. W. Liu, X. X. Wei, R. Ros, H. Yan and Y. Liu, *J. Am. Chem. Soc.*, 2010, **132**, 5592-5593.

31. T. W. Kim, I. Y. Kim, T. S. Jung, C. H. Ko and S. J. Hwang, *Adv. Funct. Mater.*, 2013, **23**, 4377-4385.

32. J. L. Gunjakar, T. W. Kim, I. Y. Kim, J. M. Lee and S. J. Hwang, *Sci. Rep.*, 2013, **3**.

33. G. Liu, C. H. Sun, L. Z. Wang, S. C. Smith, G. Q. Lu and H. M. Cheng, *J. Mater. Chem.*, 2011, **21**, 14672-14679.

34. Y. Ebina, T. Sasaki, M. Harada and M. Watanabe, *Chem. Mater.*, 2002, **14**, 4390-4395.

35. W. W. Yu, L. Qu, W. Guo and X. Peng, *Chem. Mater.*, 2003, **15**, 2854-2860.

36. H. Zhang and B. Yang, *Thin Solid Films*, 2002, **418**, 169-174.

37. H. Zhang, Z. Zhou, B. Yang and M. Gao, *J. Phys. Chem. B*, 2003, **107**, 8-13.

38. X. X. Yan, G. Liu, L. Z. Wang, Y. Wang, X. F. Zhu, J. Zou and G. Q. Lu, *J. Mater. Res.*, 2010, **25**, 182-188.

39. L. Wu, J. C. Yu and X. Z. Fu, *J. Mol. Catal. A-Chem.*, 2006, **244**, 25-32.

40. Z. Deng, O. Schulz, S. Lin, B. Ding, X. Liu, X. Wei, R. Ros, H. Yan and Y. Liu, *Journal of the American Chemical Society*, 2010, **132**, 5592-5593.

41. Y. Khalavka and C. Sönnichsen, *Adv. Mater.*, 2008, **20**, 588-591.

42. L. Carbone, S. Kudera, C. Giannini, G. Ciccarella, R. Cingolani, P. D. Cozzoli and L. Manna, *J. Mater. Chem.*, 2006, **16**, 3952-3956.

43. A. B. Ellis, S. W. Kaiser, J. M. Bolts and M. S. Wrighton, *J. Am. Chem. Soc.*, 1977, **99**, 2839-2848.

44. A. B. Ellis, S. W. Kaiser and M. S. Wrighton, *J. Am. Chem. Soc.*, 1976, **98**, 6418-6420.

45. P. M. Lessner, F. R. McLarnon, J. Winnick and E. J. Cairns, *J. Electrochem. Soc.*, 1993, **140**, 1847-1849.

46. J. Jasieniak, M. Califano and S. E. Watkins, *ACS nano*, 2011, **5**, 5888-5902.

47. C. G. Van de Walle and J. Neugebauer, *Nature*, 2003, **423**, 626-628.

48. A. Kudo and Y. Miseki, *Chem. Soc. Rev.*, 2008, **38**, 253-278.

5.6 Supporting information

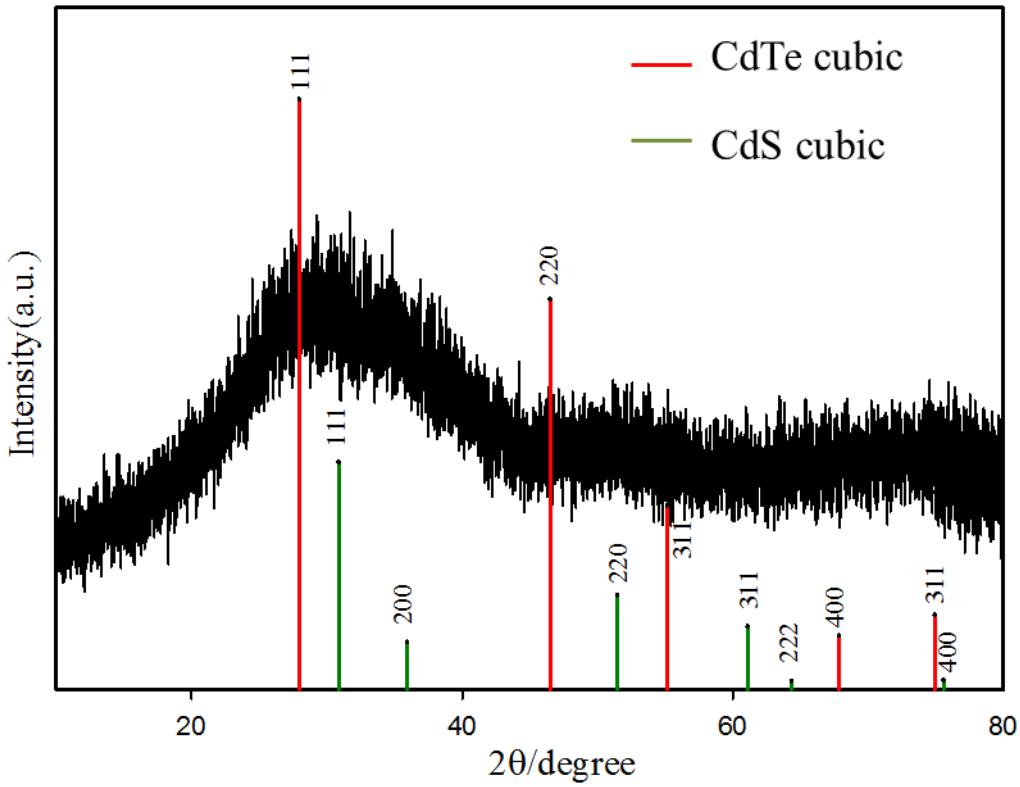

Figure S5.1 XRD pattern of pure CdTe@CdS NCs.

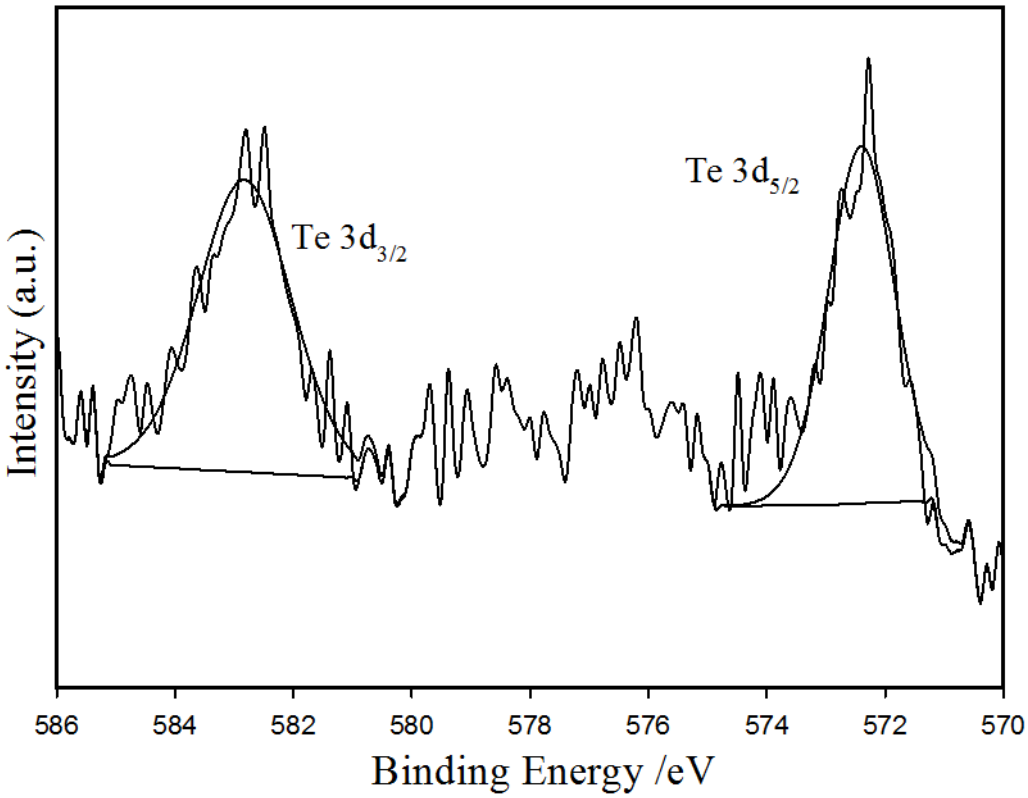

Figure S5.2 XPS spectrum of Te 3d of CT after photocatalytic reaction.

6. A novel carbon nitride-based polymer composite for enhanced photocatalytic hydrogen production

A novel carbon nitride-based polymer composite for enhanced photocatalytic hydrogen production

Zheng Xing, Zhigang Chen, Xu Zong* and Lianzhou Wang*

Chem. Commun., 2014, 50,6762-6764

6.1 Abstract

A new type of graphitic C_3N_4-based composite photocatalysts were prepared by co-loading PEDOT as hole transport pathway and Pt as electron trap on C_3N_4. The as-prepared C_3N_4-PEDOT-Pt composites showed drastically enhanced activity for visible light-driven photocatalytic H_2 production compared to those of C_3N_4-PEDOT and C_3N_4-Pt possibly due to the spatial separation of the reduction and oxidation reaction sites.

6.2 Introduction

Photocatalytic hydrogen evolution using semiconductor materials provides a promising way to produce clean hydrogen fuel.[1] However, a significant factor limiting the overall photocatalytic efficiency is the rapid charge recombination after photo-excitation, which often happens during the diffusion of charges in the bulk as well as on the photocatalyst particle surface.[2, 3] In order to suppress the charge recombination, one effective solution is to design photocatalysts with spatially separated oxidative and reductive sites. For example, Kudo and co-workers prepared a NiO-loaded $NaTaO_3$ doped with lanthanum[4]. The Lanthanum doping induced the formation of nanostep structure on the surface of $NaTaO_3$ and H_2 evolution occurred on the NiO particles while O_2 evolution took place at the groove of the nanostep structure. Therefore, this type of catalysts exhibited high efficiency for overall water splitting into H_2 and O_2 under UV illumination due to the separation of the reduction and oxidation sites. Li et al. developed a dual cocatalyst system by loading Pt and PdS on CdS as the reduction and oxidation cocatalysts, respectively, and achieved impressively high quantum efficiency for hydrogen production.[5, 6] Recently, Li and co-workers found that the (010) and (110) facets of the $BiVO_4$ crystals are reductive and oxidative, respectively.[7, 8] Based on this finding, the selectively deposited reduction and oxidation catalysts on different facets led to much improved oxygen production upon visible light irradiation compared to $BiVO_4$ with randomly distributed cocatalyst. In this regard, the spatial separation of charge carriers in photocatalyst is significantly important for the photocatalytic efficiency.

Since the pioneer work on using graphitic carbon nitride (g-C_3N_4) for photocatalytic water splitting reported by Wang et al.[9], g-C_3N_4, a polymer semiconductor has drawn great attention as a promising photocatalyst due to its visible light absorption, suitable band position for both H_2 and O_2 production, and relatively good thermal and chemical stability.[10] However, the photocatalytic activities of pure g-C_3N_4 are still limited due to the serious charge recombination, and much effort has been devoted to addressing this issue.[11-16]

Poly (3, 4-ethylenedioxythiophene) (PEDOT) has been recognised to be an excellent conducting polymer in optoelectronic devices because PEDOT possesses excellent conductivities, thermal stability, transparency in the visible range and the ability to be processed in aqueous solution.[17, 18] For instance, as a result of its high hole mobility, PEDOT is often exploited as hole conductor in Dye Sensitized Solar Cells (DSSCs).[18, 19] Moreover, PEDOT has been used to not only conduct holes but also catalyse water oxidation reaction in the configuration of photoelectrochemical cells.[20] Considering the aforementioned outstanding electrical, chemical, catalytic and optical properties of PEDOT, we wondered whether it was possible to construct a C_3N_4-PEDOT composite and use PEDOT as a hole transport pathway. Furthermore, as Pt particles are often deposited onto g-C_3N_4 as proton reduction sites, we may create a C_3N_4-PEDOT-Pt system, in which PEDOT and Pt act as oxidation and reduction reaction sites, respectively. Herein, we report a new type of C_3N_4 composite photocatalyst by co-loading PEDOT and Pt cocatalysts on C_3N_4. The as-prepared C_3N_4-PEDOT-Pt photocatalyst produced 4 times more hydrogen than conventional C_3N_4-Pt photocatalyst under optimised conditions. The speculated spatial separation of the reductive and oxidative reaction sites on C_3N_4 can efficiently suppress the recombination of photogenerated electrons and holes and was supposed to be the main reason for the drastically enhanced photocatalytic performance.

6.3 Results and Discussion

The C_3N_4-PEDOT-Pt composites were prepared by co-loading PEDOT and Pt particles on g-C_3N_4 using a two-step method (Scheme 6.1, see ESI† for experimental details). Commercially available poly(3,4-ethylenedioxythiophene):poly(styrenesulfonate) (PEDOT-PSS) complex was used, in which the PSS has dual functions of acting as the counterion of the positively charged PEDOT and rendering the dispersibility in aqueous medium.[21] In the first step, different amounts of PEDOT-PSS were loaded on g-C_3N_4 by impregnating g-C_3N_4 in commercial PEDOT-PSS solution. As PEDOT-PSS is soluble in water, the

resulting C_3N_4-PEDOT composite was post-treated with ethylene glycol (EG) to avoid the detachment of the PEDOT in aqueous solution.[22] Moreover, treatment with EG can improve the conductivity and stability of PEDOT.[17, 22] In the second step, Pt nanoparticles were loaded on the C_3N_4-PEDOT composite powder via an in-situ photoreduction method in the presence of a hole scavenger.

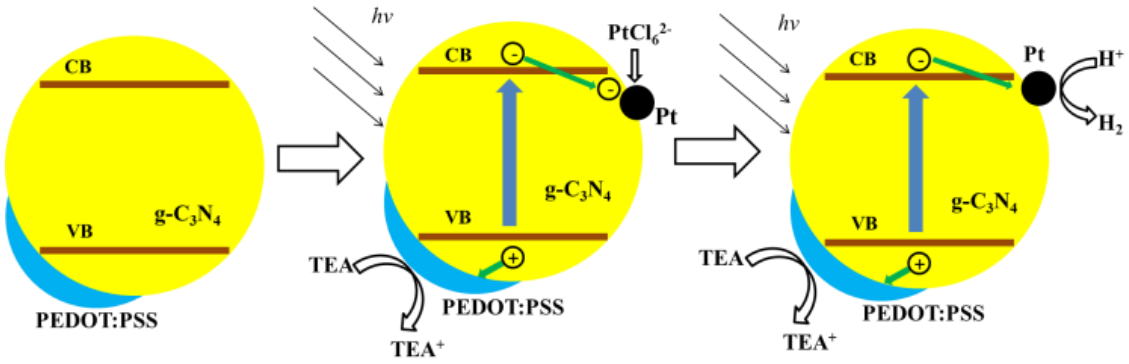

Scheme 6.1 Schematic of the preparation process of the C_3N_4-PEDOT-Pt composite and the proposed mechanism of the photocatalytic reaction.

The X-ray diffraction (XRD) pattern of as-prepared g-C_3N_4 (Figure S6.1a, ESI†) shows two peaks: a low-angle (100) peak at around 15.3° corresponding to the tri-s-triazine units packing in the lattice planes parallel to the c-axis, and a (002) peak at around 32.1° stemmed from the periodic stacking of individual layers.[11, 16] XRD patterns of C_3N_4-PEDOT composites with different ratios of PEDOT are very similar to that of g-C_3N_4, indicating that the addition of PEDOT made insignificant change to the crystal structure of g-C_3N_4 (Figure S6.1b-e, ESI†). The optical absorption properties of all samples were then examined by UV-visible spectroscopy. The g-C_3N_4 has an absorption edge at 466 nm, corresponding to a band gap of 2.66 eV (Figure S6.2a, ESI†). After the impregnation of PEDOT, the absorption edge of g-C_3N_4 remained nearly unchanged while the baseline was elevated (Figure S6.2b-e, ESI†). This phenomenon reveals that PEDOT did not change the electronic structure of g-C_3N_4. The rise of absorption baseline by PEDOT is reflected by the gradual colour change of C_3N_4-PEDOT from yellow (pure g-C_3N_4) to dark green (C_3N_4-5 wt% PEDOT) with the increase of the ratios of PEDOT.

The morphology of C_3N_4-PEDOT composite was investigated with transmission electron microscopy (TEM). The g-C_3N_4 possessed a layered structure (Figure 6.1a and Figure S6.3). To confirm the presence of PEDOT in the polymer composite and determine the

distribution of PEDOT, element mapping analysis was conducted. As shown in Figure 6.1b-e, all C, N, O and S elements are evenly distributed at the surface of C_3N_4-5 wt% PEDOT. S elements only come from the C-S-C in the PEDOT and sulfonic acid or sulfonate functional groups in the PSS, while O elements only come from sulfonic acid or sulfonate functional groups in the PSS. The distribution of S and O elements indicates that the surface of g-C_3N_4 was relatively uniformly covered by the PEDOT-PSS polymer.

To further confirm the existence of PEDOT on C_3N_4, X-ray photoelectron spectroscopy (XPS) analysis was performed. Similar results in the XPS spectra of S 2p of all C_3N_4-PEDOT samples were observed (Figure S6.4, ESI†). The lower binding energy peaks at 163.5 eV and 164.7 eV can be assigned to sulphur atoms in PEDOT while the higher binding energy peak at 168.8 eV corresponds to S atoms in PSS.[23] Moreover, the ratio of PEDOT to PSS is estimated to be around 1:3 based on the measured area ratio of PEDOT to PSS in the S 2p spectra, which is in good agreement with previous reports .[23, 24]

We then investigated the photocatalytic H_2 evolution performance of the composites. Figure 6.2A shows the H_2 evolution rates of all samples under visible light illumination. When loaded with Pt, pure g-C_3N_4 (Figure 6.2A-a) can only produce H_2 at a rate of 6.4 μmol h^{-1} in the first 4 h. With the increase of the amount of PEDOT, the hydrogen production rate steadily rose, reaching a maximum at 2 wt% loading. C_3N_4-2 wt% PEDOT (Figure 6.2A-d) showed a hydrogen evolution rate of 32.7 μmol h^{-1}, which was over 4 times higher than that of g-C_3N_4. However, when the loading was increased to to 5 wt%, the activity decreased (Figure 6.2A-e). All the C_3N_4-PEDOT-Pt composites exhibited much improved H_2 evolution compared to g-C_3N_4-Pt in aqueous triethanolamine (TEA) solution. In a control experiment, we also tested the H_2 evolution on C_3N_4 without Pt, and only negligible amount of H_2 was detected when using C_3N_4-2 wt% PEDOT (Figure 6.2A-f). The results indicate that PEDOT cannot work as the reduction reaction site like Pt. Moreover, PEDOT by itself was not able to produce any H_2 in TEA solution regardless of the presence of Pt (not shown in the Figure 6.2). This indicates that PEDOT cannot act as the light absorber to induce photocatalytic H_2 production.

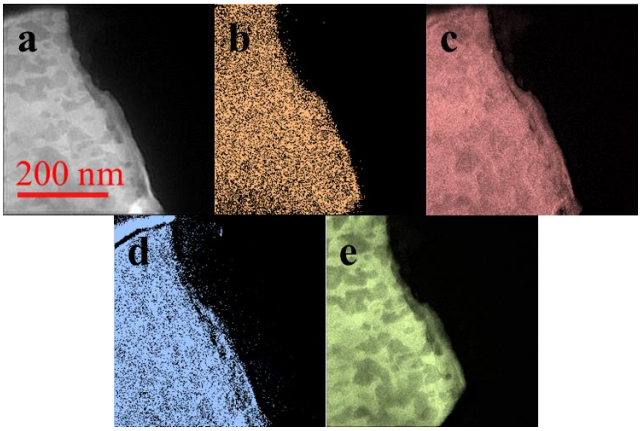

Figure 6.1 TEM image of C_3N_4-5 wt% PEDOT (a) and elemental maps of C (b), N (c), O (d) and S (e).

In order to investigate the origin of the difference of the photocatalytic performance and the role of PEDOT, photoluminescence (PL) analysis was performed. Figure 6.3 shows the PL spectra of g-C_3N_4 and PEDOT-C_3N_4 composites. The broad peaks at around 460 nm are related to the electron-hole recombination in g-C_3N_4,[13, 16] and the peak position agrees well with the band gap (2.66 eV) of g-C_3N_4. When the PEDOT loading was increased, the PL peak became gradually quenched. The weakened PL signals with the increased PEDOT loading implied a decreased electron-hole recombination, which led to the improved H_2 evolution. Theoretically, as PEDOT is a hole conductor, photogenerated electrons will not transfer from g-C_3N_4 to PEDOT and therefore Pt cannot form on the PEDOT surface. Instead, $PtCl_6^{2-}$ ions can only be reduced to Pt on the bare surface of g-C_3N_4 where PEDOT is not present (Scheme 6.1). Therefore, reduction (Pt) and oxidation (PEDOT) reaction sites should be spatially separated on the surface of g-C_3N_4 through the present two-step method. Such a structure will facilitate charge separation and is supposed to lead to enhanced photocatalytic performance. This is further confirmed by the further quenching of PL signal upon photodeposion of Pt on C_3N_4-PEDOT (Figure 6.3B). It is worth noting that even though C_3N_4-5 wt% PEDOT has the weakest PL peak, when loaded with Pt it produced less H_2 than C_3N_4-2 wt% PEDOT- 1 wt% Pt and C_3N_4-1 wt% PEDOT- 1 wt% Pt. We believe that when the PEDOT loading was too high, the available surface sites for $PtCl_6^{2-}$ reduction were limited, and so the lessened Pt sites led to drop in hydrogen production. We tentatively used TEM to acquire the direct evidence on the spatial separation of the reduction (Pt) and oxidation (PEDOT) reaction sites on C_3N_4 but no desirable results were obtained due to the low contrast between PEDOT and C_3N_4. However, from the synthesis process shown in Scheme 6.1, the as-designed spatial

separation of Pt and PEDOT should be achieved, which is the supposed to be the main reason for the high photocatalytic activity of the composite.

To test the stability of C_3N_4-PEDOT in the aqueous reaction environment, a 12-hour cycle experiment was carried out with C_3N_4-2 wt% PEDOT. During the reaction, the reaction system was re-evacuated every 4 h and illumination was resumed after re-evacuation. As shown in Figure 6.2B, the activity was well maintained after 12 h and the catalyst can produce a total amount of 452.77 μmol of H_2. Moreover, it is noticed that the second and third cycles witnessed slightly increased H_2 evolution than the first cycle, possibly due to the photodeposition of Pt particles in the beginning of photocatalytic reaction. In previous reports about C_3N_4-polymer composites, H_2 evolution always suffered decay after prolonged reaction time possibly due to photocorrosion.[11, 12] The remarkably improved stability of our C_3N_4-PEDOT composites can be attributed to the stability of PEDOT and the intimate contact between PEDOT and g- C_3N_4.

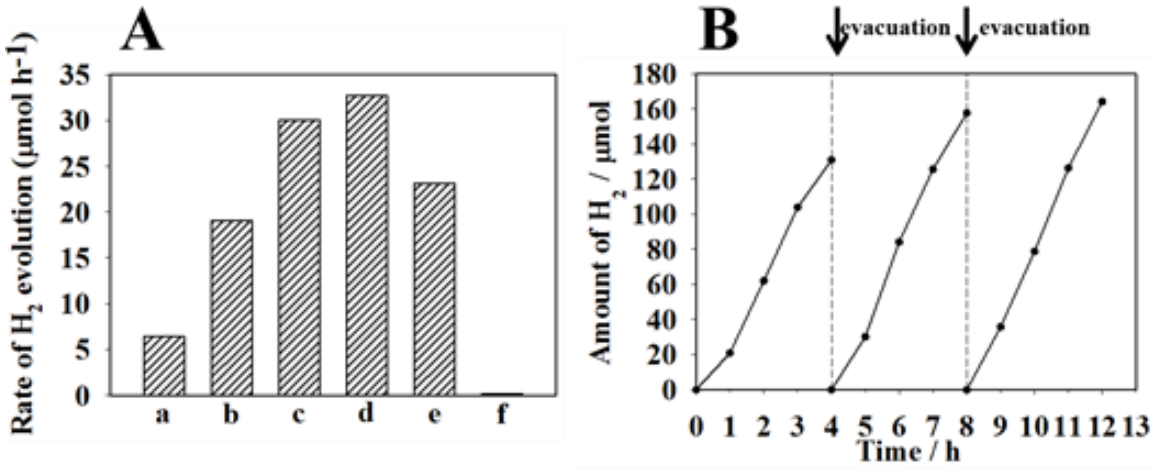

Figure 6.2 H_2 evolution performance on different samples. A: rates of photocatalytic H_2 evolution in the first 4 hours on (a) pure g-C_3N_4, C_3N_4-PEDOT with PEDOT loading of (b) 0.5 wt%, (c) 1 wt%, (d) 2 wt%, and (e) 5 wt% and (f) C_3N_4-2 wt% PEDOT without Pt. B: the time course of H_2 evolution in a 12-hour cycle experiment on C_3N_4-2 wt% PEDOT. In all experiments, 0.1 g of catalyst was loaded with 1 wt% Pt as the cocatalyst except (f) in A. 300 mL of triethanolamine (TEA) aqueous solution (10 vol%) was used as the reaction solution. High energy Xenon lamp equipped with 400 nm cut-off filter was used as the light source.

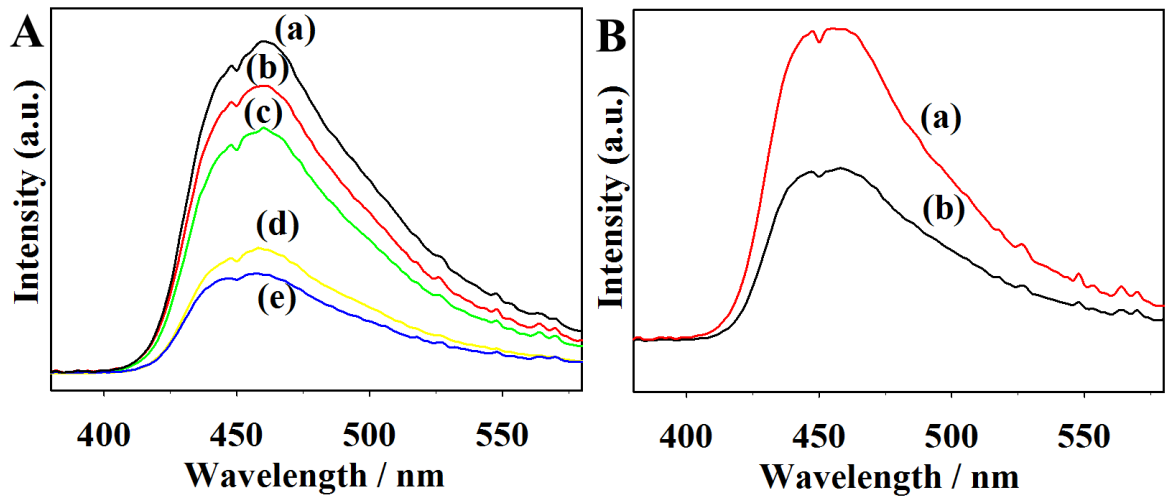

Figure 6.3 The PL spectra of pure g-C_3N_4 and C_3N_4-PEDOT composites. A: PL spectra of all samples before photocatalytic reaction: (a) pure g-C_3N_4, C_3N_4-PEDOT with PEDOT loading of (b) 0.5 wt%, (c) 1 wt%, (d) 2 wt% and (e) 5 wt%. B: PL spectra of C_3N_4-2 wt% PEDOT (a) before and (b) after photocatalysis reaction with photodeposited Pt particles.

6.4 Conclusions

In summary, we presented a new type of C_3N_4-based composite photocatalyst loaded with dual cocatalysts Pt and PEDOT. The as-prepared composites exhibited very stable and drastically enhanced photocatalytic hydrogen production compared to pure g-C_3N_4 under visible light illumination. The excellent performance of the composites can be attributed to the spatial separation of the reduction and oxidation reaction sites on C_3N_4. This finding demonstrates the important role of hole-conducting polymer for the generation of specially separated reductive and oxidative sites toward more efficient photocatalysis, and this concept could also be applied to other semiconductor-based photocatalyst systems.

6.5 References

1. A. Kudo and Y. Miseki, *Chem. Soc. Rev.*, 2008, **38**, 253-278.

2. G. Liu, L. Wang, H. G. Yang, H. M. Cheng and G. Q. M. Lu, *J. Mater. Chem.*, 2009, **20**, 831-843.

3. F. E. Osterloh, *Chem. Mat.*, 2007, **20**, 35-54.

4. H. Kato, K. Asakura and A. Kudo, *J. Am. Chem. Soc.*, 2003, **125**, 3082-3089.

5. J. Yang, H. Yan, X. Wang, F. Wen, Z. Wang, D. Fan, J. Shi and C. Li, *J. Catal.*, 2012, **290**, 151-157.

6. J. Yang, D. Wang, H. Han and C. Li, *Acc. Chem. Res.*, 2013, **46**, 1900-1909.

7. R. Li, F. Zhang, D. Wang, J. Yang, M. Li, J. Zhu, X. Zhou, H. Han and C. Li, *Nat. Commun.*, 2013, **4**, 1432.

8. R. Li, H. Han, F. Zhang, D. Wang and C. Li, *Energy Environ. Sci.*, 2014.

9. X. Wang, K. Maeda, A. Thomas, K. Takanabe, G. Xin, J. M. Carlsson, K. Domen and M. Antonietti, *Nat. Mater.*, 2009, **8**, 76-80.

10. Y. Wang, X. Wang and M. Antonietti, *Angew. Chem., Int. Ed.*, 2012, **51**, 68-89.

11. Y. Sui, J. Liu, Y. Zhang, X. Tian and W. Chen, *Nanoscale*, 2013, **5**, 9150-9155.

12. H. Yan and Y. Huang, *Chem. Commun.*, 2011, **47**, 4168-4170.

13. Y. Hou, Z. H. Wen, S. M. Cui, X. R. Guo and J. H. Chen, *Adv. Mater.*, 2013, **25**, 6291-6297.

14. D. H. Wang, Y. W. Zhang and W. Chen, *Chem. Commun.*, 2014, **50**, 1754-1756.

15. Y. B. Li, H. M. Zhang, P. R. Liu, D. Wang, Y. Li and H. J. Zhao, *Small*, 2013, **9**, 3336-3344.

16. P. Niu, L. L. Zhang, G. Liu and H. M. Cheng, *Adv. Funct. Mater.*, 2012, **22**, 4763-4770.

17. J. Ouyang, C. W. Chu, F. C. Chen, Q. Xu and Y. Yang, *Adv. Funct. Mater.*, 2005, **15**, 203-208.

18. A. J. Mozer, D. K. Panda, S. Gambhir, B. Winther-Jensen and G. G. Wallace, *J. Am. Chem. Soc.*, 2010, **132**, 9543-9545.

19. X. Liu, Y. Cheng, L. Wang, L. Cai and B. Liu, *Phys. Chem. Chem. Phys.*, 2012, **14**, 7098-7103.

20. X. Li, W. Lu, W. Dong, Q. Chen, D. Wu, W. Zhou and L. Chen, *Nanoscale*, 2013, **5**, 5257-5261.

21. S. Kirchmeyer and K. Reuter, *J. Mater. Chem.*, 2005, **15**, 2077-2088.

22. J. K. Lee, J. M. Cho, W. S. Shin, S. J. Moon, N. T. Kemp, H. Zhang and R. Lamb, *J. Korean Phys. Soc.*, 2008, **52**, 621-626.

23. J. Kim, J. Jung, D. Lee and J. Joo, *Synth. Met.*, 2002, **126**, 311-316.

24. G. Greczynski, T. Kugler and W. R. Salaneck, *Thin Solid Films*, 1999, **354**, 129-135.

6.6 Supporting information

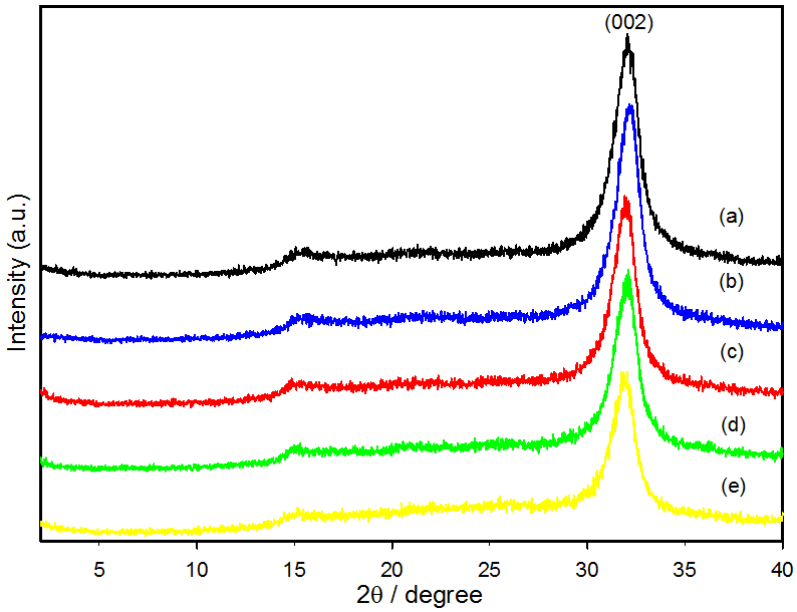

Figure S6.1 X-ray diffraction patterns of (a) pure C_3N_4, (b) C_3N_4-0.5%PEDOT, (c) C_3N_4-1%PEDOT, (d) C_3N_4-2%PEDOT and (e) C_3N_4-5%PEDOT.

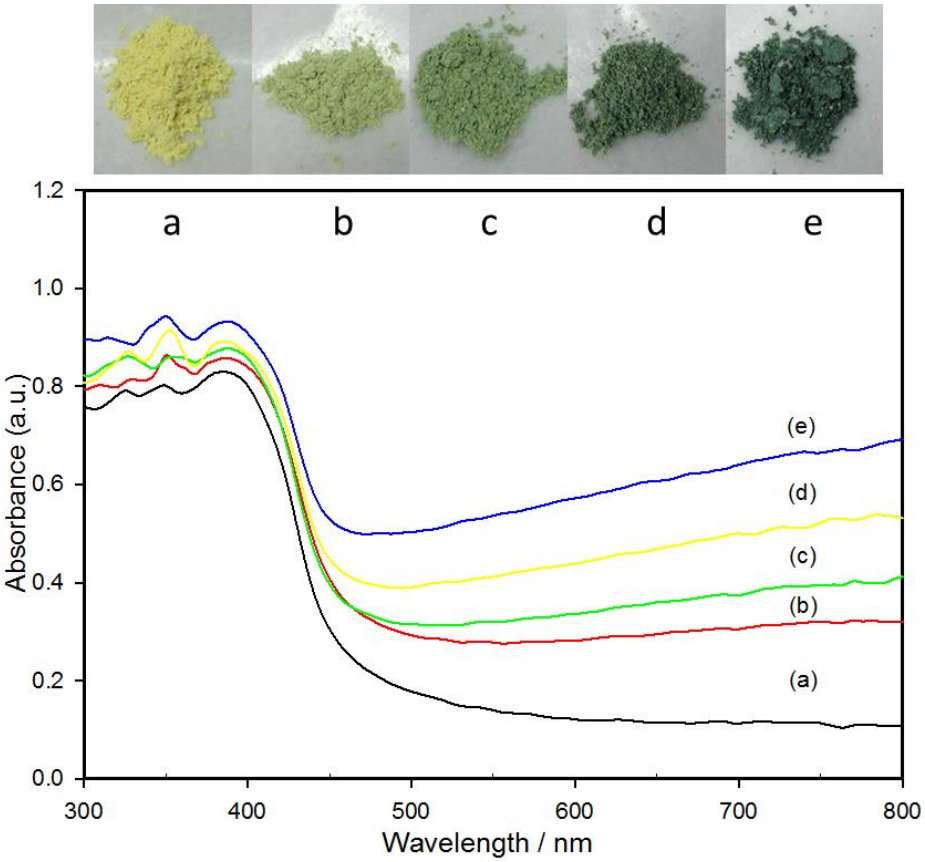

Figure S6.2 UV-visible absorption spectra of (a) pure C_3N_4, (b) C_3N_4-0.5%PEDOT, (c) C_3N_4-1%PEDOT, (d) C_3N_4-2%PEDOT and (e) C_3N_4-5%PEDOT. The photos of all samples above the spectra show the gradual colour changes when the amount of PEDOT is increased.

Figure S6.3 TEM image of C_3N_4-5%PEDOT.

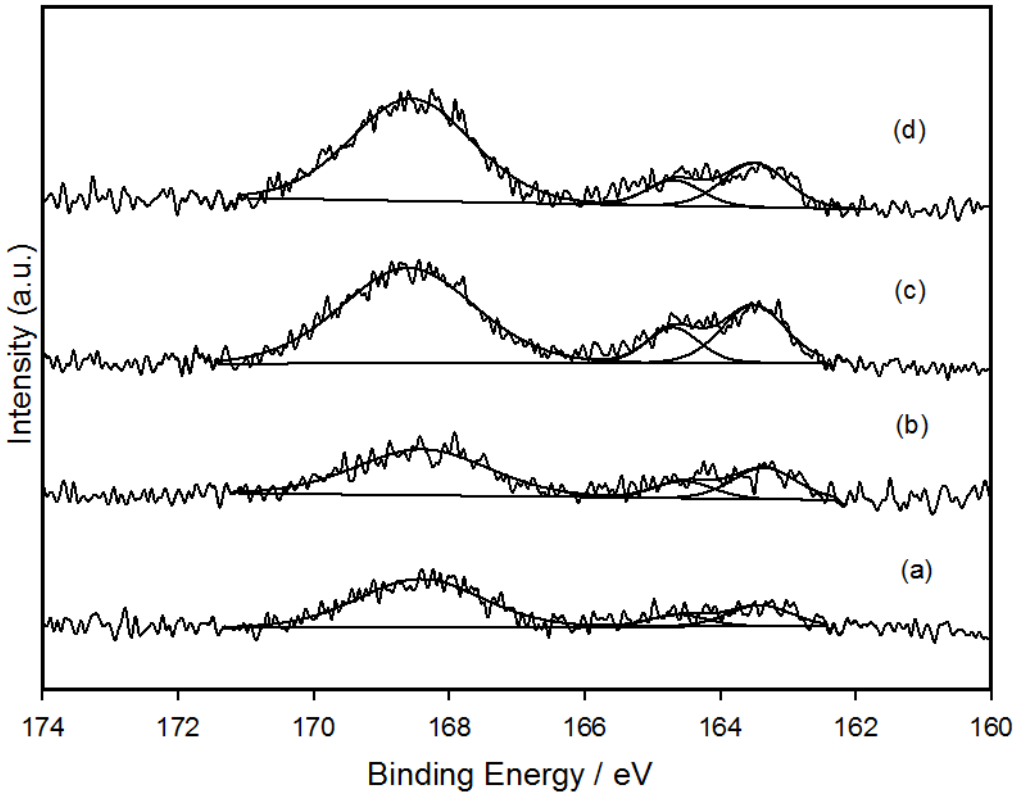

Figure S6.4 High-resolution XPS spectra for S 2p measured on (a) C_3N_4-0.5%PEDOT, (b) C_3N_4-1%PEDOT, (c) C_3N_4-2%PEDOT, and (d) C_3N_4-5%PEDOT.

7. Metal-free semiconducting carbon nitride nanosheets as building blocks for nanodevices

Metal-free semiconducting carbon nitride nanosheets as building blocks for nanodevices

Zheng Xing, Xu Zong, Bei Wang, and Lianzhou Wang*

Submitted to ***Adv. Mater.***

7.1 Abstract

Ultra-thin two-dimensional nanosheets are versatile building blocks for a variety of functional nanocomposites and nanodevices that have potential applications in photocatalysis, optoelectronic devices, etc. Herein we presented the fabrication of a semiconducting metal-free nanosheets device using phosphorus-doped carbon nitride (P-g-C_3N_4) nanosheets as the building block. The doping of P in g-C_3N_4 nanosheets not only extended the absorption of the nanosheets to the infrared region, more importantly endowed the nanosheets with highly negative-charged feature, which facilitated their even and stable dispersion in aqueous media. The as-prepared P-g-C_3N_4 nanosheets can be easily assembled with a layer-by-layer strategy to obtain nanodevices which resembled the first metal-free semiconducting nanosheet-based devices. Moreover, the P-doped g-C_3N_4 nanosheets demonstrated potential applications for solar energy conversion via water splitting under visible light irradiation. This work not only enriches the nanosheet galleries but also opens up new possibilities in fabricating metal-free nanosheet-based nanodevices for optoelectronic applications.

7.2 Introduction

The discovery of graphene, a single atomic layer “nanosheet (NS)” of carbon networks, has sparked enormous research interest thanks to its excellent physicochemical properties.[1-5] Along with graphene, a variety of inorganic NSs including metal oxide NSs,[6-8] layered double hydroxides (LDHs) NSs,[7, 9] metal dichalcogenides NSs,[9, 10] etc. have drawn great research interest since the term “nanosheet” was first defined by Sasaki et al. in 1996 when they successfully synthesized titanium oxide NSs via a soft chemistry exfoliation method.[11, 12] In particular, the charge-bearing metal oxide NSs can be assembled into different nanostructures through a variety of solution-based processing techniques, including Layer-by-Layer (LBL) deposition, Langmuir-Blodgett (LB) deposition, flocculation, etc.[6, 8, 13] The great variety of metal oxide NSs, unique properties associated with the NSs and the high controllability of the nanostructures constructed from the NSs open up possibilities for designing novel nanodevices or nanocomposites for

optoelectronic applications,[14-16] photocatalysis,[17-19] photolumiscence,[20, 21] etc. At present, metal-based nanosheets account for the most fraction of the nanosheets gallery. Developing metal-free nanosheets that are capable of fabricating nanodevices still represents a big challenge.

Graphitic carbon nitride (g-C_3N_4), a stable polymeric semiconductor, has been widely studied for photoconversion applications due to its proper energy band structure.[22-24] g-C_3N_4 possesses a similar lamellar structure as graphite, with N-bridged tri-s-triazine forming the planar layers.[23, 25] The synthesis of graphene via exfoliation of graphite inspires the exfoliation bulk g-C_3N_4 to form graphene-like carbon nitride NSs, which can potentially exhibit special electronic and optical properties. In order to synthesize g-C_3N_4 NSs, both bottom-up[26] and top-down[27-32] methods have been investigated, with top-down methods remaining to be the prevalent strategy. Through these methods, g-C_3N_4 NSs with various numbers of atomic layers can be obtained ranging from single atomic layer (ca. 0.3-0.4 nm) to several layers (1-3 nm).

Despite the fact that the aforementioned g-C_3N_4 NSs possess dramatically expanded surface area and altered energy band structures, the optical absorption edge is blue-shifted due to the quantum size effect.[27, 30, 32] The enlarged band gap will inevitably limit the visible light absorbance of g-C_3N_4 NSs. Moreover, there are still no reports on g-C_3N_4 NSs assembly for fabricating nanodevices, which is possibly due to the deficiency of these NSs as indicated in our following investigation. Herein, we reported P-doped g-C_3N_4 NSs synthesized by first doping bulk g-C_3N_4 via calcination and subsequent exfoliation process in water. P doping dramatically improved the visible light absorption, and led to a highly negative charge on the P-doped g-C_3N_4 NSs. The negative surface charge not only made the P-doped g-C_3N_4 NSs suspension in aqueous media very stable, but also enabled the LBL assembly of NSs to form nanodevices. Moreover, P-doped g-C_3N_4 NSs showed the capability of photocatalytic water splitting under visible light irradiation.

7.3 Results and discussion

P-doped g-C_3N_4 powder was prepared with a simple two-step approach as shown in Scheme 7.1. In the first step, g-C_3N_4 was prepared by calcining dicyandiamide at 550 °C for 4 h in air. The as-prepared g-C_3N_4 was then grounded with sodium hypophosphite monohydrate ($NaH_2PO_2 \cdot H_2O$) followed by heating under N_2 flow at 500 °C for 2 h to obtain P-doped C_3N_4 (P-C_3N_4) (see ESI† for experimental details). The crystal structures of P-C_3N_4 as well as that of the pristine g-C_3N_4 were investigated with X-ray diffraction pattern

(XRD). As shown in Figure 7.1, two peaks located at 15.3 ° and 32.1 ° were observed for both samples. The peak at around 15.3 ° corresponds to the (100) plane of g-C_3N_4, which is originated from the tri-s-triazine units packing in the lattice planes parallel to the c-axis. The peak at around 32.1 ° corresponds to the (002) plane, indicating the stacking of individual C-N layers.[33] The intensity of the XRD peaks of P-doped g-C_3N_4 decreased slightly (Figure 7.1b), indicating the decreased crystallinity of g-C_3N_4 upon P doping. Similar phenomena were observed in many samples containing foreign dopants.[34, 35] However, since the XRD patterns of both the doped and undoped samples were similar, it is reasonable to conclude that the original C-N structure remained almost intact after P doping.

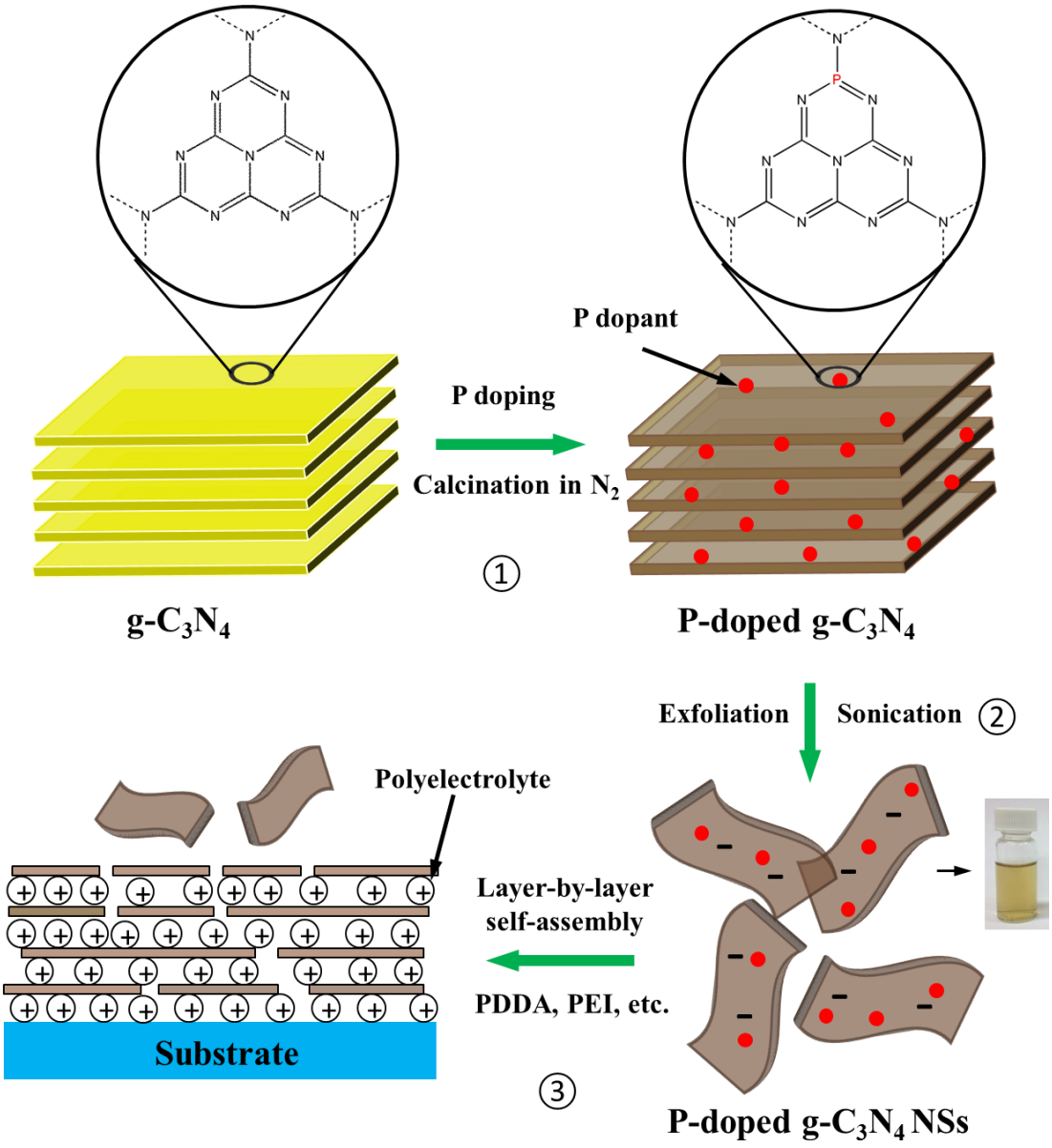

Scheme 7.1 Schematics of the fabrication of P-C_3N_4 NSs device with LBL strategy.

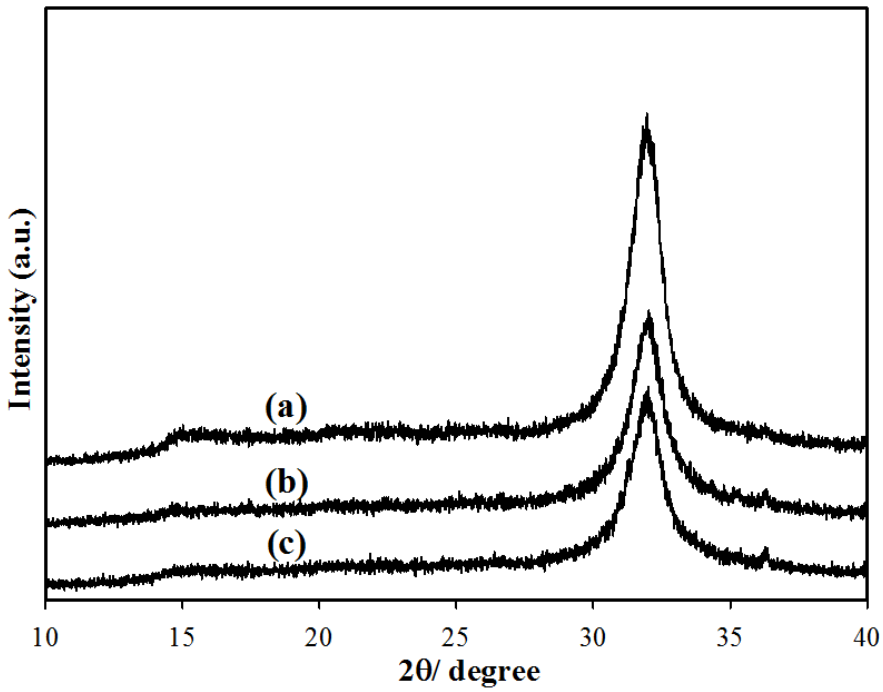

Figure 7.1 XRD patterns of (a) (a) g-C_3N_4, (b) P-doped g-C_3N_4 and (c) g-C_3N_4 calcined with Na_3PO_4.

To confirm the existence of P in the C-N network and investigate the chemical state of P dopant, X-ray photoelectron spectroscopy (XPS) analysis was conducted on P-C_3N_4. As shown in Figure 7.2, the P 2p peak is centred at ca. 133.3 eV, which is very close to that of P-N bond reported in P-doped g-C_3N_4.[36, 37] Therefore, P dopant most likely replaces the corner or bay carbon, forming P-N bonding in the doped C-N framework.[36] Based on the measured area of different elements in the XPS analysis, the atomic ratio of P is roughly estimated to be ca. 2.4%. The distribution of P dopants in P-doped g-C_3N_4 was investigated with element mapping analysis under TEM. As shown in Figure 7.3, the P-doped g-C_3N_4 possessed a typical layered structure (Figure 7.3a), with C, N and P elements evenly distributed throughout the particle (Figure 7.3b-c).

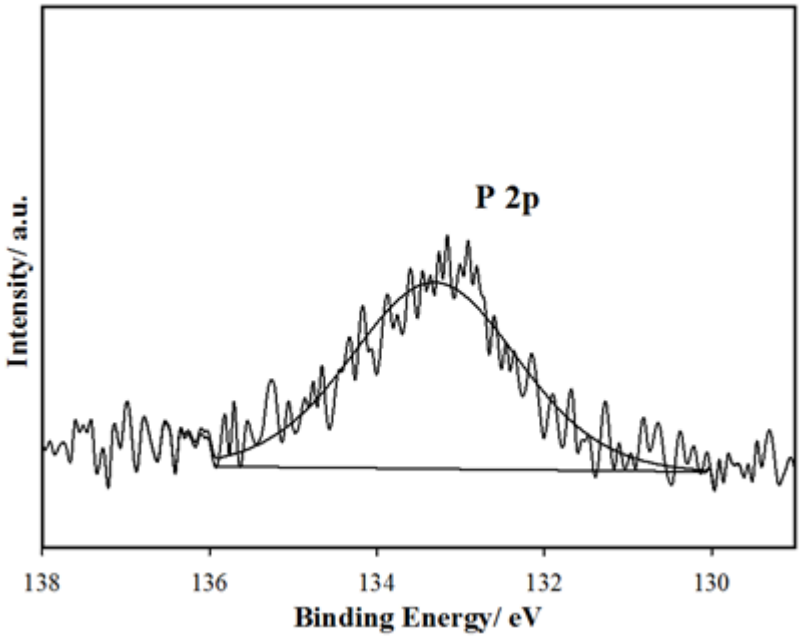

Figure 7.2 High-resolution XPS spectra for P 2p measured on P-doped g-C_3N_4.

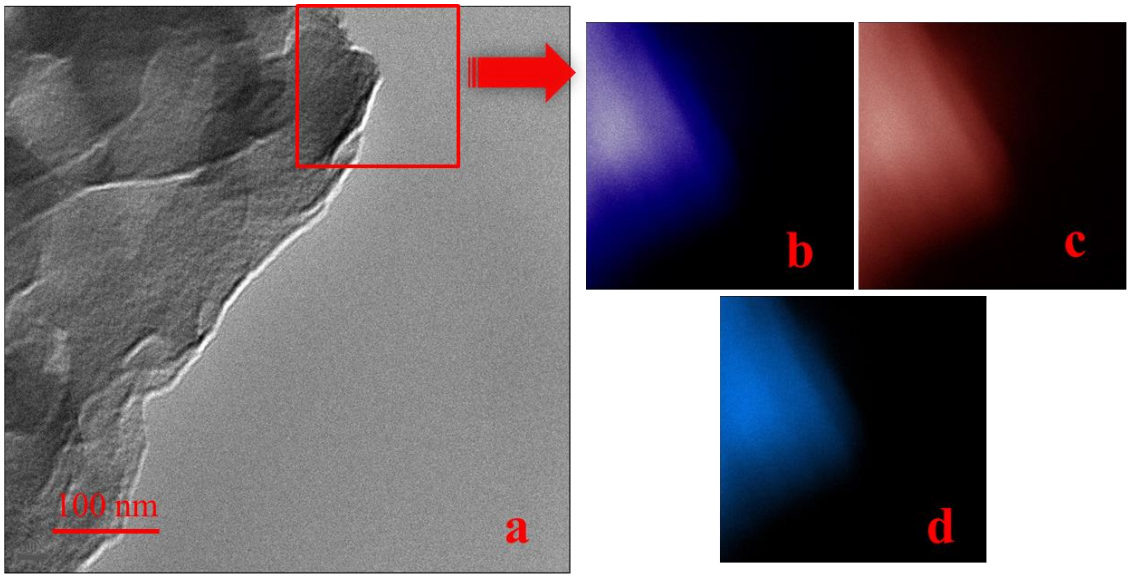

Figure 7.3 TEM image of P-doped g-C_3N_4 (a) and elemental maps of carbon (b), nitrogen (c) and phosphorus (d).

The chemical structure of all samples was further studied by FTIR analysis. Both g-C_3N_4 and P-doped g-C_3N_4 showed very similar FTIR spectra (Figure S7.1, ESI†), with typical C-N heterocycle stretches in the ~1100-1600 cm^{-1} region and breathing mode of the tri-s-triazine units at 800 cm^{-1}.[36] This indicates that the original C-N network was unchanged after P doping. The vibrations of P-related group can barely be observed, which is probably due to the very low ratio of P dopant.[37]

The optical properties of P-C_3N_4 and g-C_3N_4 were examined by UV-Visible spectroscopy. The absorption edge of g-C_3N_4 is at ca. 466 nm (Figure 7.4b), corresponding to a band gap of 2.66 eV. After doping with P, the absorption of the resulting P-C_3N_4 was significantly extended to the infrared region (Figure 7.4c). The great absorption extension was accompanied by the noticeable colour shift from yellow to red brown-ish (Figure 7.4), indicating the drastic modification of the electronic structure of g-C_3N_4 after P doping.

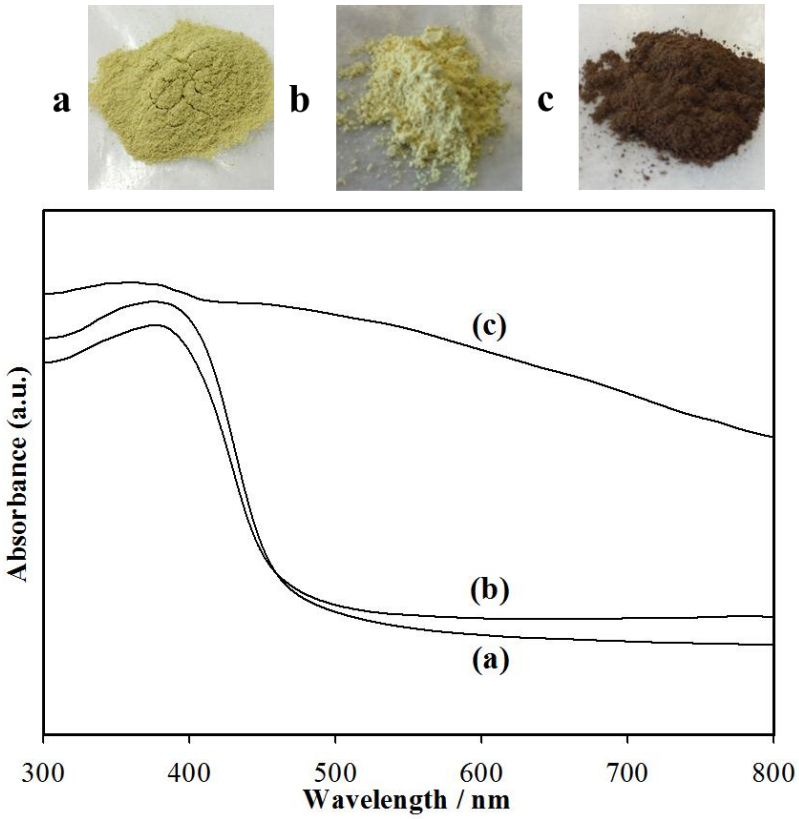

Figure 7.4 UV-visible absorption spectra and corresponding photos of (a) g-C_3N_4 calcined with Na_3PO_4, (b) g-C_3N_4 and (c) P-doped g-C_3N_4.

In the present synthesis, we used $NaH_2PO_2{\cdot}H_2O$ as a novel doping reagent for g-C_3N_4. By heating the mixture of g-C_3N_4 and $NaH_2PO_2{\cdot}H_2O$ at 500 °C, $NaH_2PO_2{\cdot}H_2O$ can produce PH_3 and Na_3PO_4 in-situ,[38, 39] and the resulting PH_3 and Na_3PO_4 could both act as the doping source for P. To investigate whether PH_3 or Na_3PO_4 plays the role of P doping source, we calcined g-C_3N_4 together with Na_3PO_4 at similar condition with that of preparing P-C_3N_4. It was found that the XRD pattern and UV-Vis spectroscopy of the resulting product were both similar with those of the undoped one (Figure 7.1 and Figure 7.4), indicating that the role of Na_3PO_4 as the P doping source is negligible. Therefore, we can conclude that PH_3 is the P source, which play the main role for the modification of the electronic structures of the original g-C_3N_4. Our group has reported that in semiconductors with layered structure or channelled structure, the process of nitrogen doping was greatly

facilitated when using NH_3 gas as N source because NH_3 molecules can diffuse into the interlayer space or the channels of those semiconductors and lead to relatively uniform doping.[40-42] Therefore, we propose that due to the layered structure of g-C_3N_4, PH_3 gas can diffuse into interlayer spacing and lead to the uniform doping of P in the C-N network and thus effective tuning of its electronic structure.

After confirming the successful preparation of P-C_3N_4, we tentatively exfoliated P-C_3N_4 to obtain the corresponding NSs by sonicating P-C_3N_4 powder in water for 1 h with an ultra-sonication probe (step 2 of Scheme 7.1). The obtained nanosheets suspension was very stable and no precipitates were found within 6 months. As a comparison, we also tried to exfoliate undoped g-C_3N_4 with the same method. However, in the sonicated g-C_3N_4 suspension, all g-C_3N_4 sank to the bottom of the suspension in 2 weeks, leaving the supernatant solution clear. Even if the sonication time was extended from 1 h to 8 h, the same phenomenon was observed.

The morphologies of the as-prepared samples were first investigated via transmission electron microscopy (TEM). Bulk g-C_3N_4 is mainly composed of large particles with laminar structure (Figure S7.2a, ESI†). TEM image of P-doped g-C_3N_4 NSs shows the extremely thin nature (Figure S7.2b, ESI†), which is distinct from the bulk material. The morphology of P-doped g-C_3N_4 NSs is very similar to previous reports on g-C_3N_4 NSs and metal oxide NSs.[29, 43] However, we found that the sonicated g-C_3N_4 was not successfully exfoliated to thin sheets, and still composed of a number of layers (Figure S7.2c, ESI†). To further confirm the exfoliation of P-doped g-C_3N_4 and determine the thickness of NSs, atomic force microscopy (AFM) was conducted. The AFM image of NSs on a silicon wafer is shown in Figure 7.5, and the substrate was densely covered with overlapped NS flakes with lateral size of several hundreds of nanometers. Careful searching of non-overlapped regions showed that a thickness of ca. 1 nm was obtained. Considering that the theoretical thickness of a single atomic layer of g-C_3N_4 is 0.325 nm,[32, 44] the as-prepared P-doped g-C_3N_4 NSs are composed of 3 atomic layers.

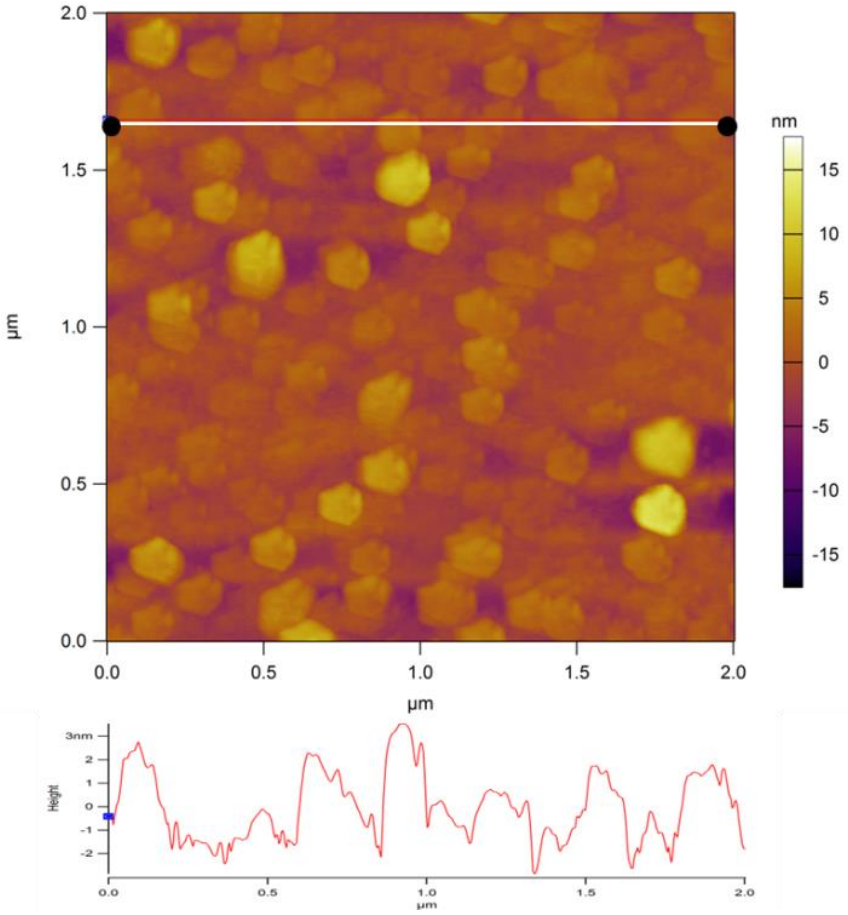

Figure 7.5 AFM image of P-doped g-C_3N_4 NSs and corresponding thickness analysis taken around the white line.

In the XRD pattern of the P-doped g-C_3N_4 NSs, the (002) peak was significantly attenuated and broadened while the (100) peak still existed (Figure 7.6a). This phenomenon reflects that the in-plane structure of the C-N layers was retained and the layered structure of g-C_3N_4 was successfully delaminated to NSs.[29, 31] The exfoliated NSs has weaker and noisier FTIR spectrum (Figure 7.6b) compared to the bulk materials (Figure S7.1, ESI†), but the overall spectrum was very similar. XRD pattern and FTIR spectrum of the NSs indicate that the in-plane structure of NSs were nearly unchanged.

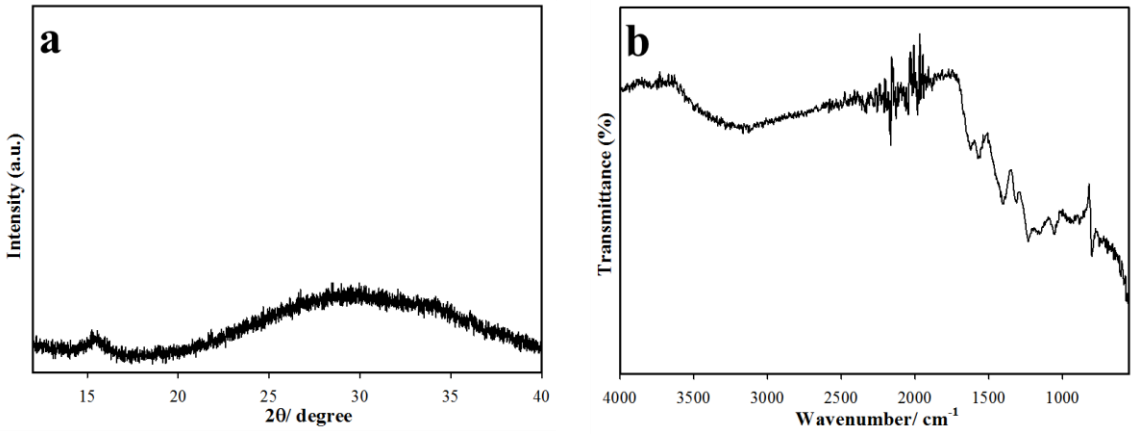

Figure 7.6 XRD pattern (a) and FTIR spectrum (b) of P-doped g-C_3N_4 NSs.

Figure 7.7 shows the photos and UV-Visible absorption spectra of both P-doped g-C_3N_4 NSs and the undoped counterpart dried onto substrates. The P-doped g-C_3N_4 NSs have a very broad absorption shoulder in the visible region (Figure 7.7b), while the undoped counterpart has very weak absorption above 400 nm (Figure 7.7a). The optical absorption corresponds well to their colors, with yellow brown-ish color of the doped NSs and the almost white color of the undoped counterpart.

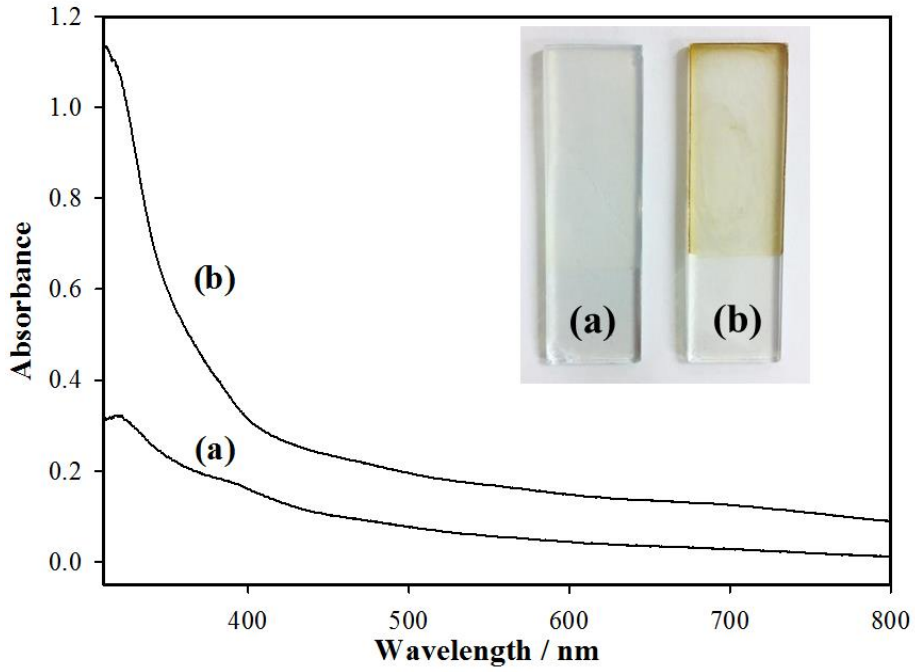

Figure 7.7 UV-visible absorption spectra and photos of (a) sonicated g-C_3N_4 suspension and (b) P-doped g-C_3N_4 NSs suspension dried onto substrate.

Zeta potential measurement depicted that the as-prepared P-doped g-C_3N_4 NSs carried a negative charge of ca. -48.5 mV while the sonicated g-C_3N_4 had negligible surface charge. We also observed that the P-doped g-C_3N_4 NSs suspension flocculated upon addition of

cations such as hydrochloric acid or NaCl, and this phenomenon agreed well with its negative surface charge. The great difference in surface charge explains why P-doped g-C_3N_4 NSs were extremely stable in water but sonicated g-C_3N_4 precipitated quickly. This phenomenon also highlights the importance of the P dopants in the C-N structure for the successful exfoliation and impressive stability in water. The planar structure of g-C_3N_4 will be distorted as a result of the longer P-N bond strength (150-170 pm) compared to that of C-N (135 pm),[45-47] which could possibly faciliate the delamination process. In addition, the larger surface charge may be attributed to the lower electronegativity of P (2.19) than that of C (2.55).[48]

This feature of negative surface charge of P-doped g-C_3N_4 NSs is very similar to metal oxide NSs such as $Ti_{0.91}O_2^{-0.36}$ and $MnO_2^{-0.4}$, which can be used for electrostatic LBL self-assembly via sequential adsorption onto different substrates.[6, 7] In a LBL process, colloidal NSs can be combined with oppositely charged species including organic polyelectrolytes such as polyethylenimine (PEI) and polyaniline (PANI).[43, 49] However, to our knowledge, g-C_3N_4 NSs have never been used as the building blocks to fabricate LBL assembly. We tried to use both poly(diallyldimethylammonium chloride) (PDDA) and PEI as the binding agent to fabricate LBL assembly with the as-prepared P-doped g-C_3N_4 NSs. Figure 7.8A presents the UV-Visible absorbance spectra of the multilayer films of (PDDA-P-doped g-C_3N_4 NSs)$_n$ deposited on a quartz substrate. The peak-top absorbance at ca. 300 nm showed almost a linear increase with the increasing number of deposited PDDA-P-doped g-C_3N_4 NSs bilayers (insert of Figure 7.8A), which provides a strong evidence of the multilayer growth of P-doped g-C_3N_4 NSs.[43, 50] The results also demonstrate the possibility of constructing nanostructures from g-C_3N_4-based NSs via LBL assembly method. In contrast, it is not possible to perform LBL assembly with the sonicated g-C_3N_4 as it does not possess surface charge.

We also fabricated a (PEI- P-doped g-C_3N_4 NSs)$_4$ film onto fluorine-doped tin oxide (FTO) coated glass substrate. The photocurrent responsive behaviour of the film as photoanode in the visible range was investigated in a standard three-electrode photoelectrochemical (PEC) quartz cell. Figure 7.8B shows the I-t curves of both the (PEI- P-doped g-C_3N_4 NSs)$_4$ film and bare FTO substrate. While bare FTO substrate had no photo-response, the (PEI- P-doped g-C_3N_4 NSs)$_4$ film showed obvious anodic photocurrent upon visible light irradiation at 0.45 V vs Ag/AgCl. The observed photocurrent is apparently attributed to the visible light absorption of P-doped g-C_3N_4 NSs.

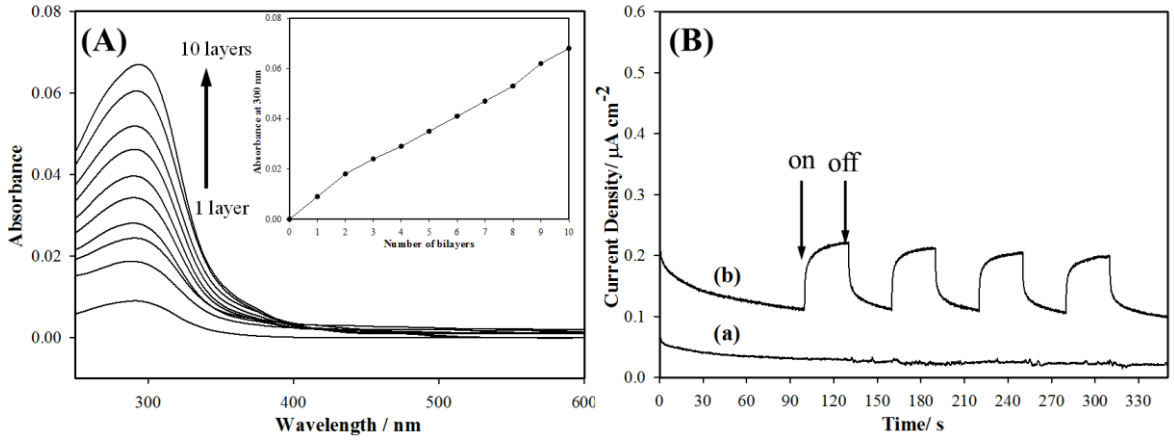

Figure 7.8 (A) UV-Visible absorption spectra of multilayer films of (PDDA-P-doped g-C_3N_4 NSs)$_n$ on a quartz glass substrate, in which n represents the bilayer number. The insert shows the dependence of absorbance at 300 nm as a function of the bilayer number. (B) Photocurrent responses (I-t) at 0.45 V vs Ag/AgCl reference electrode of (a) bare FTO glass and (b) (PEI- P-doped g-C_3N_4 NSs)$_4$ nanosheet film. Measurement condition: a 300 W Xe lamp equipped with 400 nm cut-off filter served as the visible light source, and 0.5 M Na_2SO_4 solution was used as the electrolyte. The illuminated photoanode surface area with the deposition of 4 layers of nanosheet film was ca. 2.3 cm^2.

The photocatalytic hydrogen production performance was also studied. Surprisingly, the sonicated g-C_3N_4 suspension was not able to produce any hydrogen under visible light irradiation, while P-doped g-C_3N_4 NSs could yield hydrogen at a rate of 4.8 $\mu mol \cdot h^{-1} \cdot g^{-1}$ under same conditions. We believe that the improved hydrogen production activity is due to the enhanced visible light absorption of P-doped g-C_3N_4 NSs.

7.4 Conclusions

In summary, we successfully synthesized phosphorus-doped g-C_3N_4 NSs with enhanced visible light absorption. The P dopants replace the carbon atoms in the C-N network while not changing the overall g-C_3N_4 structure. The 1 nm-thick NSs colloidal suspension in water is highly stable and the NSs carry negative surface charge. We also demonstrated the possibility of constructing LBL assembly with the P-doped g-C_3N_4 NSs and organic polyelectrolyte, and the LBL assembly on a FTO substrate showed photocurrent under visible light irradiation. The P-doped g-C_3N_4 NSs also exhibited the capability of performing visible light photocatalytic hydrogen production. The findings not only provide a method to enhance the visible light absorption of g-C_3N_4 NSs, but also promise a new class of building blocks for nanostructure design for a broad range of applications including photocatalytic and photoelectrochemical reactions.

7.5 References

1. K. S. Novoselov, A. K. Geim, S. V. Morozov, D. Jiang, Y. Zhang, S. V. Dubonos, I. V. Grigorieva and A. A. Firsov, *Science*, 2004, **306**, 666-669.

2. Q. J. Xiang, J. G. Yu and M. Jaroniec, *Chem. Soc. Rev.*, 2012, **41**, 782-796.

3. G. C. Xie, K. Zhang, B. D. Guo, Q. Liu, L. Fang and J. R. Gong, *Adv. Mater.*, 2013, **25**, 3820-3839.

4. A. K. Geim, *Science*, 2009, **324**, 1530-1534.

5. S. Pisana, M. Lazzeri, C. Casiraghi, K. S. Novoselov, A. K. Geim, A. C. Ferrari and F. Mauri, *Nat. Mater.*, 2007, **6**, 198-201.

6. M. Osada and T. Sasaki, *J. Mater. Chem.*, 2009, **19**, 2503-2511.

7. R. Z. Ma and T. Sasaki, *Adv. Mater.*, 2010, **22**, 5082-5104.

8. M. Osada and T. Sasaki, *Adv. Mater.*, 2012, **24**, 210-228.

9. J. L. Gunjakar, I. Y. Kim, J. M. Lee, Y. K. Jo and S. J. Hwang, *J. Phys. Chem. C*, 2014, **118**, 3847-3863.

10. J. N. Coleman, M. Lotya, A. O'Neill, S. D. Bergin, P. J. King, U. Khan, K. Young, A. Gaucher, S. De, R. J. Smith, I. V. Shvets, S. K. Arora, G. Stanton, H. Y. Kim, K. Lee, G. T. Kim, G. S. Duesberg, T. Hallam, J. J. Boland, J. J. Wang, J. F. Donegan, J. C. Grunlan, G. Moriarty, A. Shmeliov, R. J. Nicholls, J. M. Perkins, E. M. Grieveson, K. Theuwissen, D. W. McComb, P. D. Nellist and V. Nicolosi, *Science*, 2011, **331**, 568-571.

11. T. Sasaki, M. Watanabe, H. Hashizume, H. Yamada and H. Nakazawa, *J. Am. Chem. Soc.*, 1996, **118**, 8329-8335.

12. T. Sasaki and M. Watanabe, *J. Am. Chem. Soc.*, 1998, **120**, 4682-4689.

13. L. Wang and T. Sasaki, *Chem. Rev.*, 2014.

14. T. Yui, Y. Kobayashi, Y. Yamada, T. Tsuchino, K. Yano, T. Kajino, Y. Fukushima, T. Torimoto, H. Inoue and K. Takagi, *Phys. Chem. Chem. Phys.*, 2006, **8**, 4585-4590.

15. N. Miyamoto, Y. Yamada, S. Koizumi and T. Nakato, *Angew. Chem., Int. Ed.*, 2007, **46**, 4123-4127.

16. H. Sato, K. Okamoto, K. Tamura, H. Yamada, K. Saruwatari, T. Kogure and A. Yamagishi, *Appl. Phys. Express*, 2008, **1**.

17. G. Liu, C. H. Sun, L. Z. Wang, S. C. Smith, G. Q. Lu and H. M. Cheng, *J. Mater. Chem.*, 2011, **21**, 14672-14679.

18. H. N. Kim, T. W. Kim, I. Y. Kim and S. J. Hwang, *Adv. Funct. Mater.*, 2011, **21**, 3111-3118.

19. J. L. Gunjakar, T. W. Kim, H. N. Kim, I. Y. Kim and S. J. Hwang, *J. Am. Chem. Soc.*, 2011, **133**, 14998-15007.

20. S. Ida, C. Ogata, M. Eguchi, W. J. Youngblood, T. E. Mallouk and Y. Matsumoto, *J. Am. Chem. Soc.*, 2008, **130**, 7052-7059.

21. H. Xin, Y. Ebina, R. Z. Ma, K. Takada and T. Sasaki, *J. Phys. Chem. B*, 2006, **110**, 9863-9868.

22. X. Wang, K. Maeda, A. Thomas, K. Takanabe, G. Xin, J. M. Carlsson, K. Domen and M. Antonietti, *Nat. Mater.*, 2009, **8**, 76-80.

23. Y. Wang, X. Wang and M. Antonietti, *Angew. Chem., Int. Ed.*, 2012, **51**, 68-89.

24. X. Wang, S. Blechert and M. Antonietti, *ACS Catal.*, 2012, **2**, 1596-1606.

25. M. J. Bojdys, J. O. Müller, M. Antonietti and A. Thomas, *Chem. Eur. J.*, 2008, **14**, 8177-8182.

26. M. Sadhukhan and S. Barman, *J. Mater. Chem. A*, 2013, **1**, 2752-2756.

27. X. Zhang, X. Xie, H. Wang, J. Zhang, B. Pan and Y. Xie, *J. Am. Chem. Soc.*, 2012, **135**, 18-21.

28. H. X. Zhao, H. T. Yu, X. Quan, S. Chen, H. M. Zhao and H. Wang, *RSC Adv.*, 2014, **4**, 624-628.

29. S. Yang, Y. Gong, J. Zhang, L. Zhan, L. Ma, Z. Fang, R. Vajtai, X. Wang and P. M. Ajayan, *Adv. Mater.*, 2013, **25**, 2452-2456.

30. P. Niu, L. L. Zhang, G. Liu and H. M. Cheng, *Adv. Funct. Mater.*, 2012, **22**, 4763-4770.

31. X. She, H. Xu, Y. Xu, J. Yan, J. Xia, L. Xu, Y. Song, Y. Jiang, Q. Zhang and H. Li, *J. Mater. Chem. A*, 2014, **2**, 2563-2570.

32. J. Xu, L. Zhang, R. Shi and Y. Zhu, *J. Mater. Chem. A*, 2013, **1**, 14766-14772.

33. Z. Xing, Z. Chen, X. Zong and L. Wang, *Chem. Commun.*, 2014, **50**, 6762-6764.

34. M. Sathish, B. Viswanathan, R. P. Viswanath and C. S. Gopinath, *Chem. Mater.*, 2005, **17**, 6349-6353.

35. P. Bouras, E. Stathatos and P. Lianos, *Appl. Catal. B-Environ.*, 2007, **73**, 51-59.

36. Y. Zhang, T. Mori, J. Ye and M. Antonietti, *J. Am. Chem. Soc.*, 2010, **132**, 6294-6295.

37. L. G. Zhang, X. F. Chen, J. Guan, Y. J. Jiang, T. G. Hou and X. D. Mu, *Mater. Res. Bull.*, 2013, **48**, 3485-3491.

38. Q. X. Guan, W. Li, M. H. Zhang and K. Y. Tao, *J. Catal.*, 2009, **263**, 1-3.

39. Q. X. Guan and W. Li, *J. Catal.*, 2010, **271**, 413-415.

40. A. Mukherji, B. Seger, G. Q. Lu and L. Wang, *ACS nano*, 2011, **5**, 3483-3492.

41. A. Mukherji, R. Marschall, A. Tanksale, C. H. Sun, S. C. Smith, G. Q. Lu and L. Z. Wang, *Adv. Funct. Mater.*, 2011, **21**, 126-132.

42. G. Liu, L. Wang, C. Sun, X. Yan, X. Wang, Z. Chen, S. C. Smith, H. M. Cheng and G. Q. Lu, *Chem. Mater.*, 2009, **21**, 1266-1274.

43. G. Liu, L. Wang, C. Sun, Z. Chen, X. Yan, L. Cheng, H. M. Cheng and G. Q. M. Lu, *Chem. Commun.*, 2009, 1383-1385.

44. J. S. Zhang, M. W. Zhang, R. Q. Sun and X. C. Wang, *Angew. Chem., Int. Ed.*, 2012, **51**, 10145-10149.

45. S. Horstmann, E. Irran and W. Schnick, *Angew. Chem., Int. Ed.*, 1997, **36**, 1873-1875.

46. K. Landskron, H. Huppertz, J. Senker and W. Schnick, *Angew. Chem., Int. Ed.*, 2001, **40**, 2643-2645.

47. B. V. Lotsch and W. Schnick, *Chem. Eur. J.*, 2007, **13**, 4956-4968.

48. C. H. Choi, S. H. Park and S. I. Woo, *ACS nano*, 2012, **6**, 7084-7091.

49. B. Seger, J. McCray, A. Mukherji, X. Zong, Z. Xing and L. Wang, *Angew. Chem., Int. Ed.*, 2013, **52**, 6400-6403.

50. L. Wang, Y. Ebina, K. Takada and T. Sasaki, *J. Phys. Chem. B*, 2004, **108**, 4283-4288.

7.6 Supporting information

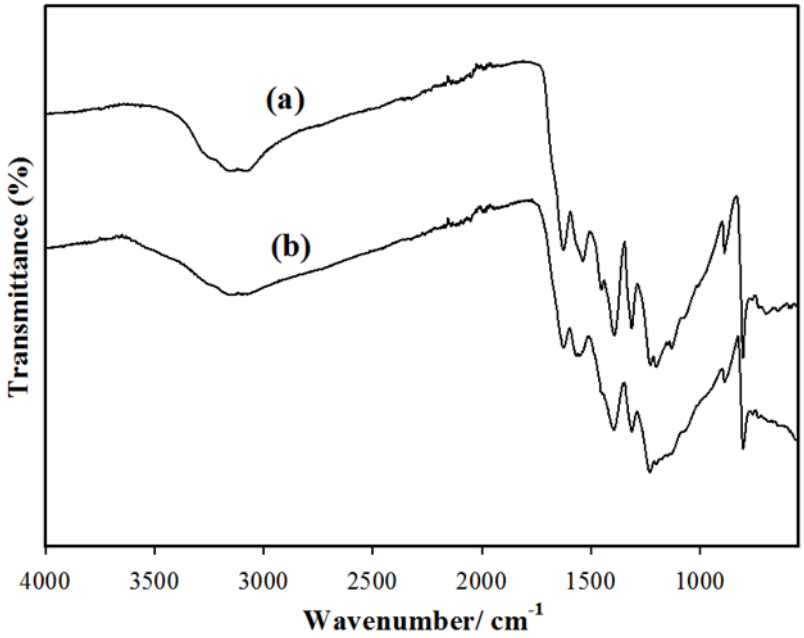

Figure S7.1 FTIR spectra of (a) g-C_3N_4 and (b) P-doped g-C_3N_4.

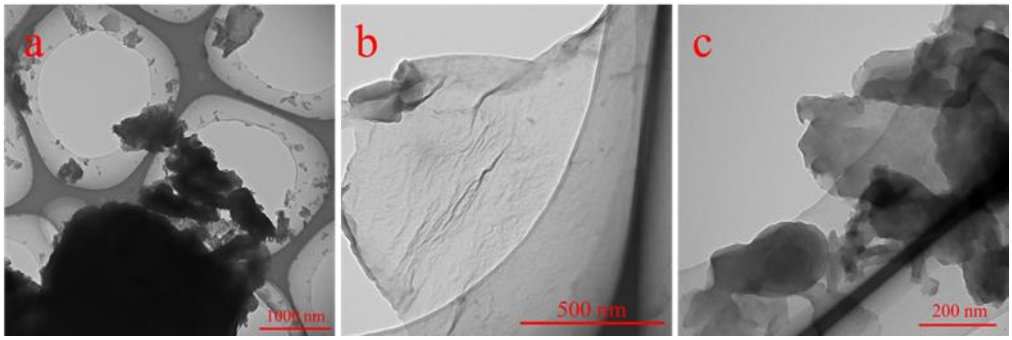

Figure S7.2 TEM images of (a) pristine g-C_3N_4, (b) P-doped g-C_3N_4 NSs, and (c) g-C_3N_4 powders sonicated with ultra-sonication probe (300 W, 40 kHz).

8. Conclusions and recommendations

8.1 Conclusions

This thesis aims to fabricate a series of heterogeneous photocatalysts based on layered semiconductors and the exfoliated nanosheets in order to improve the photocatalytic activities. Starting from two types of layered semiconductors including caesium titanate with perovskite structure and graphitic carbon nitride with graphite-like structure, wet chemistry method was used to exfoliate them into ultrathin 2D nanosheets. Via various strategies including impregnation, exfoliation-restacking and layer-by-layer deposition, composites and assemblies were constructed based on not only the pristine layered semiconductor (C_3N_4-PEDOT), but also the exfoliated nanosheets ($Ti_{0.91}O_2$-Au, $Ti_{0.91}O_2$-CdTe@CdS, P-C_3N_4-PEI). More, the effect of forming heterogeneous structures on the overall photocatalytic water splitting performance was studied. The main conclusions of this thesis are as follows:

(i) An exfoliation-restacking method was used to prepare a nanohybrid of titania nanosheets and octahedral Au nanoparticles, which showed considerably improved photocatalytic hydrogen production performance compared to naked titania and titania with photodeposited Au particles.

In this nanohybrid, octahedral Au nanoparticles were embedded into the matrix of titania, which possessed excellent surface plamson resonance (SPR) properties. The SPR effect greatly enhanced the local light intensity and effectively scattered photons thorough titania particles, contributing to the overall hydrogen evolution activities. Moreover, the general strategy can be applied to other nanosheets or plasmonic metal nanoparticles in order to tailoring the SPR effect.

(ii) A nanocomposite was built with titania nanosheets and CdTe@CdS nanocrystals through exfoliation-restacking method. This nanocomposite exhibited impressively enhanced hydrogen production capability compared to both its single component under visible light irradiation.

The introduction of CdTe@CdS nanocrystals not only extended the visible light absorption, but also dramatically suppressed charge recombination due to the proper energy band alignment and the formation of p-n nanojunctions. The dual functions of CdTe@CdS nanocrystals were highlighted, i.e., visible light absorbed and p-n nanojunction.

(iii) A new C_3N_4-based composite was synthesized by co-loading PEDOT as the hole transport pathway and Pt as the electron trap. The as-prepared composite exhibited significantly increased hydrogen production under visible light illumination compared to pure C_3N_4 and remained very stable in the photocataytic reaction process.

In this composite, PEDOT was first loaded onto C_3N_4 via impregnation as the hole transport pathway, and then Pt was photodeposited at the bare C_3N_4 surface with PEDOT. Through this method, the reduction and oxidation reaction sites were spatially separated, giving rise to more efficient photocatalysis. The importance of hole conducting polymer like PEDOT was demonstrated.

(iv) Phosphorus-doped C_3N_4 nanosheets with enhanced visible light absorption were successfully synthesized.

Pristine C_3N_4 was found to be difficult to be exfoliated via sonication in water while the P-doped C_3N_4 was not only delaminated to 1 nm-thick nanosheets, but also remained extremely stable in the colloidal suspension. The P-doped C_3N_4 nanosheets showed visible light hydrogen production while the undoped counterpart was not active at all. The P-doped C_3N_4 nanosheets carried negative surface charge in the suspension, which enabled its LBL assembly with polyelectrolyte such as PDDA and PEI. The findings promise novel metal-free building blocks for photoelectrochemical devices.

8.2 Recommendations for future works

This thesis has demonstrated some effective strategies to construct heterogeneous photocatalysts based on layered semiconductors and exfoliated 2D nanosheets. Through careful selecting the proper guest species and synthesis method, efficient photocatalytic activities can be obtained. Despite the great variety of 2D nanosheets and functional nanoparticles, the works on nano-assembly based on them are still very limited. Therefore, future works are highly recommended in the following aspects:

(i) Constructing nanohybrids with various nanosheets and nanoparticles through exfoliation-restacking. Less studied nanosheets other than titania nanosheets such as niobate nanosheets, carbon nitride nanosheets should be made use of to form heterostructured photocatalysts. Exfoliation-restacking is a powerful method to build loosely packed heterostructures, especially for photocatalytic water splitting.

(ii) Building new layer-by-layer assemblies with metal-free nanosheets such as carbon nitride nanosheets. The emergence of more metal-free nanosheets opens up the opportunities of building exciting LBL assemblies, with special chemical, electrical and optical properties.

(iii) Modification of nanosheets for tuning their properties. As a result of quantum size confinement effect, the exfoliated nanosheets often possess enlarged band gaps compared to the pristine layered semiconductors, which can limits the optical absorption. Careful modifications such as doping can effectively improve the optical absorption.